The Dissertation Committee for Matthew George Panthani Certifies that this is the approved version of the following dissertation:

Colloidal Nanocrystals with Near-infrared Optical Properties: Synthesis, Characterization, and Applications

Committee:

Brian A. Korgel, Supervisor

Ananth Dodabalapur

C. Buddie Mullins

James Chelikowsky

Arumugam Manthiram

Colloidal Nanocrystals with Near-infrared Optical Properties: Synthesis, Characterization, and Applications

by

Matthew George Panthani, B.S.

Dissertation

Presented to the Faculty of the Graduate School of

The University of Texas at Austin

in Partial Fulfillment

of the Requirements

for the Degree of

Doctor of Philosophy

The University of Texas at Austin

November 2011

Dedication

for my family

Acknowledgements

As I conclude the chapters of this dissertation, I am grateful to those who have contributed to my educational and professional development.

First, I would like to thank my advisor, Dr. Brian Korgel. His creativity and passion for science have helped mold me as a scientist and inventor. I consider myself lucky to work for someone who was able to provide me with not only the necessary tools, but also the mindset for doing innovative research.

Much of my doctoral journey and growth has been in "parallel" with Vahid Akhavan and Brian Goodfellow. Our accomplishments are quite incredible considering we began with little knowledge of how to make functioning photovoltaic devices. Speaking of which, I would like to express gratitude towards our first functioning "device", a sandwich film of nanocrystals smashed between two electrodes and assembled with binder clips. While our progress since then makes the resulting 0.00001% power conversion efficiency forgettable (and slightly embarrassing), measuring a reproducible photocurrent gave us the hope to continue along in this project.

Over the years I have worked with a number of exceptional individuals, remarkable in both scientific ability and in character. Among the many, I would like to thank Andrew Heitsch, Doh Chang Lee, Colin Hessel, Hsing-Yu Tuan, Damon Smith, Danielle Smith, and Dayne Fanfair for at some point providing me with mentorship. Additionally I would like to thank some of my colleagues – Aaron Chockla, Michael Rasch, Vince Holmberg, Chet Steinhagen, Jose-Luis Hueso, Kate Collier, and Kate Shipman. Our frequent scientific discussion, debate, and criticism helped to keep me sharp, while our non-scientific discussion has at times kept me sane.

I would like to specifically thank some relatively new members of our research group: C. Jackson Stolle, Taylor Harvey, and Tim Bogart. They have been indispensible to me in my busy last few months, doing some experiments for me while I have been traveling, writing, and frantically tying loose ends. I hope I was able to impart some of my knowledge upon them, and I hope they can continue along some of the research paths I have helped forge. I would like to thank my many collaborators in other research groups, such as Takuji Adachi, Chris Lombardo, Tarik Khan, and Hyun Seo Park.

I have been privileged to have mentored an unusually large number of undergraduate students. Among them, I would like to especially thank Danny Hellebusch and Dariya Reid. They were instrumental in many of the projects discussed in this dissertation. By the end of their times in Austin, I found myself to be learning from them. I wish them luck and continued success in their academic careers and in life.

I would like to thank Professors Paul Barbara, Ananth Dodabalapur, and Allen Bard for their contributions to the photovoltaics project and their students and postdocs who were involved. Without the collaborative, multidisciplinary approach to this project, our development certainly would not have been as rapid as it was.

I am especially grateful for advice, encouragement, and education from my committee members. I would also like to thank my undergraduate research advisor, Syed Qutubuddin, as well as R. Mohan Sankaran at Case Western Reserve University for advice and mentorship. Additionally I would like to thank Michael Dell for sponsoring my Engineering Doctoral Fellowship which enabled me to pursue my education with little financial worry.

Perhaps most instrumental to my success has been my near and extended family. They have in shaped me both as a scientist and an individual. My mother and father provided me with the education and encouragement to succeed, as well as support. My

parents have most certainly been an inspiration for me. It is no coincidence that both my father and I pursued doctoral degrees when there were more conventional and much easier paths in front of us. Likewise, it is also no coincidence that my younger sister, Tessie, is also pursuing a PhD in Chemical Engineering. I would like to thank all of my family for their love, support, and prayers. And Annie.

Colloidal Nanocrystals with Near-infrared Optical Properties: Synthesis, Characterization, and Applications

Matthew George Panthani, Ph.D.

The University of Texas at Austin, 2011

Supervisor: Brian A. Korgel

Colloidal nanocrystals with optical properties in the near-infrared (NIR) are of interest for many applications such as photovoltaic (PV) energy conversion, bioimaging, and therapeutics. For PVs and other electronic devices, challenges in using colloidal nanomaterials often deal with the surfaces. Because of the high surface-to-volume ratio of small nanocrystals, surfaces and interfaces play an enhanced role in the properties of nanocrystal films and devices.

Organic ligand-capped $CuInSe_2$ (CIS) and $Cu(In_XGa_{1-X})Se_2$ (CIGS) nanocrystals were synthesized and used as the absorber layer in prototype solar cells. By fabricating devices from spray-coated CuInSe nanocrystals under ambient conditions, solar-to-electric power conversion efficiencies as high as 3.1% were achieved. Many treatments of the nanocrystal films were explored. Although some treatments increased the conductivity of the nanocrystal films, the best devices were from untreated CIS films. By modifying the reaction chemistry, quantum-confined $CuInSe_XS_{2-X}$ (CISS) nanocrystals were produced. The potential of the CISS nanocrystals for targeted bioimaging was demonstrated via oral delivery to mice and imaging of nanocrystal fluorescence.

The size-dependent photoluminescence of Si nanocrystals was measured. Si nanocrystals supported on graphene were characterized by conventional transmission

electron microscopy and spherical aberration (Cs)-corrected scanning transmission electron microscopy (STEM). Enhanced imaging contrast and resolution was achieved by using Cs-corrected STEM with a graphene support. In addition, clear imaging of defects and the organic-inorganic interface was enabled by utilizing this technique.

Table of Contents

List of Tables

List of Figures

Chapter 1: Introduction

The field of nanoscience has emerged over the past two decades via an amalgamation of many parallel efforts in different fields of condensed matter physics. In the mid 1980's, Richard Smalley and coworkers at Rice University discovered C_{60}[1] (often referred to as "buckyballs"), which spurred research and discovery of other sp^2 hybridized carbon nanomaterials, such as other spherical fullerenes, carbon nanotubes, and graphene. Also during this time, Louis Brus and coworkers at Bell Laboratories were experimenting with small semiconductor crystallites which demonstrated size-tunable optical properties.[2-4] These crystallites came to be known as "quantum dots" and would form another pillar of nanoscience due to their unique properties. In 1990, Canham reported luminescence from electrochemically etched silicon with nanoscale domains.[5] This silicon had room temperature photoluminescence, which at the time was considered controversial, because emission from Si is forbidden due to an indirect bandgap. Further work in the field of silicon nanomaterials has demonstrated that nanoscale silicon can emit with surprisingly high quantum efficiencies due to quantum confinement.[6] In the 1990's, Lieber and coworkers demonstrated controllable synthesis of silicon nanowires via seeded growth off a substrate using vapor-liquid-solid (VLS) growth.[7] This was intriguing to use as a testbed for the effects of 2 dimensional confinement of charge carriers in electronic devices. Additionally, this spurred research into forming a vast array of 1D semiconducting and metallic structures via VLS, as well as solution-based methods such as solution-liquid-solid (SLS),[8] supercritical fluid-liquid-solid (SFLS),[9] and surfactant-based approaches.

While the discovery of these new materials has spurred research, nanomaterials have actually been used in commercial applications for decades. Nanoparticles are used extensively in many applications, such as pigments in paints, cosmetics, antireflective and UV-protective coatings,[10] and as fillers in polymers to enhance mechanical properties to name a few. These nanoparticles are used primarily for their very high available surface area and optical transparency. Semiconductor nanocrystal, however are a special class of nanoparticles—crystalline and typically no more than about 20 nm in diameter, they usually exhibit quantum confinement effects and unique physical properties. An extensive colloidal chemistry using capping ligands to control size without aggregation has been developed to produce nanocrystals of a wide range of composition. Gas-phase synthesis combined with post-synthesis colloidal manipulation has also become an effective way to obtain nanocrystals in this size range. Nanocrystals can be generated with very narrow size distributions (5-10% standard deviation about the mean diameter); particle shape can be manipulated (i.e., disks, rods, tetrapods, etc.); and different materials can be interfaced in individual nanocrystals to form heterostructures, such as core-shell, rod-tip, or striated structures. An extensive library of nanocrystal materials is available to build electronic devices. Semiconductor nanocrystals are essentially macromolecules that are composed of a crystalline inorganic core terminated with capping ligands that can be dispersed and handled in solvents like inks for depositing inorganic films.

1.1. NANOCRYSTAL DEPOSITION AND THEIR USE AS "BUILDING BLOCKS" FOR NEW THIN FILM MATERIALS

Nanocrystal films can be deposited by simple drop-casting from solvent dispersions, which can often provide sufficiently uniform local area coverage on a substrate for laboratory tests of material properties. Commercial applications, however, require much better control over film thickness and uniformity. Various nanocrystal deposition methods that have been studied to achieve better uniformity include covalent grafting on chemically modified surfaces, spray deposition,[11] inkjet printing,[12] spin-coating,[13] and layer-by-layer deposition.[14] Nanocrystal films can also be assembled on liquid interfaces[15] and then deposited and patterned on substrates by contact transfer[16-18].

Monodisperse nanocrystals can spontaneously order into superlattices upon solvent evaporation.[19-22] For many applications, it is not clear how important ordered assembly is, although studies on metal nanocrystals have shown that order can significantly improve carrier transport.[23] Applications that rely on specific size-dependent properties, like the color of light emitting quantum dots in ncLEDs, clearly require uniformity particle size. Structurally complex binary nanocrystal superlattices (BSLs) offer further capability to mix nanocrystals with different properties, such as semiconductor and magnetic nanocrystals for example in a highly controlled manner.[21, 24, 25] Recently, rapid binary superlattice film formation has been demonstrated over large areas (~cm's) on liquid interfaces (Figure 1.1).[15] These structures are mechanically stable enough to be transferred to solid supports for device fabrication.

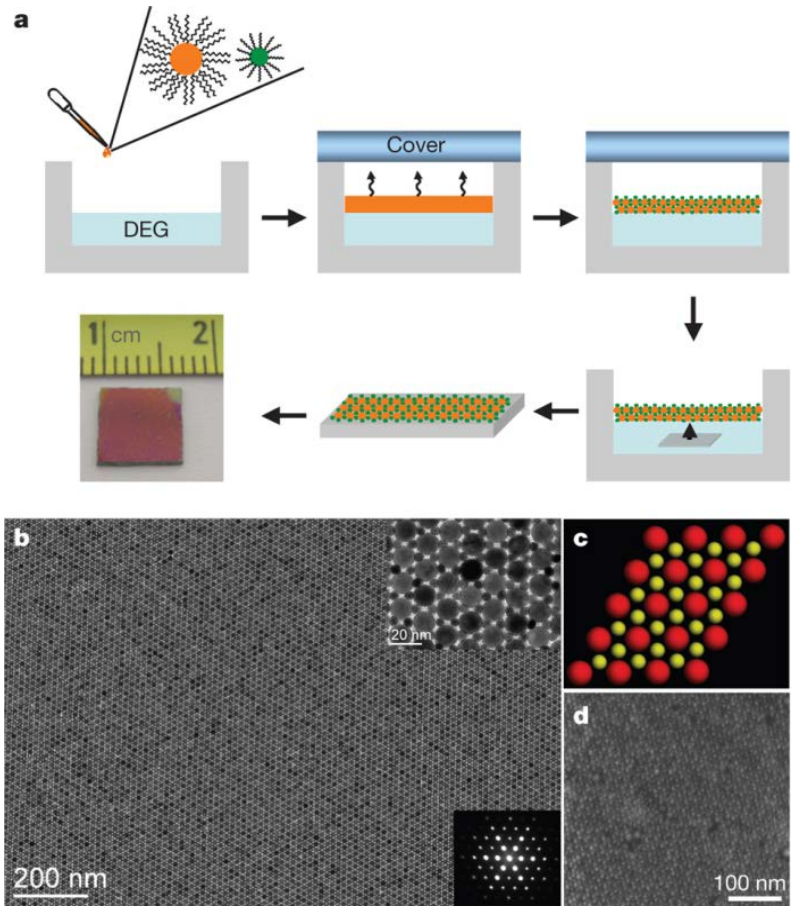

Figure 1.1. Nanocrystal assembly. (a) A bidisperse dispersion of sterically-stabilized nanocrystals is dropped on an air-liquid interface and the solvent evaporates under controlled conditions. The nanocrystals float on the liquid interface and order into a BSL membrane. The photograph shows a typical BSL membrane transferred to a SiO_2 coated Si wafer. (b) TEM image of a BSL of 15 nm Fe_3O_4 and 6 nm FePt nanocrystals with (c) a crystallographic model of the structure and (d) a scanning electron microscopy (SEM) image of the BSL. Reprinted by permission from Macmillan Publishers Ltd: Nature 446, 474-477 (22 July 2008).

1.2. NANOCRYSTALS FOR BIOMEDICAL APPLICATIONS

Nanocrystals have great potential advantages for biomedical applications. Their small size enables them to permeate cell membranes. Although many quantum dots contain toxic heavy metals (e.g. CdSe,[26] HgTe,[14] InAs[27]), the toxicity can be reduced by growing an epitaxial shell (such as ZnS), or using less common alternative quantum dot materials. Recent works have demonstrated the ability of colloidal nanocrystals to be suitable candidates for biolabeling,[28-30] in vivo imaging,[31-33] and photothermal therapy.[34]

1.3. NANOCRYSTAL SYNTHESIS

Semiconductor nanocrystals are in a sense very large molecules. They can be synthesized chemically using organic ligands to bond to and protect the nanocrystal surfaces. One of the major appeals of colloidal nanocrystals is the ability to finely control the size, shape, composition, and crystal structure of the material. A wide variety of colloidal nanocrystals can be synthesized by "hot injection" methods in which metal salts and/or organometallic precursors are combined in a hot solvent. Some common precursors include metal chlorides, oxides, metal-phosphonates/oleates, and trioctylphosphine chalcogenides (TOP:E, where E is a chalcogen). Capping ligands in the reaction mixture restrict growth by binding the growing nanocrystal. Examples of capping ligands include trioctylphosphine oxide (TOPO), amines, thiols, and phosphonic acids. Some capping ligands can control reaction kinetics as well as direct growth by selectively binding to specific crystallographic facets. Nanocrystals can be synthesized with polydispersities of less than 10%.

In a typical reaction, one precursor is injected into the reaction mixture to induce a burst of nucleation. A schematic is shown in Figure 1.2. Several reviews have discussed control of nanocrystal synthesis in great detail.[35, 36]

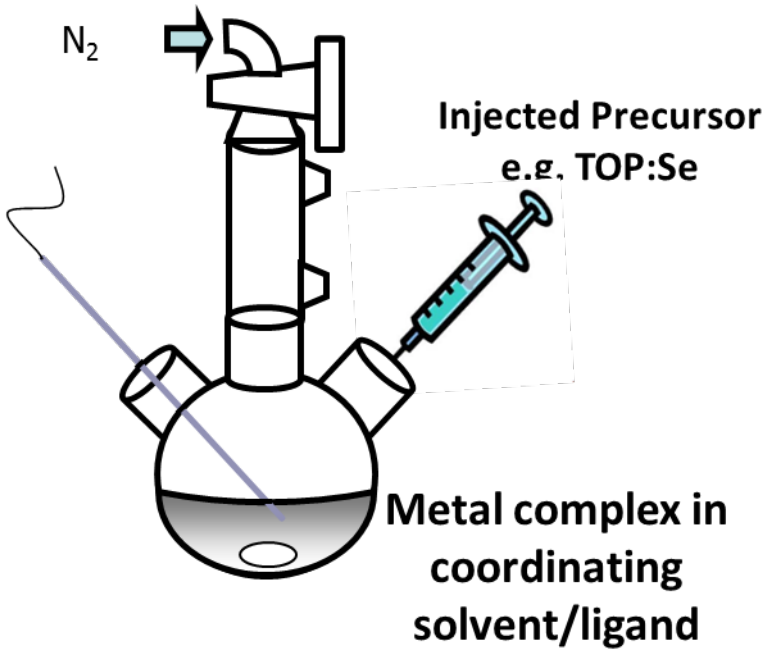

Figure 1.2. An illustration of nanocrystal synthesis.

Heterostructures such as core-shell,[37-39] rod-tip,[40] striated structures can be synthesized by sequential injections of precursors or post-synthesis cation exchange.[41-44] Depending on the valence and conduction band alignments and geometry, these heterostructures can enhance exciton dissociation or recombination.[40, 45, 46]

1.3.1. Nanocrystal Assemblies

The basis of nanocrystal electronics is not individual nanocrystals, but their collective assemblies. Nanocrystal assemblies can be disordered or ordered, with one component or many. While the electronic properties within a semiconductor nanocrystal may be similar to that of the bulk semiconductor, the large surface area of the collective assembly and the barriers that exist between individual nanocrystals tend to dominate transport. Ligand-stabilized nanocrystals will arrange into ordered structures upon evaporation of the solvent due to competing van der Waals interactions between the inorganic hard spheres and steric stabilization provided by the ligand shell.[19] Through controlled evaporation, translation order can increase to length scales of several microns. Such assemblies are commonly referred to as superlattices. Binary nanocrystal assemblies have been synthesized in a variety of different structures. Binary nanocrystal assemblies isostructural to AlB_2,[25] $NaZn_{13}$, $CaCu_5$, $MgZn_2$, $MgNi_2$, Cu_3Au, Fe_4C, and NaCl have been synthesized.[21, 22, 47] Proposed driving mechanisms for assembly include entropic,[22, 48] Coulombic,[21] depletion,[49, 50] dipole,[35, 51] and van der Waals interactions.[21, 22, 47, 52] Recently, the Murray group has demonstrated deposition of superlattices on centimeter-scale substrates by directed assembly at a controlled air-liquid interface.[15, 18] A photograph of a binary superlattice created at an air-liquid interface along and SEM images down different orientations is shown in Figure 1.1.

1.3.2. Deposition methods

1.4. ELECTRONIC PROPERTIES OF NANOCRYSTALS

The electronic properties of amorphous and granular materials have been studied in great detail for several decades. A large amount of the theoretical framework used to describe this materials was developed by Mott,[53, 54] Altshuler,[55] and Efros and Shklovskii.[56] In early days of studying these theories, the only available samples to test these theories were highly polydisperse semiconductor and metal particles. The recent advancements in colloidal nanomaterials synthesis have enabled the ability to test these theoretical frameworks with greater detail.

Nanocrystals are typically capped with aliphatic chains ranging from about 8 to18 carbons long that enable controlled synthesis and dispersibility in solvents. However, for electronic application, these insulating chains hinder charge transport by reducing electronic coupling. In a film of nanocrystals, the coupling energy, can be expressed as $\beta = h\,\Gamma$, where h is Planck's constant and Γ is the exchange coupling energy, which can be approximated as

$$\Gamma \sim e^{-2\left(\frac{(2m^{*}\Delta E)}{\hbar^{2}}\right)^{1/2}\Delta x} \qquad (1)$$

Where $m^{*}$is the carrier effective mass, ΔE is the height of the tunneling barrier, and Δx is the minimum edge-to-edge distance of particles. The tunneling rate drops exponentially with interparticle separation, with a weaker dependence on effective mass and energy barrier. Many reports indicate the removal of bulky ligands or replacement with smaller molecules to greatly increase conductivity.[57, 58]

A second important contributor to conduction in nanocrystal solids is the Coulombic charging energy, E_c, which is the energetic cost for placing an additional charge carrier inside a nanocrystal. Charging energies of individual nanocrystals have been measured for Au[59] and CdSe[60] nanocrystals. The charging energy of a nanocrystal with radius *r* in a medium with relative dielectric constant ϵ_m can be expressed as

$$E_c = \frac{e^2}{4\pi\epsilon_0\epsilon_m r} \tag{2}$$

where *e* is the fundamental charge.

Strong coupling occurs when the coupling energy is greater than the available thermal energy ($\beta > k_B T$). When $\beta > E_c$, carriers can begin to move freely through the nanocrystal solid. In this formalism, the transition between the Coulombic-dominated (insulating) and coupling-dominated (conducting) is called a Mott metal-insulator transition. Mott had described these transitions in disordered semiconductors and oxide materials.[53, 54, 61] This has been observed in nanocrystals, with transitions occurring both as a function of nanocrystal separation and through reduction of the energetic barrier via use of conducting ligands. Coupling has been demonstrated via changes in both conductivity and optical properties.

The electrical conductivity (σ) of a semiconductor is related to the free carrier (i.e., electron and hole) concentrations and the electron and hole mobilities:

$$\sigma = ne\mu_e + pe\mu_p \tag{3}$$

n and *p* are the electron and hole carrier concentrations, and μ_e and μ_p are the electron and hole carrier densities. In a doped semiconductor, one type of carrier has a

much greater concentration than the ther (called the majority carrier). In these cases, the contribution to conductivity from the carrier with lower concentration (minority carrier) can be neglected. In nanocrystal films, conductivity can be measured by simply by passing a current between two points and measuring the voltage (or vice-versa). However, a four-point probe technique is typically used to eliminate contact resistance.

1.4.1. Models of electronic transport through nanocrystal solids

Carrier transport through semiconductor nanocrystal films typically occurs by hopping, variable range hopping (VRH) or Efros-Shklovskii (ES) VRH. The mobility (and conductance) typically increases with increasing temperature. At lower temperature for a variety of nanocrystal films including CdSe[62] and PbSe, , where *v* depends on dimensionality of the system. At higher temperatures, hopping can occur and the temperature-dependence of the conductance follows Arrhenius-like temperature dependence.[62] Coulomb charging in smaller nanocrystals further hinders transport and the Efros-Shklovskii (ES)-VRH model is more applicable.

The replacement of bulky organic, electrically insulating, ligands with smaller molecules like hydrazine or short-chain dithiols can significantly increase the conductivity of nanocrystal films.[57, 58, 63] In fact, annealed (200°C) $In_2Se_4^{2-}$-capped CdSe nanocrystal films with very high the field-effect mobilities (16 $cm^2V^{-1}s^{-1}$) showed a decreased mobility with increasing temperature, characteristic of band transport.[64]

1.4.2. Doping nanocrystal solids

Substitutional impurity atom doping of nanocrystals has not been effective for controllably modulating the electrical properties of nanocrystal films. A 5 nm diameter Si nanocrystal has about 1,300 atoms, so a single impurity atom adds an extremely high doping concentration of ~10^{19} cm^{-3}, making it impossible to achieve moderate doping levels. Therefore, external doping has been explored. Hydrazine exposure of PbSe and PbTe nanocrystals has led to n-type behavior.[57] K vapor exposure has led to doping of CdSe nanocrystal films.[65] ZnO nanocrystals have been doped with added sodium biphenyl. Nanocrystals themselves can also serve as dopants. For instance, p-type conductivity that was significantly enhanced when PbTe and Ag_2Te nanocrystals were combined compared to the pure nanocrystal films.[66] Heterostructure nanocrystals may also provide a way to control carrier concentrations, as in the case of core-shell Au-PbS nanocrystals that exhibited p-type conductivity, presumably due to the injection of a mobile hole into the PbS valence band from the Au core.[67]

1.5. DISSERTATION OVERVIEW

The synthesis of characterization of a variety of nanocrystal systems is discussed in Chapter 2. In particular, the synthesis and characterization of $CuInSe_2$, $CuInS_2$, $CuIn_XGa_{1-X}Se_2$, and Cu_2SnZnS_4 nanocrystals for photovoltaic applications is discussed. In addition, this chapter will describe the synthesis and characterization of quantum confined $CuInSe_XS_{2-X}$ nanocrystals. Chapters 3 and 4 will discuss the utilization of $CuInSe_2$ nanocrystals in proof-of-concept photovoltaic devices and processing of $CuInSe_2$ nanocrystal films, respectively.

Chapter 5 explores the use of quantum confined $CuInSe_XS_{2-X}$ nanocrystals for *in vivo* imaging. The nanocrystals are incorporated into polymer microspheres and conjugated with a protein that targets specific cells in the gut. Chapters 6 and 7 discuss the characterization of luminescent Si nanocrystals. Their luminescence is studied in Chapter 6, while in Chapter 7 the nanocrystals are imaged using transmission electron microscopy using graphene as a support. Chapter 8 summarizes the main points of this dissertation and suggests areas for future work.

1.6. REFERENCES

1. Kroto, H. W.; Heath, J. R.; O'Brien, S. C.; Curl, R. F.; Smalley, R. E. *Nature* **1985,** 318, (6042), 162-163.

2. Brus, L. *J. Chem. Phys.* **1984,** 80, (9), 4403.

3. Brus, L. *The Journal of Physical Chemistry* **1986,** 90, (12), 2555-2560.

4. Bawendi, M. G.; Wilson, W. L.; Rothberg, L.; Carroll, P. J.; Jedju, T. M.; Steigerwald, M. L.; Brus, L. E. *Physical review letters* **1990,** 65, (13), 1623-1626.

5. Canham, L. T. *Applied Physics Letters* **1990,** 57, (10).

6. Jurbergs, D.; Rogojina, E.; Mangolini, L.; Kortshagen, U. *Appl. Phys. Lett.* **2006,** 88, (23), 233116.

7. Morales, A. M.; Lieber, C. M. *Science* **1998,** 279, (5348), 208-211.

8. Heitsch, A. T.; Fanfair, D. D.; Tuan, H.-Y.; Korgel, B. A. *Journal of the American Chemical Society* **2008,** 130, (16), 5436-5437.

9. Holmes, J. D.; Johnston, K. P.; Doty, R. C.; Korgel, B. A. *Science* **2000,** 287, (5457), 1471-1473.

10. Buzea, C. *Biointerphases* **2007,** 2, (4), MR17.

11. Akhavan, V. A.; Panthani, M. G.; Goodfellow, B. W.; Reid, D. K.; Korgel, B. A. *Optics express* **2010,** 18 Suppl 3, A411-20.

12. Wood, V.; Panzer, M. J.; Chen, J.; Bradley, M. S.; Halpert, J. E.; Bawendi, M. G.; Bulović, V. *Advanced Materials* **2009,** 21, (21), 2151-2155.

13. Kuipers, E. W.; Laszlo, C.; Wieldraaijer, W. *Catalysis Letters* **1993,** 17, (1), 71-79.

14. Rogach, A. L.; Koktysh, D. S.; Harrison, M.; Kotov, N. A. *Chemistry of Materials* **2000,** 12, (6), 1526-1528.

15. Dong, A.; Chen, J.; Vora, P. M.; Kikkawa, J. M.; Murray, C. B. *Nature* **2010,** 466, (7305), 474-477.

16. Achermann, M.; Petruska, M. A.; Kos, S.; Smith, D. L.; Koleske, D. D.; Klimov, V. I. *Nature* **2004,** 429, (6992), 642-6.

17. Rizzo, A.; Nobile, C.; Mazzeo, M.; De Giorgi, M.; Fiore, A.; Carbone, L.; Cingolani, R.; Manna, L.; Gigli, G. *ACS nano* **2009,** 3, (6), 1506-12.

18. Dong, A.; Chen, J.; Oh, S. J.; Koh, W.-k.; Xiu, F.; Ye, X.; Ko, D.-K.; Wang, K. L.; Kagan, C. R.; Murray, C. B. *Nano Letters* **2011,** 11, (2), 841-846.

19. Korgel, B. A.; Fullam, S.; Connolly, S.; Fitzmaurice, D. *The Journal of Physical Chemistry B* **1998,** 102, (43), 8379-8388.

20. Talapin, D. V.; Shevchenko, E. V.; Murray, C. B.; Kornowski, A.; Förster, S.; Wellert, H. *Journal of the American Chemical Society* **2004,** 126, (40), 12984-12988.

21. Shevchenko, E. V.; Talapin, D. V.; Murray, C. B.; O'Brien, S. *Journal of the American Chemical Society* **2006,** 128, (11), 3620-3637.

22. Shevchenko, E. V.; Talapin, D. V.; Kotov, N. A.; O'Brien, S.; Murray, C. B., Structural Diversity in Binary Nanoparticle Superlattices. In Nature Publishing Group: 2006; Vol. 439, pp 55-59.

23. Doty, R. C.; Yu, H.; Shih, C. K.; Korgel, B. A. *The Journal of Physical Chemistry B* **2001,** 105, (35), 8291-8296.

24. Shevchenko, E. V.; Talapin, D. V.; Kotov, N. A.; O'Brien, S.; Murray, C. B. *Nature* **2006,** 439, (7072), 55-59.

25. Smith, D. K.; Goodfellow, B.; Smilgies, D.-M.; Korgel, B. A. *Journal of the American Chemical Society* **2009,** 131, (9), 3281-3290.

26. Murray, C. B.; Norris, D. J.; Bawendi, M. G. *Journal of the American Chemical Society* **1993,** 115, (19), 8706-8715.

27. Kim, S. W.; Zimmer, J. P.; Ohnishi, S.; Tracy, J. B.; Frangioni, J. V.; Bawendi, M. G. *J Am Chem Soc* **2005,** 127, (30), 10526-32.

28. Bruchez, M., Jr.; Moronne, M.; Gin, P.; Weiss, S.; Alivisatos, A. P. *Science* **1998,** 281, (5385), 2013-6.

29. Gerion, D.; Parak, W. J.; Williams, S. C.; Zanchet, D.; Micheel, C. M.; Alivisatos, A. P. *J Am Chem Soc* **2002,** 124, (24), 7070-4.

30. Alivisatos, A. P.; Gu, W.; Larabell, C. *Annual review of biomedical engineering* **2005,** 7, 55-76.

31. Dubertret, B.; Skourides, P.; Norris, D. J.; Noireaux, V.; Brivanlou, A. H.; Libchaber, A. *Science* **2002,** 298, (5599), 1759-62.

32. Lim, Y. T.; Kim, S.; Nakayama, A.; Stott, N. E.; Bawendi, M. G.; Frangioni, J. V. *Molecular imaging* **2003,** 2, (1), 50-64.

33. Kim, S.; Lim, Y. T.; Soltesz, E. G.; De Grand, A. M.; Lee, J.; Nakayama, A.; Parker, J. A.; Mihaljevic, T.; Laurence, R. G.; Dor, D. M.; Cohn, L. H.; Bawendi, M. G.; Frangioni, J. V. *Nature biotechnology* **2004,** 22, (1), 93-7.

34. Hessel, C. M.; V, P. P.; Rasch, M.; Panthani, M. G.; Koo, B.; Tunnell, J. W.; Korgel, B. A. *Nano Lett* **2011,** 11, (6), 2560-6.

35. Murray, C. B.; Kagan, C. R.; Bawendi, M. G. *Annual Review of Materials Science* **2000,** 30, (1), 545-610.

36. Cozzoli, P. D.; Pellegrino, T.; Manna, L. *Chemical Society reviews* **2006,** 35, (11), 1195-208.

37. Mekis; I; Talapin; D, V.; Kornowski; A; Haase; M; Weller; H. *Journal of Physical Chemistry B* **2003,** 107, (30), 7454-7462.

38. Talapin; D, V.; Mekis; I; Gotzinger; S; Kornowski; A; Benson; O; Weller; H. *Journal of Physical Chemistry B* **2004,** 108, (49), 18826-18831.

39. Steckel, J. S.; Zimmer, J. P.; Coe-Sullivan, S.; Stott, N. E.; Bulovic, V.; Bawendi, M. G. *Angew Chem Int Ed Engl* **2004,** 43, (16), 2154-8.

40. Talapin; D, V.; Koeppe; R; Gotzinger; S; Kornowski; A; Lupton; J, M.; Rogach; A, L.; Benson; O; Feldmann; J; Weller; H. *Nano Letters* **2003,** 3, (12), 1677-1681.

41. Luther, J. M.; Zheng, H.; Sadtler, B.; Alivisatos, A. P. *J Am Chem Soc* **2009,** 131, (46), 16851-7.

42. Sadtler, B.; Demchenko, D. O.; Zheng, H.; Hughes, S. M.; Merkle, M. G.; Dahmen, U.; Wang, L. W.; Alivisatos, A. P. *J Am Chem Soc* **2009,** 131, (14), 5285-93.

43. Dorn, A.; Allen, P. M.; Harris, D. K.; Bawendi, M. G. *Nano Lett* **2010,** 10, (10), 3948-51.

44. Jain, P. K.; Amirav, L.; Aloni, S.; Alivisatos, A. P. *J Am Chem Soc* **2010,** 132, (29), 9997-9.

45. Kim, S.; Fisher, B.; Eisler, H. J.; Bawendi, M. *J Am Chem Soc* **2003,** 125, (38), 11466-7.

46. Schrier, J.; Demchenko, D. O.; Wang, L. W.; Alivisatos, A. P. *Nano Lett* **2007,** 7, (8), 2377-82.

47. Shevchenko, E. V.; Talapin, D. V.; O'Brien, S.; Murray, C. B. *Journal of the American Chemical Society* **2005,** 127, (24), 8741-8747.

48. Bodnarchuk, M. I.; Kovalenko, M. V.; Heiss, W.; Talapin, D. V. *Journal of the American Chemical Society* **2010,** 132, (34), 11967-11977.

49. Zanella, M.; Bertoni, G.; Franchini, I. R.; Brescia, R.; Baranov, D.; Manna, L. *Chem Commun (Camb)* **2011,** 47, (1), 203-5.

50. Baranov, D.; Fiore, A.; van Huis, M.; Giannini, C.; Falqui, A.; Lafont, U.; Zandbergen, H.; Zanella, M.; Cingolani, R.; Manna, L. *Nano Lett* **2010,** 10, (2), 743-9.

51. Talapin, D. V.; Shevchenko, E. V.; Murray, C. B.; Titov, A. V.; Král, P. *Nano Letters* **2007,** 7, (5), 1213-1219.

52. Engtrakul, C.; Kim, Y. H.; Nedeljkovic, J. M.; Ahrenkiel, S. P.; Gilbert, K. E.; Alleman, J. L.; Zhang, S. B.; Micic, O. I.; Nozik, A. J.; Heben, M. J. *The journal of physical chemistry. B* **2006,** 110, (50), 25153-7.

53. Mott, N. F., Conduction in Non-Crystalline Materials. In Oxford University Press, USA: 1987.

54. Mott, N. F., *Metal-Insulator Transitions*. 2 ed.; CRC Press: 1990.

55. Altshuler, B.; Aronov, A., *Electron-Electron Interactions in Disordered Conductors*. North-Holland, Amsterdam, 1985.

56. Shklovskii, B. I.; Shklovskiĭ, B. I.; Ėfros, A. L., *Electronic Properties of Doped Semiconductors*. Springer-Verlag: 1984.

57. Talapin, D. V.; Murray, C. B. *Science* **2005,** 310, (5745), 86-89.

58. Luther, J. M.; Law, M.; Song, Q.; Perkins, C. L.; Beard, M. C.; Nozik, A. J. *ACS nano* **2008,** 2, (2), 271-80.

59. Andres, R. P.; Bein, T.; Dorogi, M.; Feng, S.; Henderson, J. I.; Kubiak, C. P.; Mahoney, W.; Osifchin, R. G.; Reifenberger, R. *Science* **1996,** 272, (5266), 1323-1325.

60. Klein, D. L.; Roth, R.; Lim, A. K. L.; Alivisatos, A. P.; McEuen, P. L. *Nature* **1997,** 389, (6652), 699-701.

61. Zylbersztejn, A.; Mott, N. F. *Physical Review B* **1975,** 11, (11), 4383.

62. Yu, D.; Wang, C.; Wehrenberg, B. L.; Guyot-Sionnest, P. *Physical review letters* **2004,** 92, (21), 216802.

63. Law, M.; Beard, M. C.; Choi, S.; Luther, J. M.; Hanna, M. C.; Nozik, A. J. *Nano Lett* **2008,** 8, (11), 3904-10.

64. Lee, J.-S.; Kovalenko, M. V.; Huang, J.; Chung, D. S.; Talapin, D. V. *Nature Nanotechnology* **2011,** 6, (6), 348-352.

65. Yu, D.; Wang, C.; Guyot-Sionnest, P. *Science* **2003,** 300, (5623), 1277-1280.

66. Urban, J. J.; Talapin, D. V.; Shevchenko, E. V.; Kagan, C. R.; Murray, C. B. *Nature materials* **2007,** 6, (2), 115-21.

67. Lee, J.-S.; Shevchenko, E. V.; Talapin, D. V. *Journal of the American Chemical Society* **2008,** 130, (30), 9673-9675.

Chapter 2: Synthesis of Colloidal $CuInS_2$, $CuInSe_2$, and $CuIn_XGa_{1-X}Se_2$, and Cu_2ZnSnS_4 Nanocrystals†

2.1. INTRODUCTION

I−III−VI_2 chalcopyrite compounds, particularly copper indium gallium selenide ($Cu(In_xGa_{1-x})Se_2$; CIGS), are effective light-absorbing materials in thin-film solar cells.[1] These materials possess advantageous properties for solar applications: their band gap energy is at the red edge of the solar spectrum; they are direct band-gap semiconductors with correspondingly high optical absorption coefficients and CIGS materials, in contrast to other candidate materials for thin-film solar cells such as CdTe and amorphous silicon (a-Si), are stable under long-term excitation.[2] High efficiency CIGS-based devices are typically fabricated using polycrystalline films, and single-junction CIGS solar cells have demonstrated over 20% solar energy conversion efficiency,[1] which is significantly higher than either CdTe or a-Si based devices. Furthermore, CIGS devices and manufacturing processes may have less environmental impact than those with thin film materials with large amounts of Cd and Pb, like CdTe and PbSe based solar cells, although to date the highest efficiency CIGS photovoltaic (PV) devices have nonetheless required CdS buffer layers.

One of the hurdles currently impeding widespread commercialization of CIGS-based solar cells is the difficulty in achieving controlled stoichiometry over large device areas, leading to high manufacturing costs and poor device yield. CIGS layers in state-of-

† Portions of this chapter appear in *Journal of the American Chemical Society* 130(49), 16770-16777 (**2011**) and *Journal of the American Chemical Society* 131(35), 12554-12555 (**2009**).

the-art devices are deposited by a multistage coevaporation process in which alternate copper, indium, and gallium layers are deposited followed by reacting with a selenium source, Se, or H_2Se gas, in the chamber. This process is time-consuming and the CIGS stoichiometry is difficult to control; intermetallic phases can form and the Se content can vary significantly in the films. Large material losses on the deposition chamber walls also increase cost. For all of these reasons, alternative CIGS layer deposition strategies are desired.

One approach with the potential to produce CIGS layers with controlled stoichiometry without the need for high temperature annealing is to chemically synthesize CIGS nanocrystals with controlled stoichiometry and crystal phase and disperse them in solvents, creating a paint or ink. Such an approach of printable CIGS inks makes accessible a range of solution-based processing techniques and may lead to inexpensive fabrication routes for CIGS light-absorbing layers.) A chemical, solution-based approach alleviates the need for a high temperature annealing step under selenium atmosphere and may solve the CIGS "selenium problem" - that is, avoiding Se loss and achieving the correct CIGS stoichiometry in films covering large substrate areas.[3] Photovoltaic devices incorporating nanocrystalline-based CdSe/CdTe[4] and CuS[5] absorber layers have been reported and demonstrated solar energy conversion efficiencies as high as 2.9%, although a high temperature anneal at 400 °C was required. Semiconductor nanocrystals have also been combined with polymers to produce solution-processed photovoltaics, such as hybrid CdSe nanocrystal/poly-3(hexylthiophene) solar cells, which yield reported efficiencies of up to 1.7%.[6] Many different semiconductor

nanocrystals can be synthesized by colloidal routes, including groups II−VI,[7] III−V,[8] I−VI.[5] IV−VI,[9] and IV semiconductors,[10-12] but the synthesis of I−III−VI_2 nanocrystals is much less developed. Nonetheless, there are literature reports of the synthesis of ternary chalcopyrite compound nanocrystals, such as $CuInS_2$, $CuInSe_2$, and other I−III−VI_2 semiconductor nanocrystals such as $AgInS_2$.[13] These nanocrystals, however, generally suffer from relatively low yields, poor crystallinity, and poor uniformity in composition and phase. This is not surprising considering that many of these systems have very complicated phase diagrams and nanocrystals can further exhibit greater phase complexity than the corresponding bulk materials.[14]

2.2. NANOCRYSTAL SYNTHESIS

2.2.1. $CuInS_2$ Nanocrystal Synthesis

A 0.26 g (1 mmol) portion of $Cu(acac)_2$ and 0.41 g (1 mmol) of $In(acac)_3$ are added to 7 mL of DCB in a 25 mL three-neck flask in air. In a separate 25-mL three-neck flask, 0.064 g (2 mmol) of elemental sulfur is dissolved in 3 mL of DCB in air. Both flasks are then attached to a Schlenk line and purged of oxygen and water by pulling vacuum at room temperature for 30 min, followed by N_2 bubbling at 60 °C for 30 min. Between 0.5 and 2 mL (1.5 to 6 mmol) of OLA are added to the (Cu, In)-DCB mixture and both flasks are heated to 110 °C and combined, maintaining a N_2 flow. The reaction mixture is refluxed (~182 °C) for 1 h under N_2 flow. The reaction is allowed to cool to room temperature, and the nanocrystals are separated by adding excess ethanol. The yield of solution-stable nanocrystals after purification was ~90%.

2.2.2. $CuInSe_2$ Nanocrystal Synthesis

2.2.2.1. $CuInSe_2$ Nanocrystal Synthesis using elemental Se

In a nitrogen-filled glovebox, 1 mmol of CuCl (0.099 g), 1 mmol of $InCl_3$(0.221 g), and 2 mmol of elemental Se (0.158 g) are combined in a 25-mL three-neck flask with an attached condenser and stopcock valve. The stopcock valve is closed before removing the flask from the glovebox, where it is attached to a Schlenk line and placed on a heating mantle. OLA (10 mL) stored in air is injected into the flask. The flask is purged of oxygen and water by pulling vacuum at 60 °C for 1 h, followed by N_2 bubbling at 110 °C for 1 h while stirring. The mixture is then heated to 200 °C for 10 min. followed by 260°C for 30 min under vigorous stirring. The reaction is cooled to ~100 °C, where ~10 mL of chloroform is added to quench the reaction and ~5 mL of ethanol is added to precipitate the nanocrystals. After adding the ethanol, the reaction mixture is immediately removed and placed in a centrifuge tube. A significant amount of poorly capped and large (up to 200 nm diameter) nanocrystals are found in the crude reaction product, which is separated from the well-capped nanocrystals. The typical product yield of the well-dispersed $CuInSe_2$ nanocrystals was ~80%. Arrested precipitation procedures in which OLA complexes of Cu, In, and Se were formed separately and then combined at high temperature yielded nanocrystals that were very unstable when purified and redispersed.

2.2.2.1. $CuInSe_2$ Nanocrystal Synthesis using Tributylphosphine selenide

In a nitrogen-filled glovebox, 1 mmol of CuCl (0.099 g), 1 mmol of $InCl_3$(0.221 g) are combined in a 25-mL three-neck flask with an attached condenser and stopcock

valve inside of glovebox. Dry OLA (10 mL) stored in a glovebox is injected into the flask. The stopcock valve is closed before removing the flask from the glovebox, where it is attached to a Schlenk line and placed on a heating mantle. The flask is purged o by pulling vacuum at 60 °C for 1 h, followed by N_2 bubbling at 110 °C for 1 h while stirring. During this heating, the precursor powders dissolve in oleylamine forming a yellow-orange solution. The mixture is then heated to 180°C, and 2 mL of 1M tributylphosphine selenide is injected into the solution, and the orange solution immediately begins to turn brown. The flask is heated to 240°C and allowed to react for 30 min. The reaction is cooled to 100 °C, where 10 mL of chloroform or toluene is added to quench the reaction and ~5 mL of ethanol is added to precipitate the nanocrystals. After adding the ethanol, the reaction mixture is immediately removed and placed in a centrifuge tube. Reactions carried out for less than 4 h yielded nanocrystals with a larger size distribution and more agglomeration when dispersed after purification. A significant amount of poorly capped and large (up to 200 nm diameter) nanocrystals are found in the crude reaction product, which is separated from the well-capped nanocrystals. The typical product yield of the well-dispersed $CuInSe_2$ nanocrystals was ~10%. Arrested precipitation procedures in which OLA complexes of Cu, In, and Se were formed separately and then combined at high temperature yielded nanocrystals that were very unstable when purified and redispersed.

2.2.3. Cu(In,Ga)Se_2 Nanocrystal Synthesis

A typical reaction is carried about by adding 1 mmol of CuCl (0.099 g), 2 mmol of elemental Se (0.158 g), and 1 mmol total of $InCl_3$ (0.00 to 0.221 g) and $GaCl_3$ (0.00 to 0.111 g) to a 25-mL three-neck flask with attached condenser and stopcock valve in a nitrogen-filled glovebox. The stopcock valve is closed before removing the flask from the glovebox, where it is attached to a Schlenk line and placed on a heating mantle. OLA (10 mL) is injected into the flask. The flask is purged of oxygen and water by pulling vacuum at 60 °C for 1 h, followed by N_2 bubbling at 110 °C for 1 h while stirring. The mixture is then heated to 240 °C, and the reaction proceeds for 4 h under vigorous stirring. The product yield of $CuIn_xGa_{1-x}Se_2$nanocrystals with $x < 1$ ranged from 20%−60% after purification. Using trialkylphosphines in this reaction results in poor control of Ga concentration in the nanocrystals.

2.2.4. Synthesis of Cu_2ZnSnS_4 (CZTS) Nanocrystals

In a typical reaction, 0.52 g of $Cu(acac)_2$ (99.99+%), 0.29 g of zinc acetate (99.99%), 0.18 g of $SnCl_2$ (99.99+%), 0.13 g of S (99.98%) were added to 40 mL of OLA (70%) in a 100 mL three-neck flask on a Schlenk line. The reaction mixture was degassed under vacuum for 2 h, purged with N_2 for 30 min at 110 °C, heated to 280 °C for 1 h, and then cooled to room temperature. The nanocrystals were then isolated by precipitation with ethanol followed by centrifugation. Solid reaction byproducts and poorly capped nanocrystals were removed by redispersion in chloroform and centrifugation at 8000 rpm for 2 min. The nanocrystals were washed three more times by

solvent/antisolvent precipitation with chloroform/ethanol. A typical reaction yielded 200 mg of nanocrystals.

2.2.5. Synthesis of Quantum-confined $CuInS_XSe_{2-X}$ Nanocrystals

In a typical reaction, 5 mmol $Cu(acac)_2$ (1.3g), 5mmol $In(acac)_3$ (2.5 g), 20 mL ODE and 10 mL DDT are placed in a 100 mL 3-neck round bottom flask equipped with a magnetic stir bar. The flask is connected to a condenser and sealed with rubber septa. A thermocouple is inserted through one septum to measure the solution temperature. The flask is attached to a Schlenk line and is heated with a heating mantle. The contents are first put under vacuum (~300 mTorr) and heated to 110ºC for 1 hr while stirring. The dispersion, which is initially blue and opaque, transforms into a transparent yellow, viscous solution as it is heated. After 1 hr, the solution ceases to bubble, indicating that all moisture is removed and the flask is thoroughly degassed. The flask is then put under a N_2 atmosphere and the temperature is quickly ramped to 180ºC, where immediately 10 mL of 1M TBP:Se is injected rapidly. Upon injection the temperature drops to ~160 ºC and the flask contents becomes almost colorless. The temperature is then ramped to 220ºC, and aliquots are taken along the course of the reaction. Reaction temperatures over 240ºC lead to uncontrolled growth, with a final product containing mostly large precipitates with no observed photoluminescence. The solution color is initially pale yellow, and as time goes on the color progresses from yellow to orange, red, and finally dark brown. Aliquots were taken to monitor the photoluminescence peak. The photoluminescent quantum yield of these aliquots were typically between 5 and 10%. A

ZnS shell precursor solution was prepared by combining zinc bis(ethyl xanthogenate) (100 mg), zinc (II) oleate (900 mg). ODE (10 mL), trioctylphosphine (3 mL) and oleylamine (1 mL). The CISS nanocrystals are coated with ZnS by cooling the reaction solution to 190ºC and injecting this solution into the reaction flask. The mixture is stirred overnight to allow the shell to form. The heating mantle is removed and the mixture is allowed to cool to room temperature. The nanocrystals are precipitated by adding an ethanol/toluene (~2:1 vol:vol) mixture and centrifuging at 8000 rpm for 5 min. Addition of only ethanol as an antisolvent is not effective because ethanol is not miscible in octadecene, and the mixture phase segregates.

2.2.6. Nanocrystal Purification

The nanocrystal products were purified by precipitation with excess ethanol followed by centrifugation at 8000 rpm for 10 min. After such a washing step, the supernatant contains unreacted precursor and byproducts and is discarded. The nanocrystals are in the precipitate. The nanocrystals are then redispersed in 10 mL of chloroform and centrifuged at 7000 rpm for 5 min to remove poorly capped nanocrystals and large particulates, which settle during centrifugation. The well-capped nanocrystals remain dispersed in the supernatant. The precipitate is discarded and a small amount of OLA (0.2 mL) is subsequently added to the supernatant to ensure complete surface passivation of the nanocrystals. To remove excess capping ligands and remaining impurities, the product is again precipitated using ~5 mL of ethanol and centrifuged at 8000 rpm for 10 min, then redispersed in chloroform. This process is done three times to

obtain a high-purity product. The isolated nanocrystals disperse in various nonpolar organic solvents, including hexane, toluene, decane, chloroform, and TCE.

2.3. RESULTS AND DISCUSSION

2.3.1. $CuInS_2$ Nanocrystals

$CuInS_2$ nanocrystals were synthesized using a variation of the procedure developed by Ghezelbash and Korgel for CuS nanocrystals,[14] by adding $In(acac)_3$ as an In source to the reaction: Elemental sulfur dissolves in dichlorobenzene and could be used directly as the sulfur source. Figure 2.1 shows TEM images of $CuInS_2$ nanocrystals. The nanocrystal size could be roughly controlled by varying the OLA/metal ratio. Figure 2.1 shows $CuInS_2$ nanocrystals with two different average diameters obtained by varying the OLA/metal ratio in the reaction. The average nanocrystal diameter was increased from 6 to 12 nm as the OLA/metal ratio by decreasing the ratio from 6:1 to 3:1. The nanocrystal shape was not perfectly spherical, which contributed to the relatively broad size distributions of the nanocrystals.

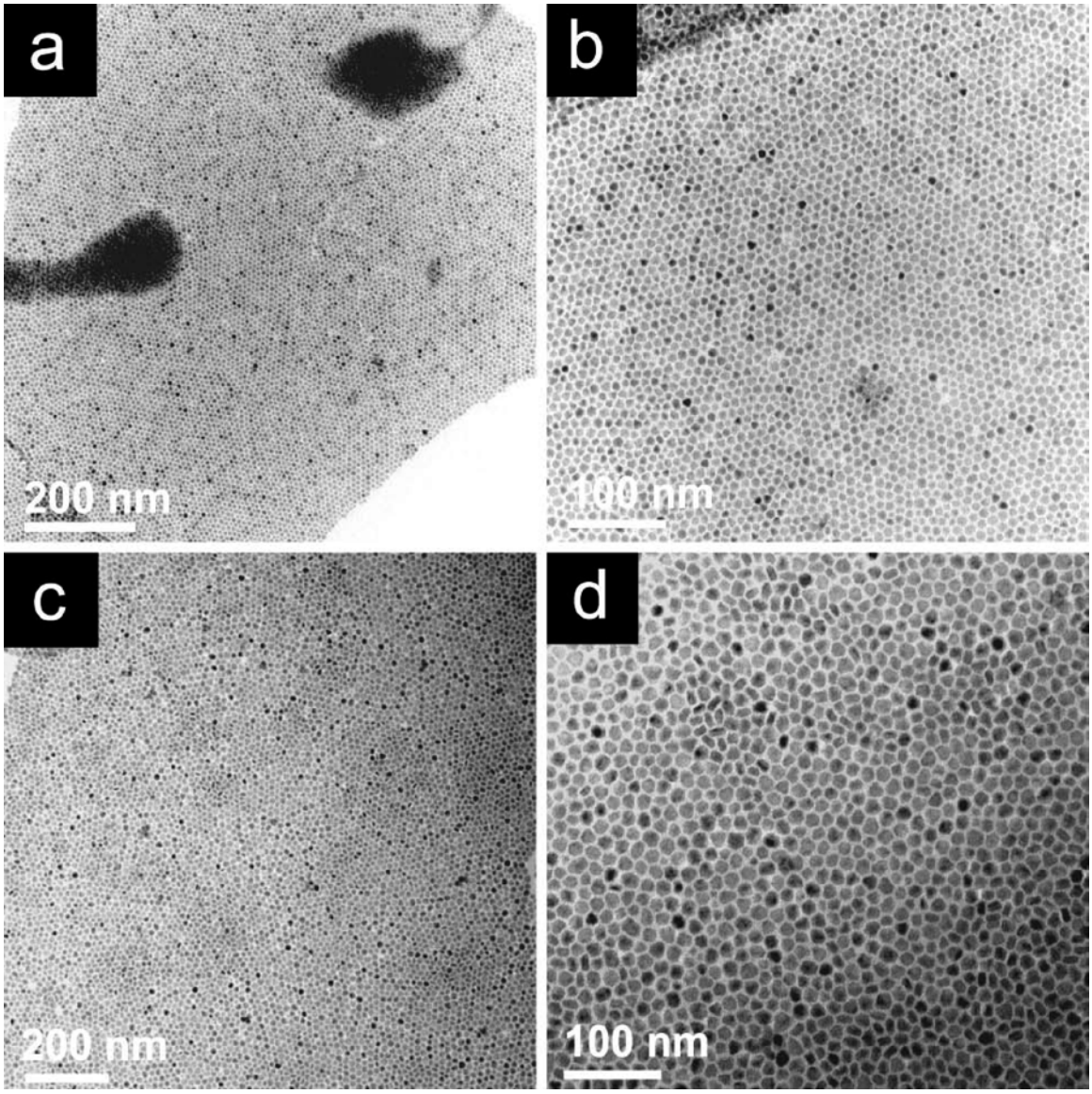

Figure 2.1. TEM images of $CuInS_2$ nanocrystals synthesized with varying OLA/(Cu+In) mole ratios: (a,b) 6:1, 8 nm diameter; (c,d) 3:1, 12 nm diameter.

High resolution TEM (Figure 2.2) showed the crystallinity of the nanocrystals, with lattice spacings corresponding to tetragonal $CuInS_2$.

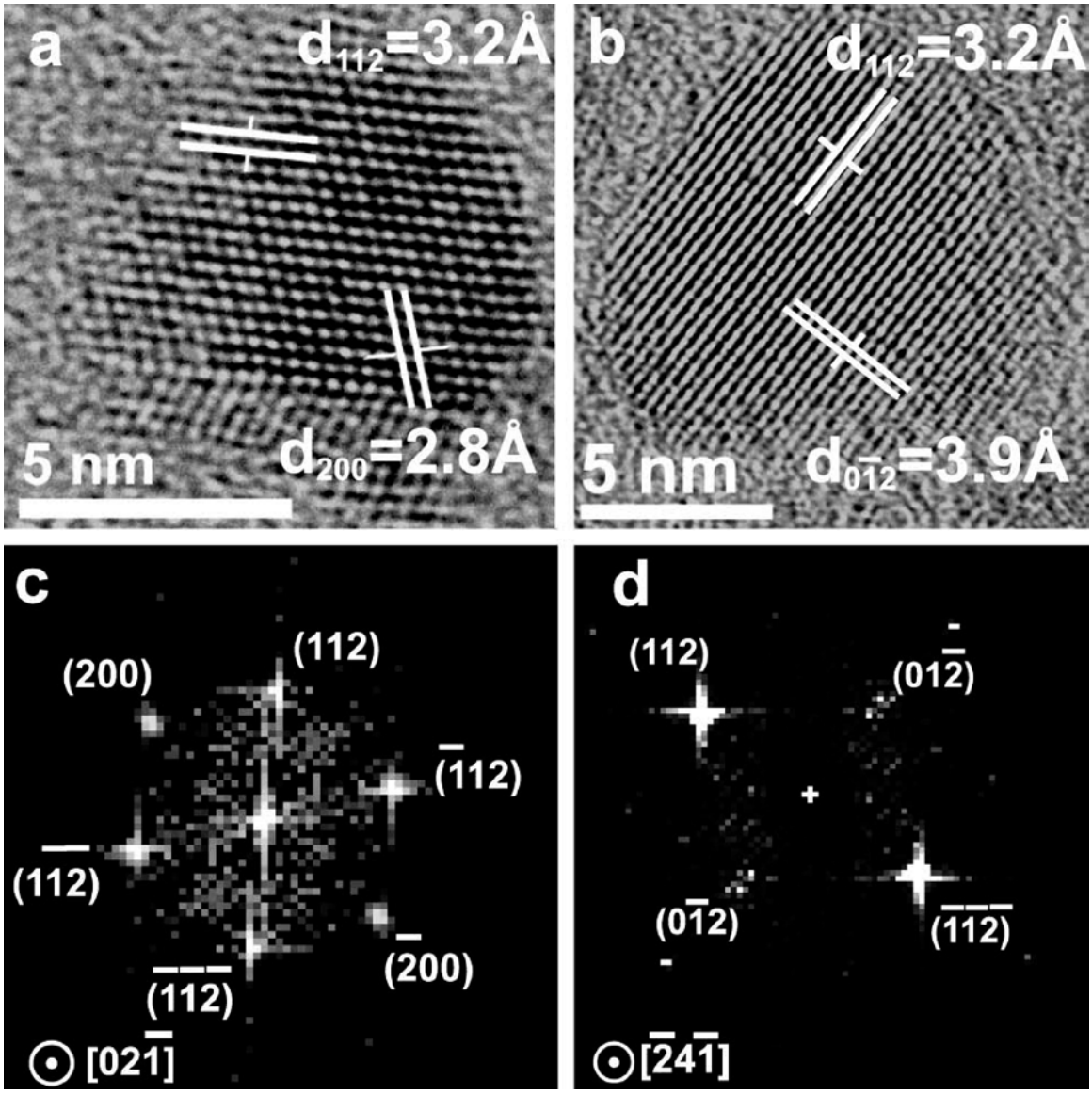

Figure 2.2. HRTEM images of a $CuInS_2$ Nanocrystals (a,b) and their respective fast Fourier transforms (FFTs) (c,d). The *d*-spacings correspond to chalcopyrite (tetragonal) $CuInS_2$.

XRD (Figure 2.3) confirmed that the nanocrystals are chalcopyrite (tetragonal) $CuInS_2$ and that no other phases are produced in the reaction. EDS from fields of

nanocrystals gave an average Cu/In/S composition of 0.29:0.25:0.46, which is near the target 0.25:0.25:0.5 ratio, considering the error of the EDS detector (approximately ±2 atom %) and that Cu is slightly overrepresented in the EDS spectra because of signal from the Cu sample holder. There was no compositional variation from particle to particle within the error of the EDS detector.

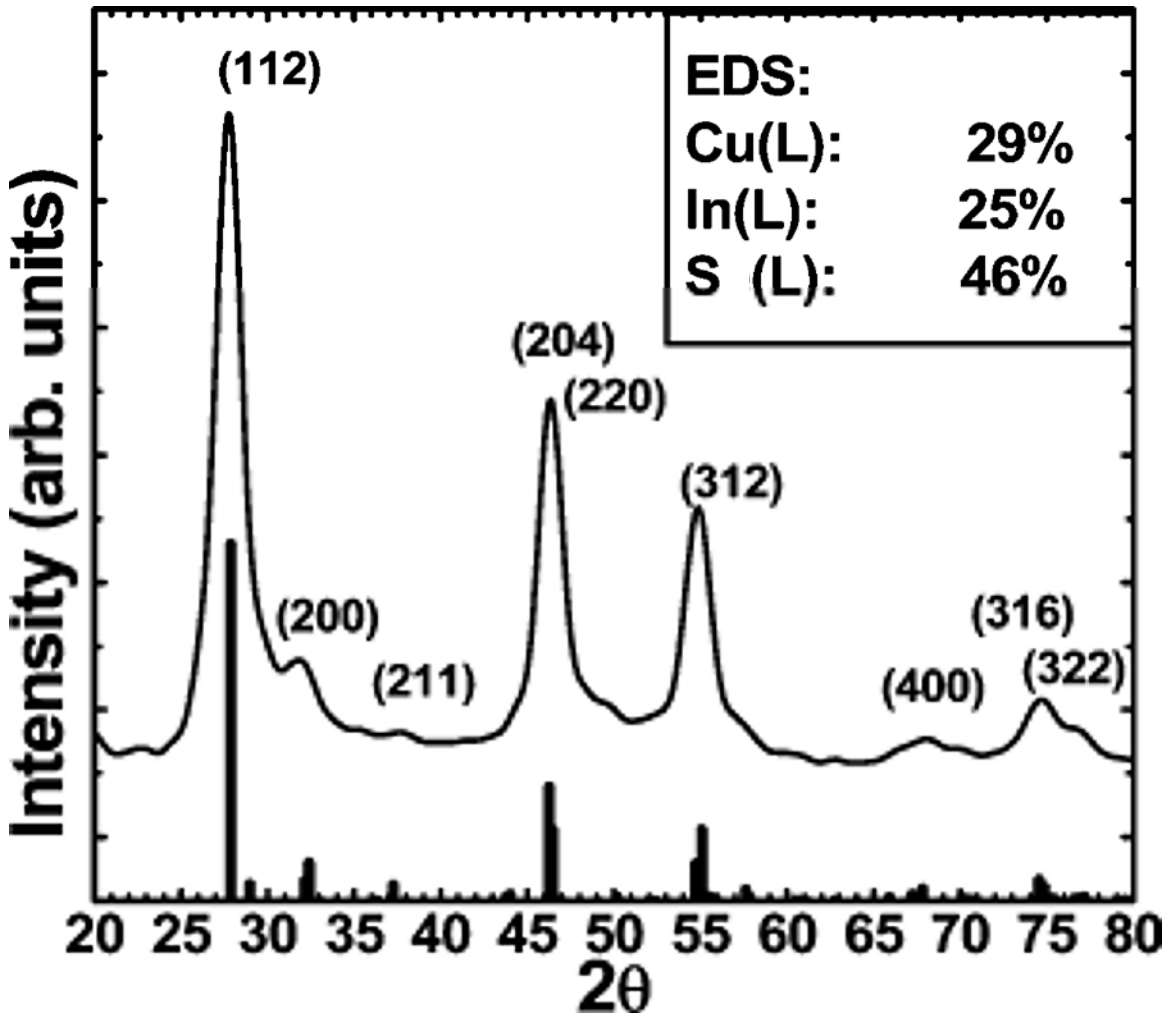

Figure 2.3. XRD and (inset) elemental composition measured by EDS of 8 nm diameter $CuInS_2$ nanocrystals. The peak labels correspond to those of chalcopyrite (tetragonal) $CuInS_2$ (JCPDS No. 085-1575).

The band gap energy determined from absorbance spectra (Figure 2.4) of optically clear (i.e., nonscattering) dispersions of nanocrystals was found to be 1.29 eV (960 nm), which

is within the range of the $CuInS_2$ band gap energy (which has been reported to lie between 1.2 and 1.5 eV) reported in literature.

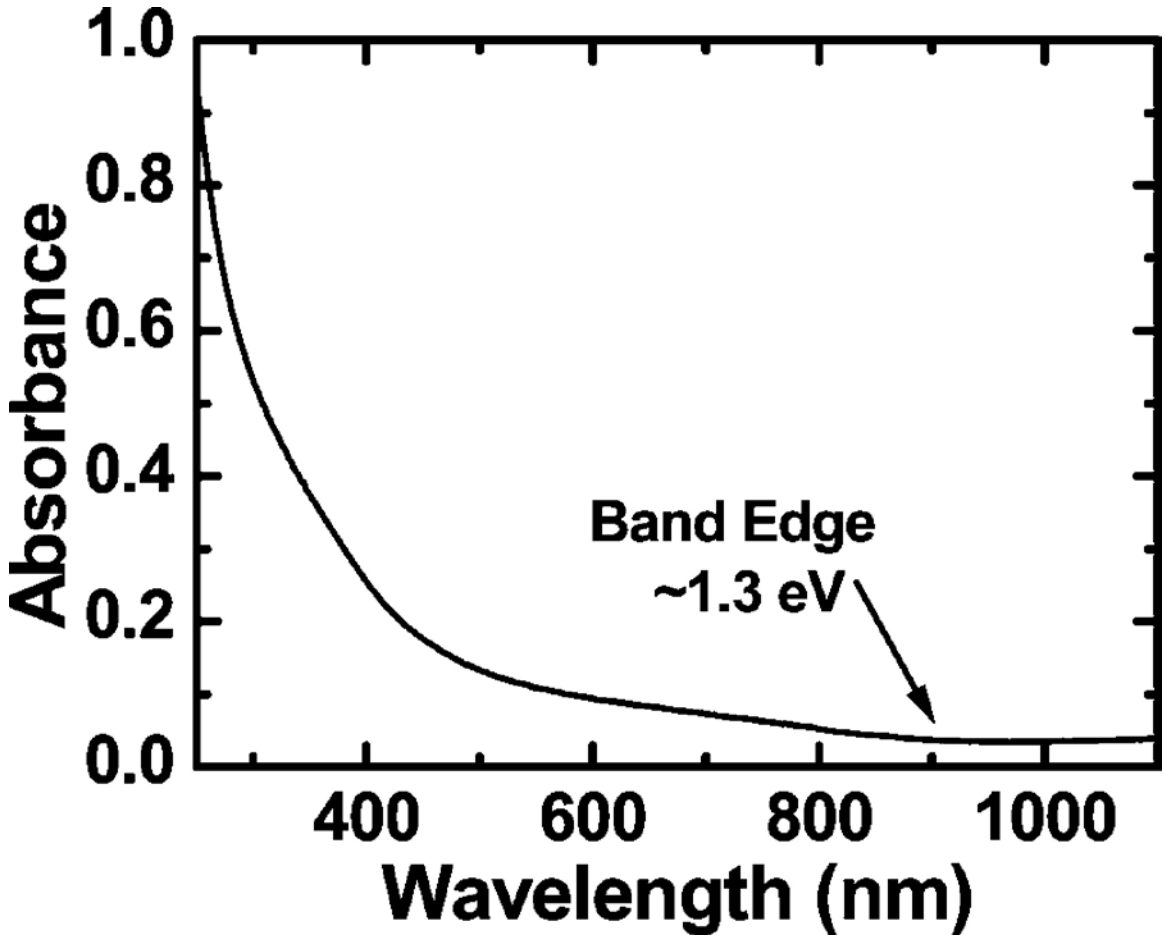

Figure 2.4. Room temperature absorbance spectrum of 8 nm diameter $CuInS_2$ nanocrystals dispersed in hexane.

2.3.2. $CuInSe_2$ Nanocrystals

$CuInSe_2$ nanocrystals could not be synthesized using an approach similar to $CuInS_2$ because unlike S, Se does not dissolve in dichlorobenzene. After exploring a variety of different reaction approaches, one effective route was a direct combination of

Cu and In salts and solid Se in a flask with oleylamine followed by heating to 240 °C for 4 h. Figure 2.5 shows TEM images of a typical $CuInSe_2$ nanocrystal preparation. The nanocrystals are approximately 15 nm in diameter.

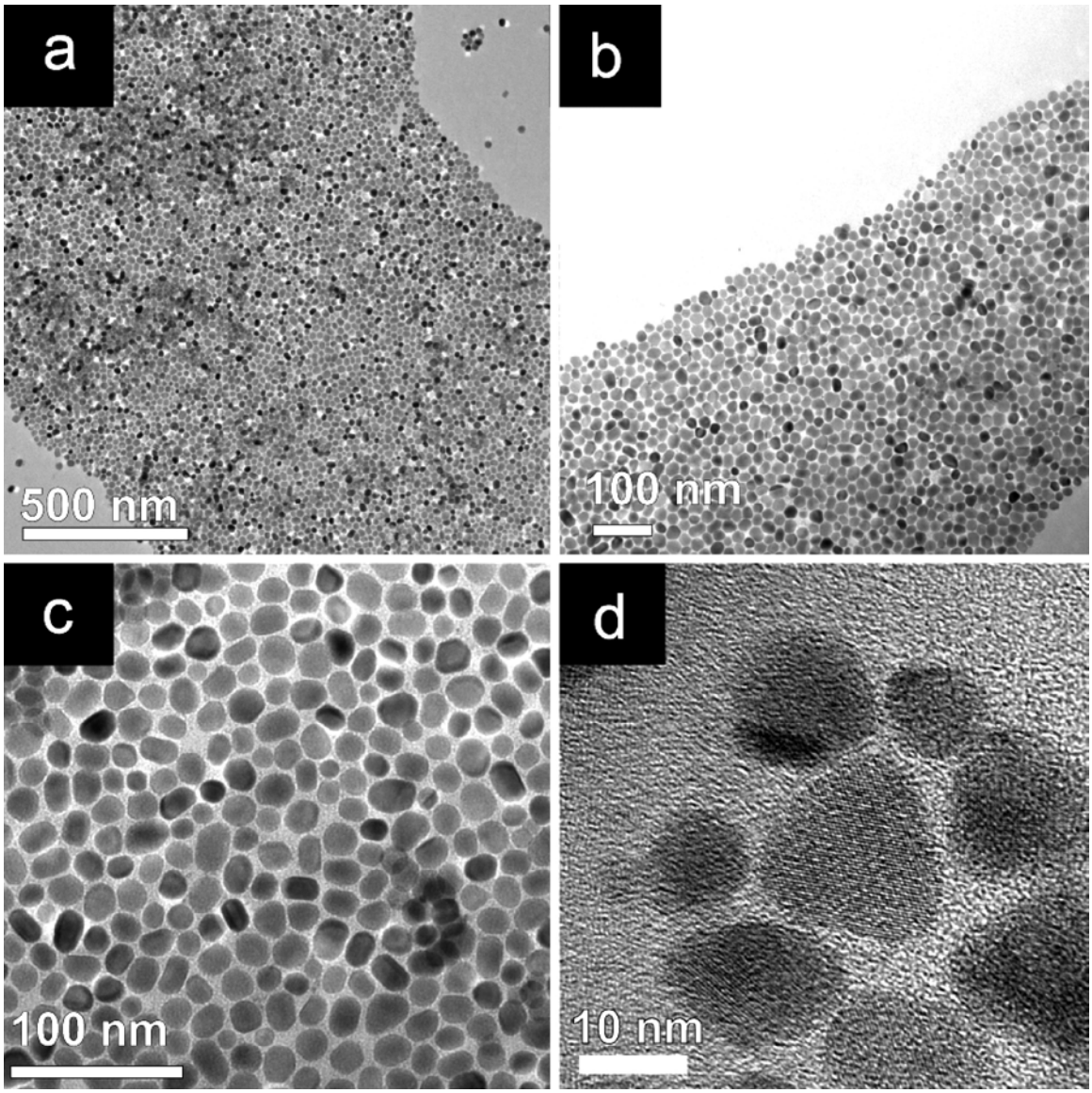

Figure 2.5. TEM images of $CuInSe_2$ nanocrystals with an average diameter of 15 nm.

Both high-resolution TEM (Figure 2.6) and XRD (Figure 2.7) confirmed that the nanocrystals are crystalline with tetragonal chalcopyrite $CuInSe_2$ structure. The *d*-spacings observed in TEM and the FFTs of the TEM images are also consistent with tetragonal $CuInSe_2$.

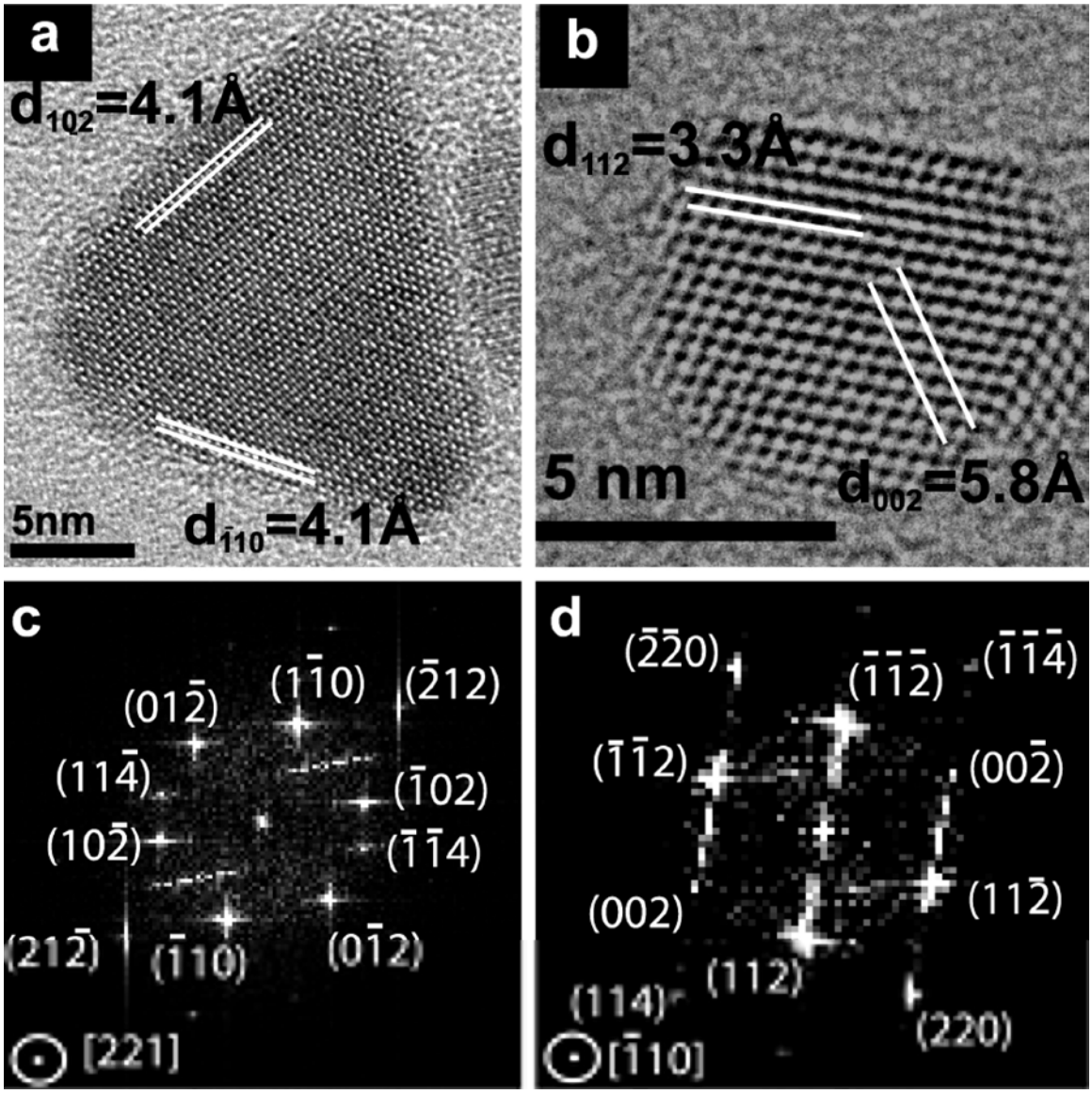

Figure 2.6. (a,b) HRTEM images of $CuInSe_2$ nanocrystals and (c,d) their FFTs. The observed *d*-spacings and the indexed FFTs are consistent with chalcopyrite (tetragonal) $CuInSe_2$.

No other crystal phases were observed in the XRD patterns of the product.

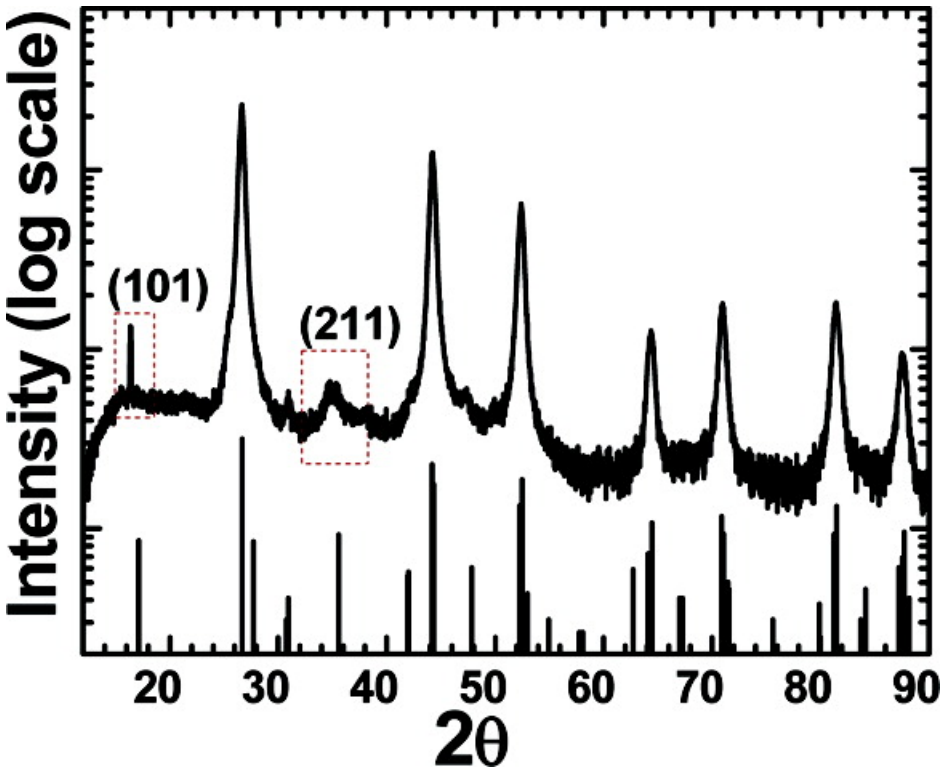

Figure 2.7. XRD pattern of chalcopyrite $CuInSe_2$ nanocrystals (JCPDS No. 00-040-1487). The scattering intensity is plotted on a logarithmic scale to elucidate the (211) peak. Dashed boxes indicate reflections that are unique to chalcopyrite ($CuInSe_2$).

Compositional analysis by ICPMS showed that the average composition of the nanocrystals in the sample has a molar Cu/In/Se ratio of 1:1:2 and the composition of individual particles measured by EDS was 1:1:2 with a variation from particle to particle less than the experimental error of ca. ±2 atom %.

Like the $CuInS_2$ nanocrystals, the $CuInSe_2$ nanocrystals are not spherical and exhibit significant faceting. The faceting has thus far been difficult to control, but this

might be addressed by the optimization of several factors, including the capping-ligand chemistry and the way reactants are added to the reaction. The relatively broad size distribution of the nanocrystals (ranging from as small as 5 nm to as large as 25 nm) is largely the result of this irregularity in particle shape.

2.3.3. $Cu(In_x,Ga_{1-x})Se_2$ (CIGS) Nanocrystals

CIGS nanocrystals were synthesized following the approach developed for $CuInSe_2$ nanocrystals, but with the addition of $GaCl_3$ to the reaction mixture in the desired In/Ga mole ratio.

The In/Ga ratio could be tuned across the entire stoichiometric range with *x* from 0 to 1 using this approach. Figure 2.8 shows TEM images of $CuIn_xGa_{1-x}Se_2$ with *x* ranging from 0.79 to 0.

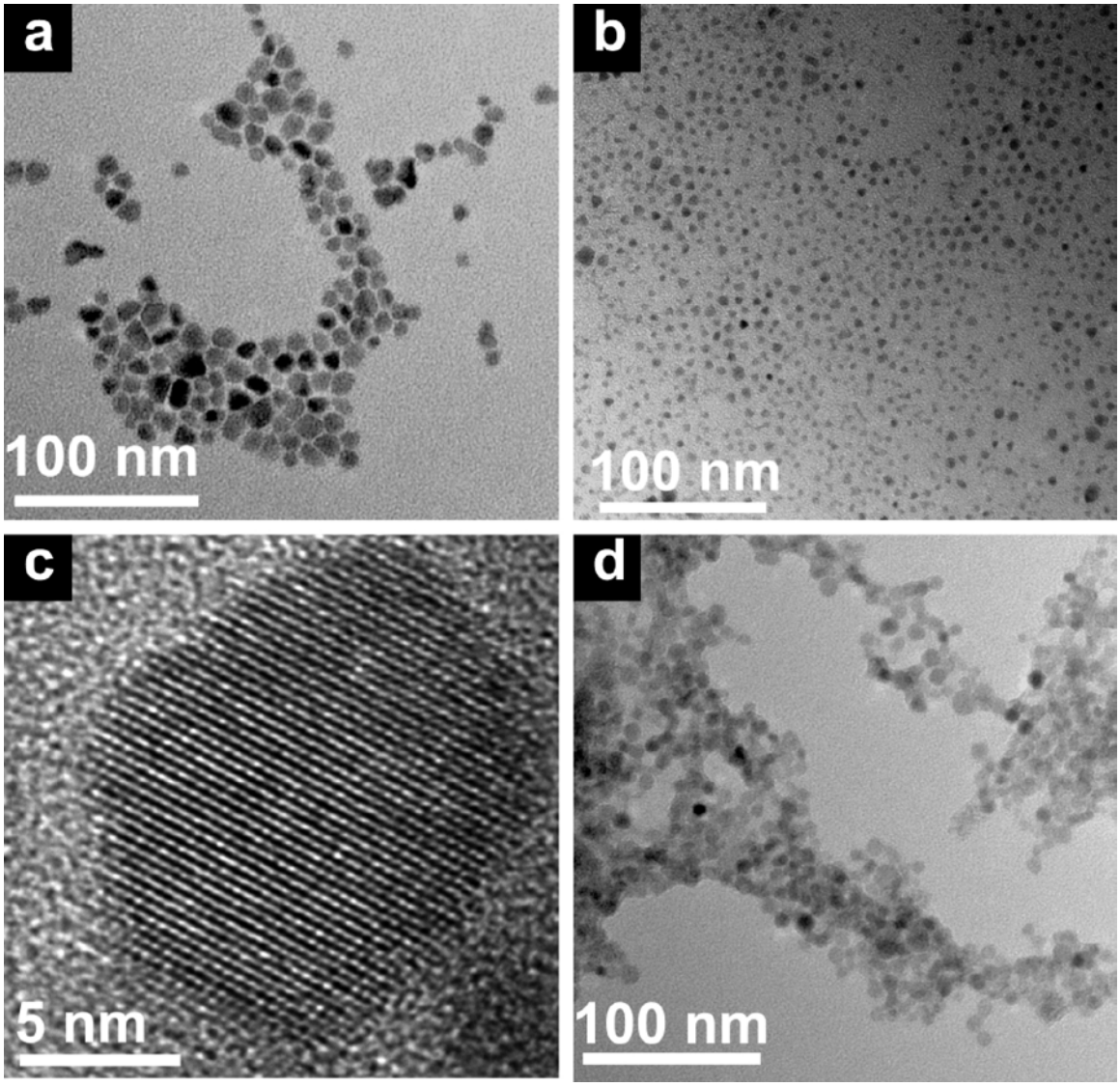

Figure 2.8. TEM images of $CuIn_XGa_{1-X}Se_2$ nanocrystals with (a) x = 0.79, (b) 0.56, (c) 0.21, and (d) 0.

Figures 2.9 and 2.10 show XRD data of CIGS nanocrystals synthesized with Ga/In ratios varying from 0 to 1. All of the patterns are consistent with chalcopyrite (tetragonal) crystal structure and exhibit the expected amount of peak broadening due to

their nanoscale crystal domain size. The diffraction peaks shift to higher 2θ with increasing Ga content, due to the decreased lattice spacing with smaller Ga atoms substituting for larger In atoms.

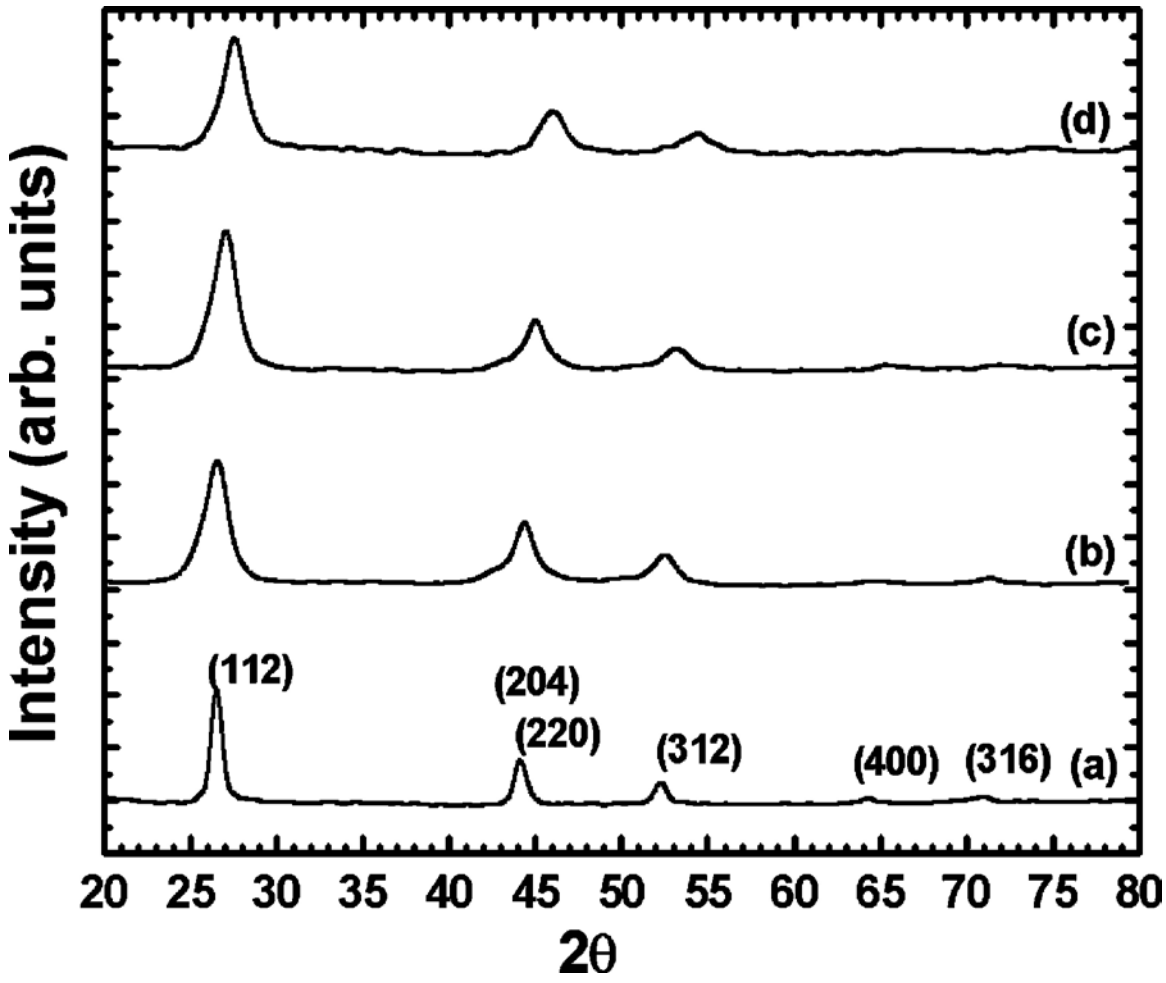

Figure 2.9. XRD patterns of CIGS nanocrystals synthesized with varying In:Ga ratios: (a) $CuInSe_2$ (b) $CuIn_{0.79}Ga_{0.21}Se_2$ (by EDS) (c) $CuIn_{0.51}Ga_{0.49}Se_2$ (by EDS) (d) $CuGaSe_2$ nanocrystals. The diffraction patterns correspond to those of the tetragonal chalcopyrite phases of the respective compounds. The indexing of the peaks noted in (a) correspond to the expected peaks positions of the chalcopyrite compounds.

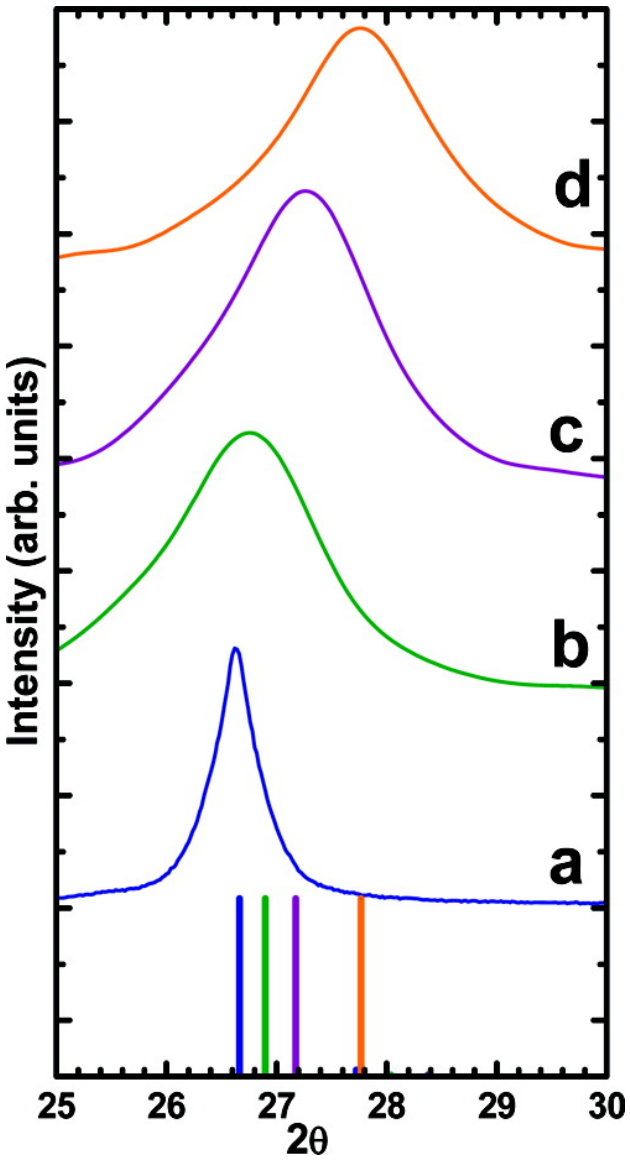

Figure 2.10. Magnification of the (112) XRD peaks from Figure 2.9 of the CIGS nanocrystals: (a) $CuInSe_2$ (b) $CuIn_{0.79}Ga_{0.21}Se_2$ (by EDS) (c) $CuIn_{0.51}Ga_{0.49}Se_2$ (by EDS) (d) $CuGaSe_2$ nanocrystals. The reference positions are for $CuInSe_2$ (JCPDS#00−040−1487), $CuIn_{07}Ga_{0.3}Se_2$ (JCPDS#00−035−1102), $CuIn_{0.5}Ga_{0.5}Se_2$ (JCPDS#00−040−1488), and $CuGaSe_2$ (JCPDS#00−031−0456).

The In/Ga ratio of the nanocrystals determined by ICPMS and EDS were consistent with the In/Ga mole ratio in the reaction mixture. Additionally, EDS measurements on different nanocrystals on the substrate did not show any noticeable variation in Cu/In/Ga ratio from particle to particle in the sample. Table 2.1 summarizes the synthesis results. The band gap energies of the $Cu(In_xGa_{1-x})Se_2$ nanocrystals determined from room temperature absorbance spectra (Figure 2.11) ($CuInSe_2$, 0.95 eV; $CuIn_{0.56}Ga_{0.44}Se_2$, 1.14 eV; $CuGaSe_2$, 1.51 eV) of nanocrystal dispersions were also consistent with energies of the corresponding bulk compounds: 0.95, 1.23, and 1.6 eV. The only noticeable difference in the nanocrystals with varying In/Ga ratio was that nanocrystals with higher Ga content were more difficult to stabilize in solution without aggregation. Particularly the $CuGaSe_2$ nanocrystals were not easily dispersible after isolation from the reaction mixture. More effective capping approaches to Ga-rich nanocrystals are desirable.

Table 2.1. Target ratios of precursors compared to measurements by EDS and ICPMS

Target Compound	precursor composition(atom ratio % Cu/In/Ga/Se)	composition measured by EDS (atom ratio % Cu/In/Ga/Se)	composition measured by ICPMS (atom ratio % Cu/In/Ga/Se)
$CuInSe_2$	25:25:50	29:25:0:46	25:25:0:50
$CuIn_{0.75}Ga_{0.25}Se_2$	25:19:6:50	25:18:5:52	26:15:9:50
$CuIn_{0.50}Ga_{0.50}Se_2$	25:13:12:50	27:14:12:47	26:13:11:50

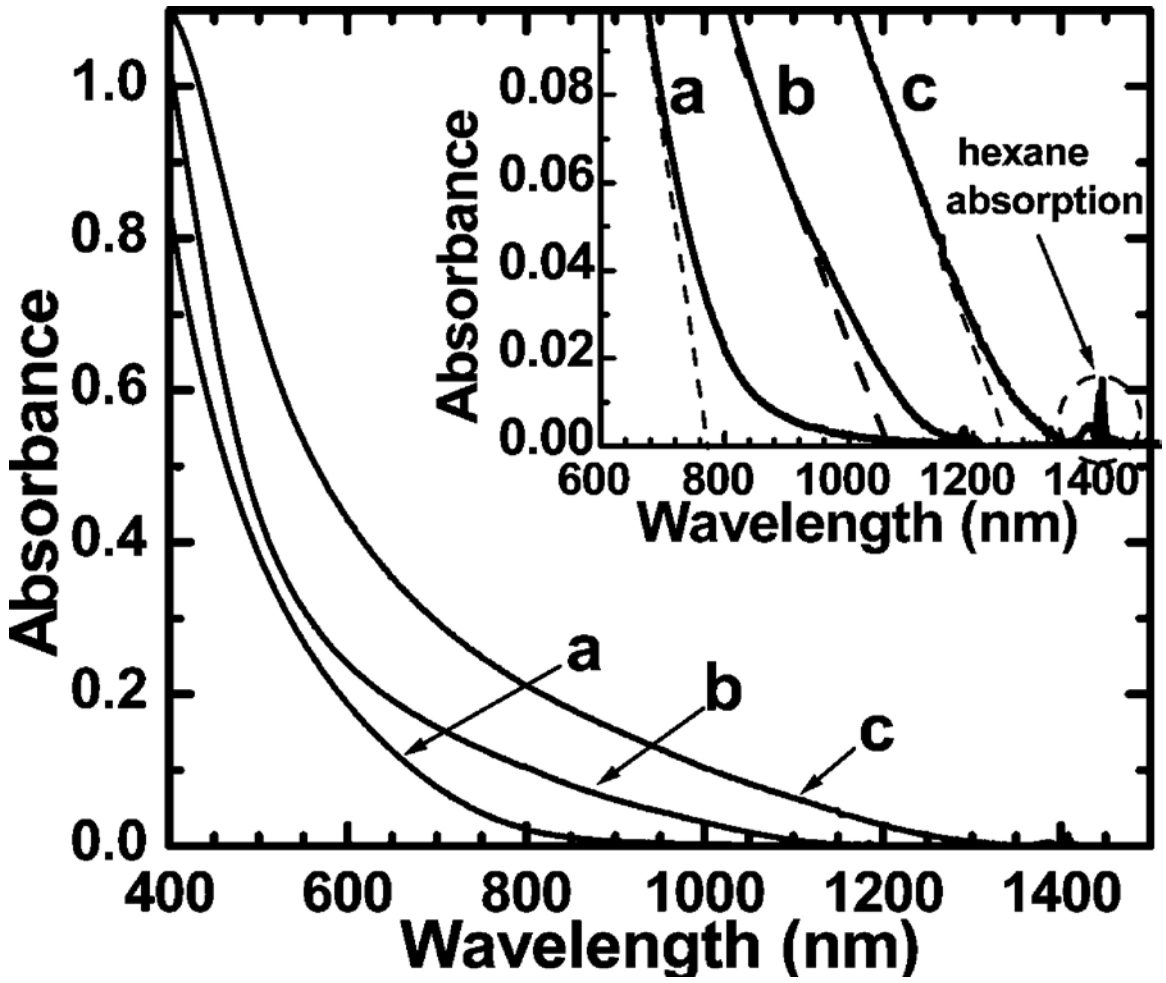

Figure 2.11. Room temperature absorbance spectra of Cu(InxGa1-x)Se2 nanocrystals dispersed in hexane. The curves correspond to In/Ga stoichiometries of (a) x = 0, (b) x = 0.56, and (c) x = 1. An extrapolation of the spectra to identify the band edge is shown in the inset. The small feature at ~1400 nm is related to the absorbance of hexane.

2.3.4. Cu_2ZnSnS_4 (CZTS) Nanocrystals

The CZTS nanocrystals were made by high-temperature arrested precipitation in the coordinating solvent, oleylamine (OLA). Copper(II) acetylacetonate [$Cu(acac)_2$], zinc acetate [$Zn(O_2CCH_3)_2$], tin(II) chloride dihydrate [$SnCl_2 \cdot 2H_2O$], and elemental sulfur (S) were combined in OLA and heated to 280 °C for 1 h under an inert atmosphere. Figure 2.12 shows transmission electron microscopy (TEM) and scanning electron microscopy (SEM) images of a typical CZTS nanocrystal sample. The particles are crystalline and have an average diameter of 10.6 ± 2.9 nm and a slightly irregular, faceted shape.

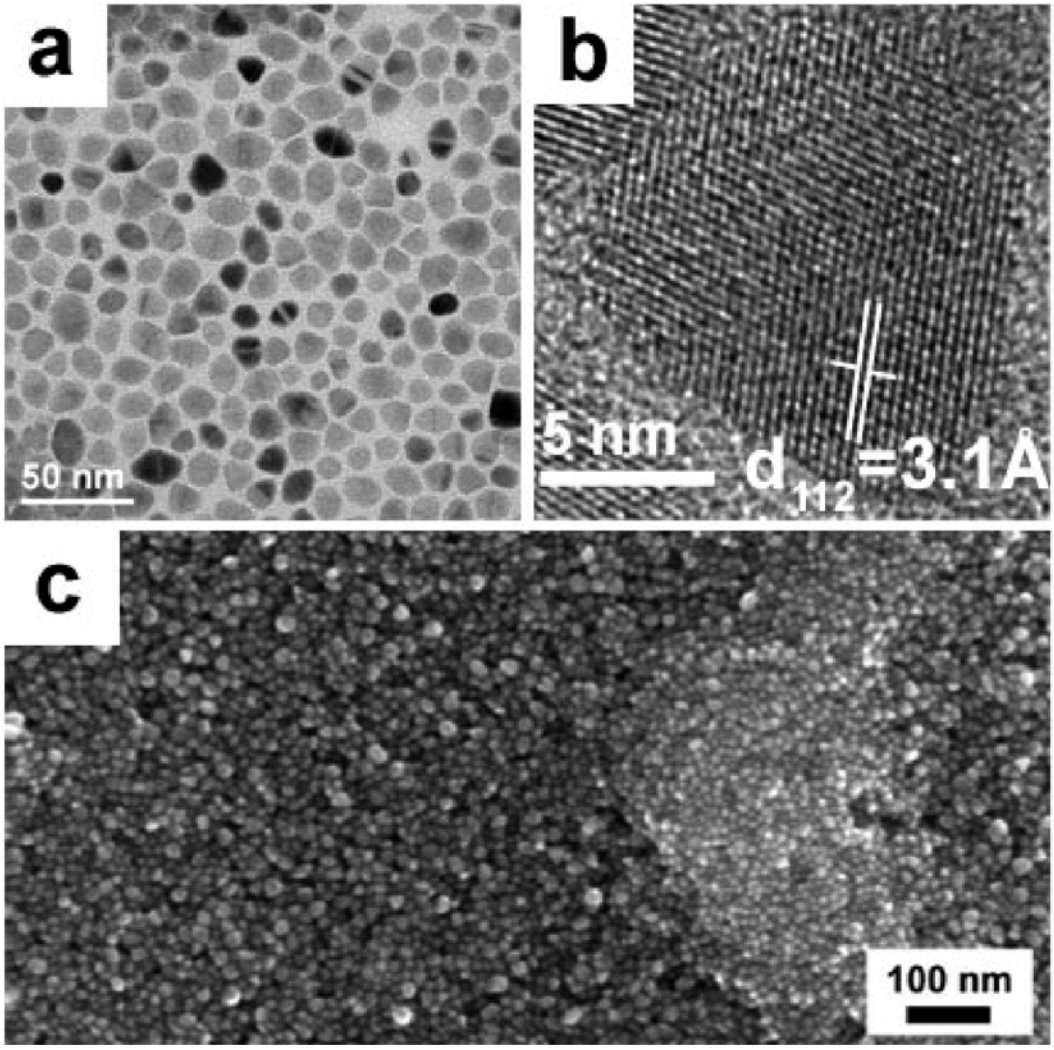

Figure 2.12. (a, b) TEM and (c) SEM images of CZTS nanocrystals. In (b), the nanocrystal is imaged down the [$1\bar{1}0$] crystallographic zone axis. TEM images and EDS data were obtained on carbon-coated Ni grids (200 mesh, Electron Microscopy Sciences) using a JEOL 2010F transmission electron microscope equipped with an Oxford INCA EDS detector. SEM images were obtained using gold-coated soda lime glass substrates with a Zeiss Supra 40 VP scanning electron microscope operated at 1−10 keV.

The average composition of the nanocrystals determined by energy-dispersive X-ray spectroscopy (EDS) analysis of 25 nanocrystals was $Cu_{2.08}Zn_{1.01}Sn_{1.20}S_{3.70}$. The nanocrystals are slightly tin-rich and sulfur-deficient. Scanning transmission electron microscopy (STEM)−EDS elemental mapping of a field of nanocrystals (Figure 2.15) confirmed that Cu, Zn, Sn, and S are evenly distributed among the nanocrystals and that there is no noticeable compositional distribution among the nanocrystals. XRD (Figure 2.13) matches kesterite CZTS. The band-gap energy determined from the absorbance spectrum of a nanocrytal dispersion (Figure 2.14 inset) is 1.3 eV, which is close to the bulk literature value of ~1.5 eV for CZTS.

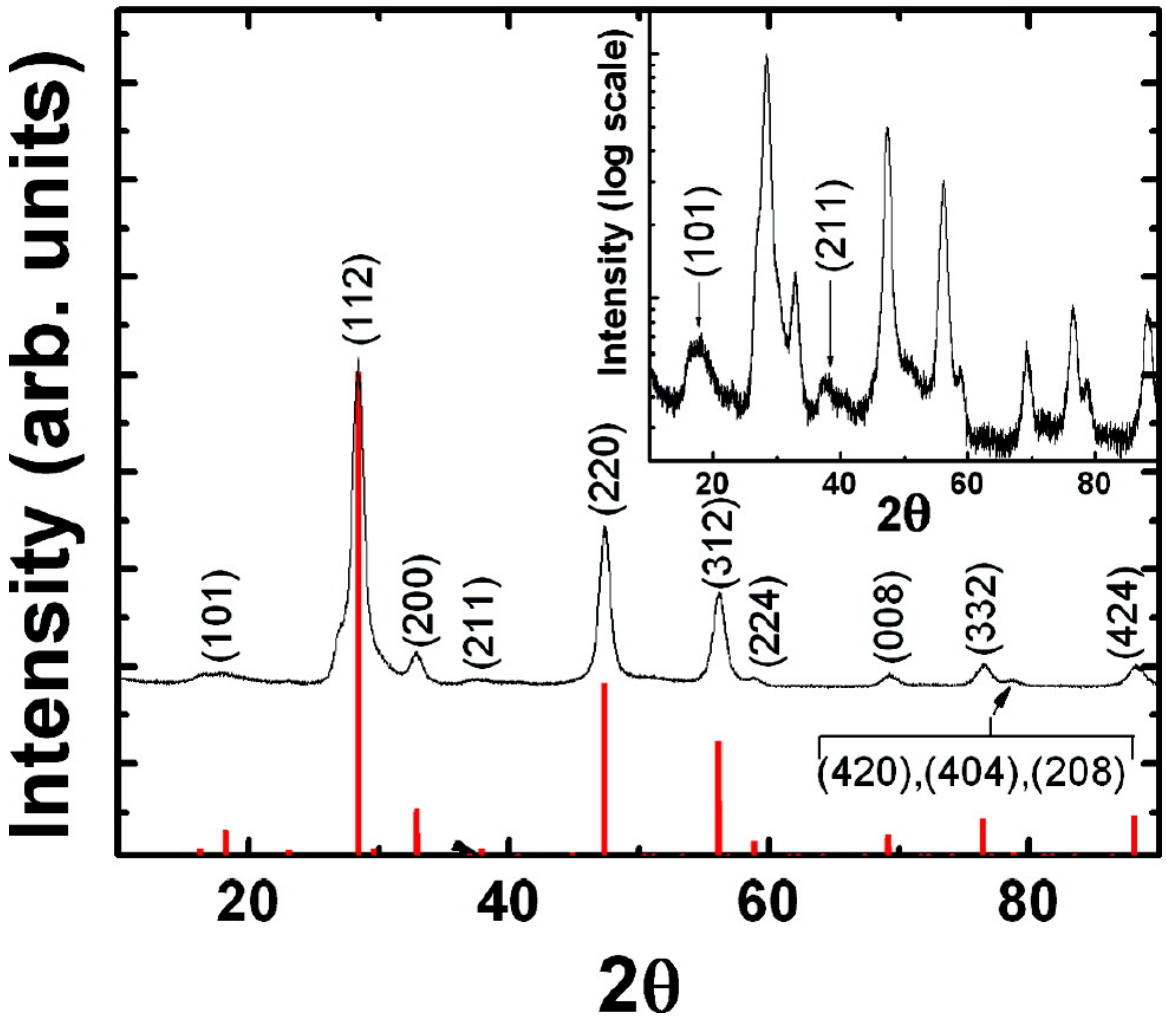

Figure 2.13. XRD pattern of CZTS nanocrystals [Cu Kα radiation (λ = 1.54 Å)]. The red reference pattern was simulated with CaRIne Crystallography 3.1 software using space group I4 and lattice parameters a = b = 5.427 Å and c = 10.848 Å for kesterite CZTS (JCPDS no. 26-0575). XRD data were acquired on a Bruker-Nonius D8 Advance powder diffractometer with samples on quartz substrates, scanning at 6 deg/min in 0.02° increments for ~12 h.

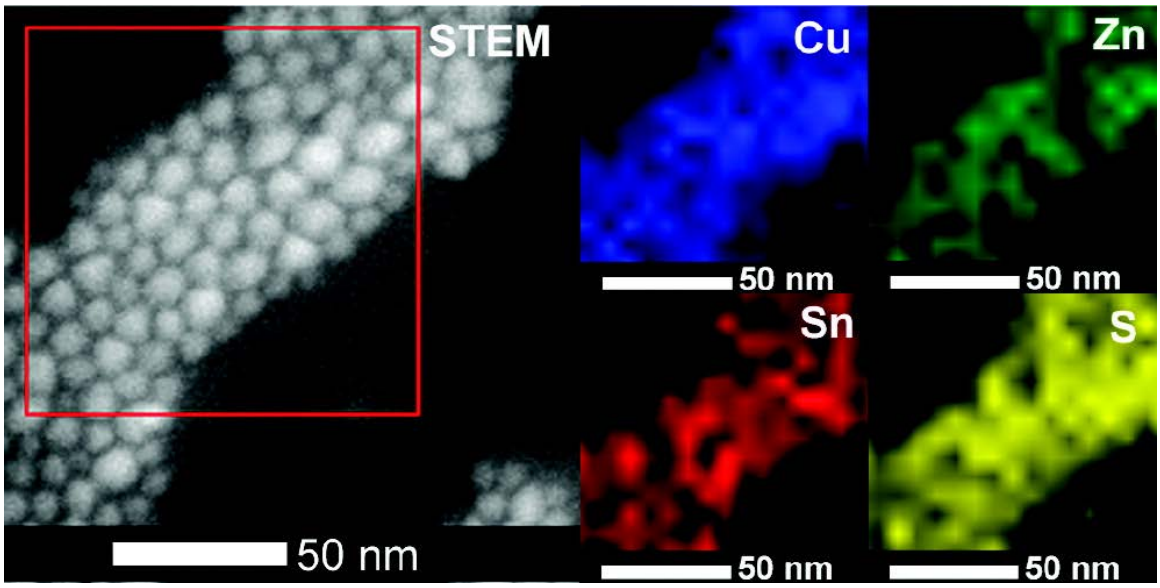

Figure 2.14. STEM−EDS elemental map of CZTS nanocrystals. The images were obtained on a Tecnai G2 F20 X-Twin microscope at an accelerating voltage of 200 kV.

2.3.4. Luminescent $CuInS_XSe_{2-X}$ (CISS) Nanocrystals

$CuInS_xSe_{2-x}$ nanocrystals were synthesized via arrested precipitation in a high boiling point solvent octadecene with dodecanethiol as both a capping ligand and sulfur source. Figure 2.16 shows TEM images of CISS nanocrystals synthesized with varying reaction times. The nanocrystals become larger with increasing reaction time. Starting at approximately 1 hour, the particles begin to become more polydisperse, as can be seen in Figure 2.16(d). Lattice spacing measurements from high resolution TEM are consistent

with a sphalerite or chalcopyrite crystal structure, with lattice spacings corresponding to CISS with a roughly 1:1 S:Se ratio.

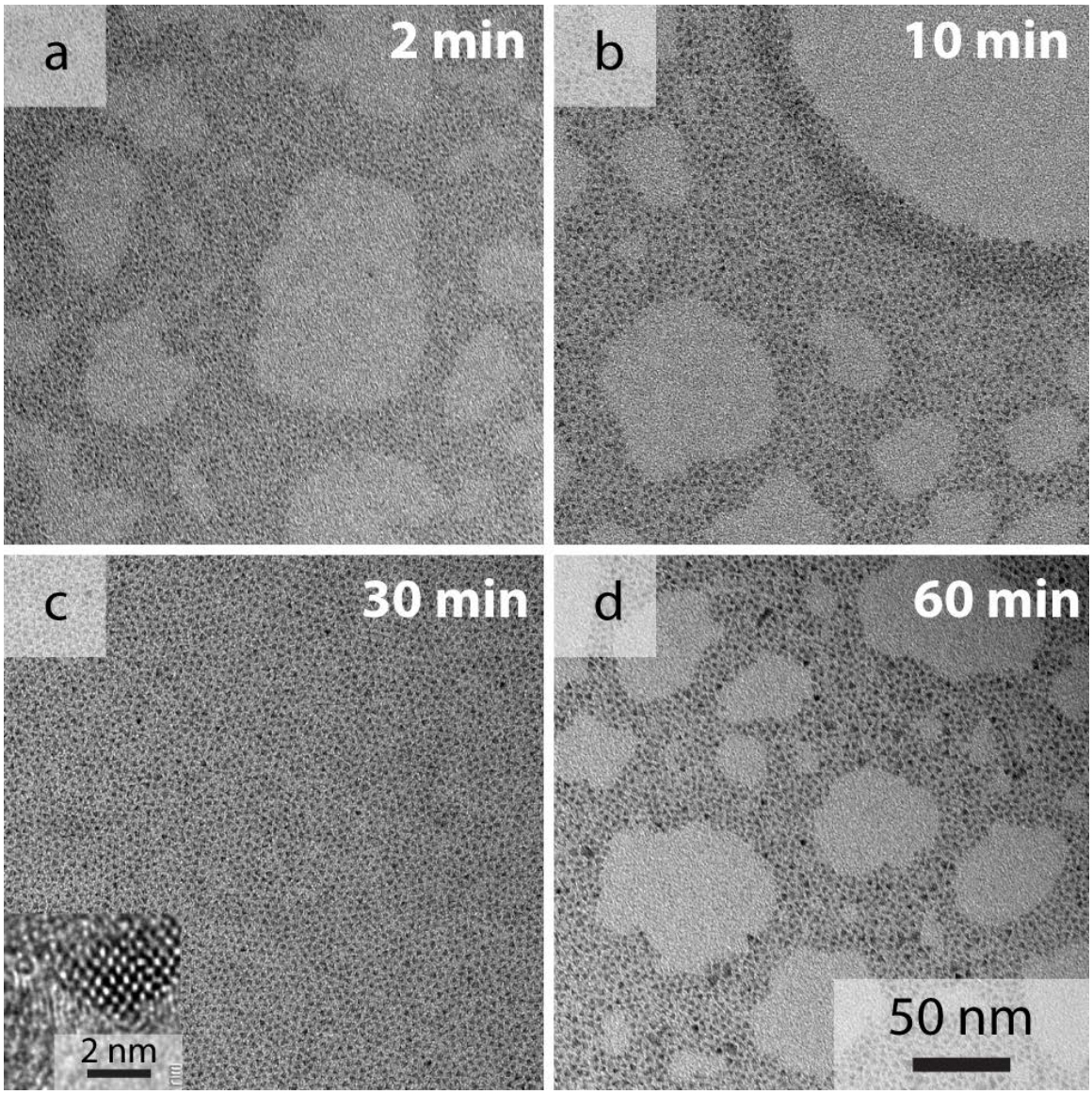

Figure 2.15. TEM of CISS nanocrystals at reaction with reaction times of (a) 2 min, (b)10 min, (c) 30 min, and (d) 1 hour. Inset: high resolution TEM of a single CISS nanocrystal

XRD (Figure 2.16) confirmed that the nanocrystals are either chalcopyrite or sphalerite CISS and that no other phases are produced in the reaction. The XRD spectra do not show peaks at ~17° and 35°, which correspond to the (101) and (211) lattice planes in the chalcopyrite crystal structure. These peaks are expected to have ~1% of the intensity compared to the (112) ((111) for sphalerite) peak, and therefore cannot be distinguished due to the noise. The (112) peak lies between where the (112) peaks for chalcopyrite copper indium selenide and copper indium sulfide would be (JCPDS #). This indicates that the nanocrystals are an alloy of the two. EDS from fields of nanocrystals gave an average Cu:In:S:Se composition of 1.0:1.0:1.3.0.7. There was no compositional variation from particle to particle within the error of the EDS detector. In addition, the composition was not significantly different for samples with different reaction times. However, when the growth temperature was reduced to 200°C or less, the nanocrystals became selenium rich, indicating lower reactivity of the dodecanethiol sulfur source, relative to the tributylphosphine selenide (TBP:Se). However, these particles had poor photoluminescence quantum yields compared to those synthesized using higher temperatures. Overcoating with a thin layer of ZnS resulted in an enhancement of PL quantum yield that was stable in air for several months.

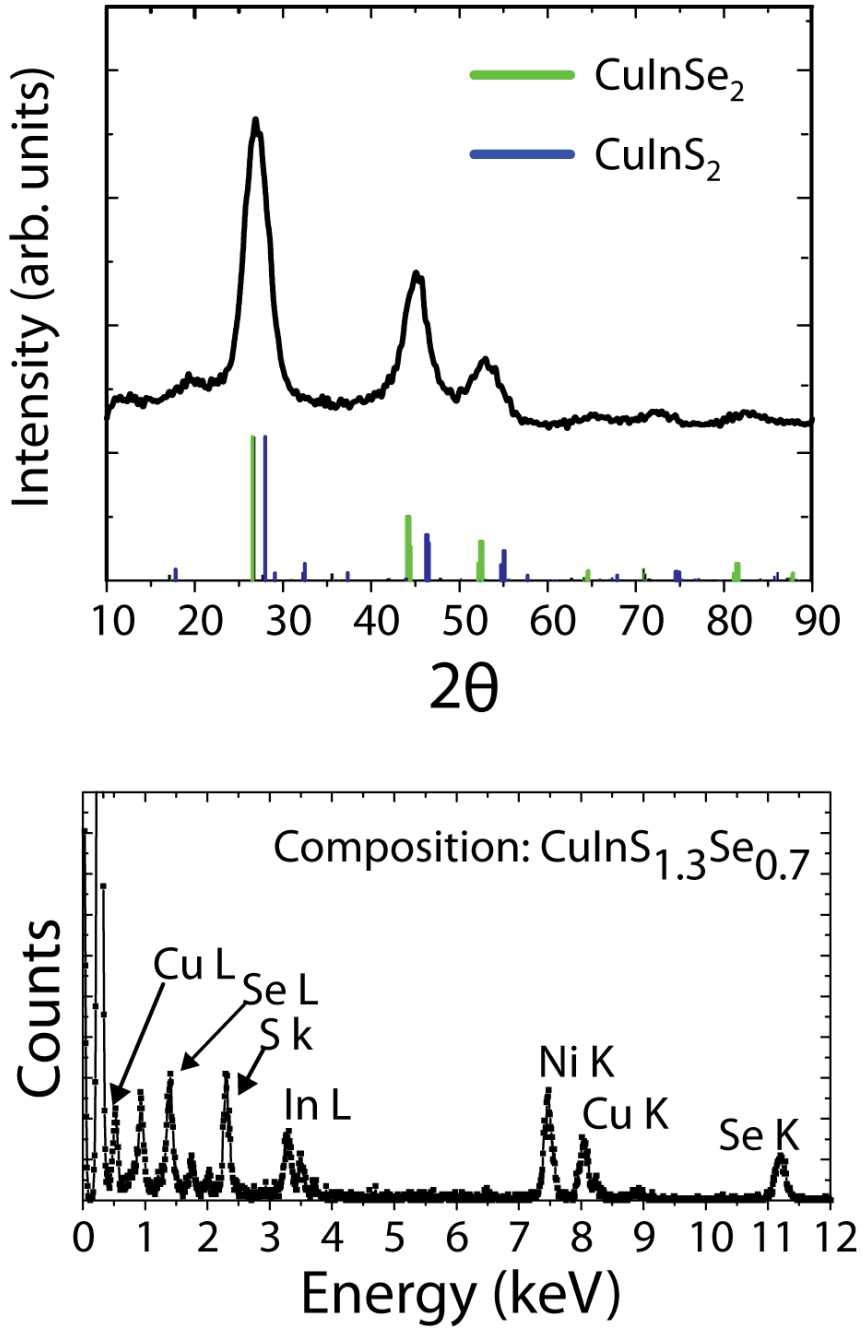

Figure 2.16. Powder XRD pattern (top) and EDS spectrum (bottom) of CISS nanocrystals.

Absorbance and PL measurements (Figure 2.17) show evidence of quantum confinement in the CISS nanocrystals. For the aliquot taken immediately after injection of the TBP:Se (0 min), there is an absorbance shoulder at approximately 380 nm. There is a weak and broad PL peak (QY < 0.01%), centered around 610 nm. As the reaction proceeds, the CISS nanocrystals grow, redshifting the absorbance and PL spectra. After 90 minutes, the absorbance shoulder shifts to ~650 nm, and the PL peak shifts to ~765 nm. Bulk CISS with the composition calculated by EDS would have band gap of about 1.2 eV (1,030 nm). This indicates that even after 90 minutes of growth time, the nanocrystals exhibit quantum confinement effects.

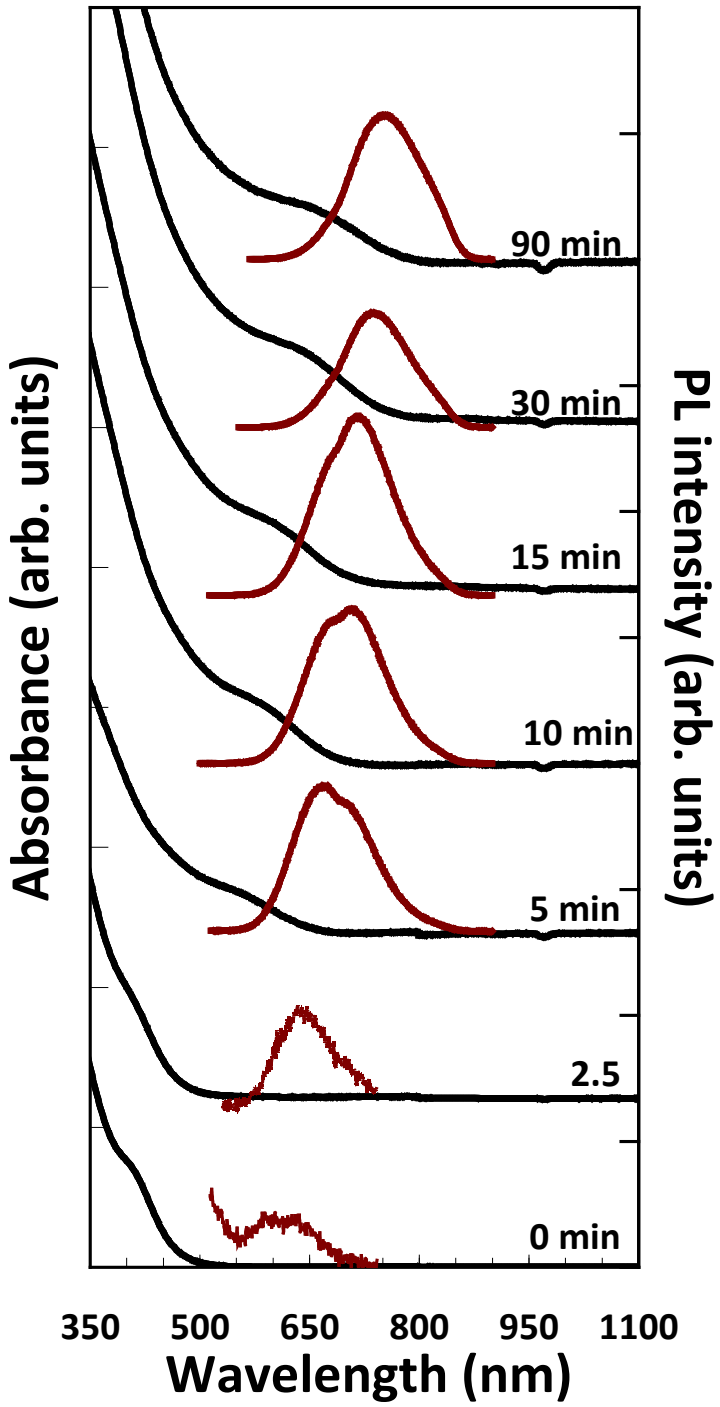

Figure 2.17. Absorbance and photoluminescence spectra of CISS nanocrystals.

2.4. CONCLUSIONS

Compound semiconductor nanocrystals are potentially useful for many electronic applications, like photovoltaics, light emitting diodes, thermoelectrics, and thin-film transistors. $CuInS_2$, $CuInSe_2$, CIGS, and CZTS nanocrystals were all synthesized using oleylamine as the solvent. By modifying the transition metal precursors and using dodecanethiol as both a ligand and sulfur source, quantum confined $CuInSe_{2-X}S_X$ nanocrystals were synthesized.

2.5. REFERENCES

1. Jackson, P.; Hariskos, D.; Lotter, E.; Paetel, S.; Wuerz, R.; Menner, R.; Wischmann, W.; Powalla, M. *Progress in Photovoltaics: Research and Applications* **2011,** 19, (7), 894-897.

2. Staebler, D.; Wronski, C. *Appl. Phys. Lett.* **1977,** 31, (4), 292.

3. Kumar, A. P.; Reddy, K. V. *Thin Solid Films* **1997,** 304, (1-2), 365-370.

4. Gur, I.; Fromer, N. A.; Geier, M. L.; Alivisatos, A. P. *Science* **2005,** 310, (5747), 462-5.

5. Wu, Y.; Wadia, C.; Ma, W.; Sadtler, B.; Alivisatos, A. P. *Nano Lett* **2008,** 8, (8), 2551-5.

6. Huynh, W. U.; Dittmer, J. J.; Alivisatos, A. P. *Science* **2002,** 295, (5564), 2425-7.

7. Murray, C. B.; Norris, D. J.; Bawendi, M. G. *Journal of the American Chemical Society* **1993,** 115, (19), 8706-8715.

8. Allen, P. M.; Walker, B. J.; Bawendi, M. G. *Angew Chem Int Ed Engl* **2010,** 49, (4), 760-2.

9. Pietryga, J. M.; Schaller, R. D.; Werder, D.; Stewart, M. H.; Klimov, V. I.; Hollingsworth, J. A. *J Am Chem Soc* **2004,** 126, (38), 11752-3.

10. Henderson, E. J.; Hessel, C. M.; Veinot, J. G. *J Am Chem Soc* **2008,** 130, (11), 3624-32.

11. Lee, D. C.; Pietryga, J. M.; Robel, I.; Werder, D. J.; Schaller, R. D.; Klimov, V. I. *J Am Chem Soc* **2009,** 131, (10), 3436-7.

12. Erogbogbo, F.; Liu, T.; Ramadurai, N.; Tuccarione, P.; Lai, L.; Swihart, M. T.; Prasad, P. N. *ACS nano* **2011**.

13. Allen, P. M.; Bawendi, M. G. *J Am Chem Soc* **2008,** 130, (29), 9240-1.

14. Ghezelbash, A.; Korgel, B. A. *Langmuir* **2005,** 21, (21), 9451-9456.

Chapter 3: $CuInSe_2$ Nanocrystal-based Photovoltaics‡

3.1. INTRODUCTION

Nanocrystals are being actively studied for use as light-absorbing materials in photovoltaic devices (PVs). PVs conveniently convert sunlight into electrical power, thus enabling the use of an abundant and sustainable energy source. At the moment, the PV market is dominated by crystalline and polycrystalline Si devices, even though the technology remains more expensive than conventional fossil fuel-based energy. Alternatives to Si include thin film direct band gap semiconductors that do not require the extreme purity of Si to achieve high efficiency. CdTe and $CuIn_XGa_{1-X}Se_2$ (CIGS) PVs have exhibited efficiencies of over 20% for CIGS[1] and 16.5% for CdTe.[2] CdTe PVs can now be manufactured for lower cost than crystalline Si devices, but they are still too expensive for grid parity.

Semiconductor nanocrystal inks can be deposited under ambient conditions on various substrates, including plastics, and could provide lower manufacturing cost than current technologies. Nanocrystals also enable alternative device structures that are not be possible using conventional high temperature processing technology. For example, nanocrystals can be embedded in polymers to take advantage of the light absorption properties of both materials, or implemented in photoelectrochemical cells like the dye-sensitized solar cell, as illustrated in Figure 3.1.

---

‡ Portions of this chapter appear in *Journal of the American Chemical Society* 130(49), 16770-16777 (**2011**), *Energy & Environmental Science* 3(10), 1600-1606 (**2010**), and *Optics Express*, 18(S3), A411-A420 (**2010**)

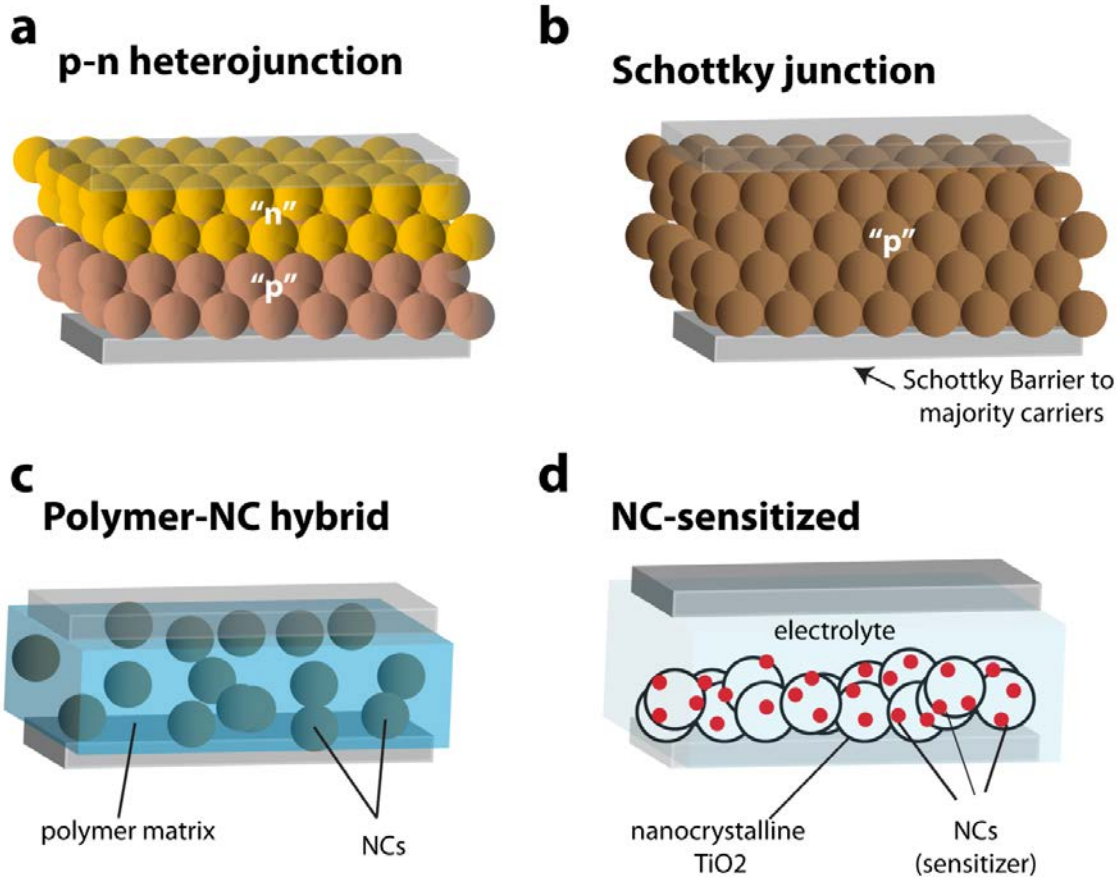

Figure 3.1. Various possible device structures using nanocrystals: (a) p-n heterojunction: (b) Schottky-barrier, (c) organic/nanocrystal hybrid, and (d) nanocrystal-sensitized cells.

3.2. Solar Cell Operation and Metrics

Figure 3.1 shows schematics of different nanocrystal-PV structures that have been studied. The power conversion efficiency (η) of the device is a measure of how much of the incident solar radiation is converted into electrical energy[3]:

$$\eta = \frac{P_{max}}{P_{in}} \quad (1)$$

P_{in} is the power of the light irradiated on the device and P_{max} is the maximum power output of the device. Typically, solar cells are tested with AM 1.5 spectral irradiation with 1 sun intensity, which has P_{in} =100 mW cm^{-1}. AM1.5 spectral irradiance (AM = airmass, 1.5= number of atmospheres refers to the solar spectrum at mid latitudes during mid-day, which is approximated by 5800K blackbody radiation passing through the Earth's atmosphere from a solar zenith angle of 48.2°.

There are fundamental limitations of the PCE. Photons with energy below the band gap of the semiconductor are not absorbed. When a photon with energy greater than the band gap is absorbed, there is an immediate relaxation of the photogenerated "hot" carrier to the bottom of the conduction band and any energy in the photon greater than the band gap energy is lost as heat. The Schockley-Quiesser (SQ) limit of 33% for a single junction solar cell results from the combination of these two losses.[4] For optimum performance of a single junction PV, the band gap of the semiconductor should be between 1.3 and 1.4 eV, otherwise the fundamental limit on the PCE is less than the SQ limit.

The PV device consists of two semiconductor materials interfaced in the light-absorbing region of the solar cell. Often, only one of the semiconductors is the primary light absorbing material, but another semiconductor is needed to create a pn junction (or Schottky barrier) to induce separation of the photogenerated electrons and holes. Illumination leads to a photogenerated current, which is called the short circuit current

density (J_{sc}) at zero bias. Under forward bias equal to the open circuit voltage (V_{oc}), there is no current in the device. V_{oc} is limited by the energy difference between bands and levels in junctions. The cell is operated in the fourth quadrant at the maximum power point, P_{max}, as illustrated in Figure 6c. The fill factor (FF), is a measure of how "square" the IV curve is when illuminated:

$$FF = \frac{P_{max}}{V_{oc} J_{sc}} \quad (2)$$

High series resistance in the device (*Rs*), and low shunt resistance (*Rp*) both degrade the fill factor. High shunt resistance occurs when the diode is leaky due to pinholes, cracks or other conductive pathways in the film. High series resistance results from poor conduction in the device layers and poor interfaces.

3.3. NANOCRYSTAL-BASED PHOTOVOLTAICS

Nanocrystals can be dispersed in solvents and deposited and processed much like organic materials. One of the first reported ncPV devices was made of a blended light-absorbing layer of polymer (poly~2-methoxy,5-2--ethyl-hexyloxy-*p*- phenylenevinylene) and pyridine-capped CdSe nanocrystals.[5] The power conversion efficiency was 0.6%, which was later improved to 1.7% by embedding CdSe nanorods in poly-3-hexylthiophene (P3HT).[6] Organics, however, are relatively unstable in air, especially under illumination at elevated temperature. The first all-inorganic ncPV was reported in 2006 with CdTe and CdS.[7] Nanocrystals were deposited from solution and sintered at 400^{o}C to achieve PCEs of up to 2.9%. Since then, many other ncPVs have been developed, including PbS,[8] PbSe,[9, 10] Cu_2S,[11] $CuInSe_2$[12, 13], and Cu_2ZnSnS_4.[14] The

highest ncPV device efficiency to date is about 6%.[15-17] Nanocrystal inks also provide a semiconductor material amenable to solar cells fabricated on mechanically flexible and light-weight plastic substrates. Flexible ncPVs of $CuInSe_2$ nanocrystals on gold-coated polyimide substrates[13] and Cu_2S nanocrystals on polyethylene terephthalate films[11] have been made.

Nanocrystal-based PVs may offer access materials that are difficult to make as bulk thin films. For example, $Cu(In,Ga)Se_2$ (CIGS) thin films are made by annealing under selenium vapor at high temperatures of over 450^{o}C to obtain the desired chalcopyrite CIGS material.[18] Chalcopyrite CIGS nanocrystals on the other hand can be synthesized directly using colloidal methods with the desired composition and phase, dispersed in a solvent as an ink, and then simply coated onto a substrate for device fabrication.[12] One of the goals of ncPV research is to obtain high efficiencies with low temperature device processing; however, substantially higher device efficiencies nearing 10% have been achieved by sintering nanocrystal films as a result of improved transport.[19-23] Similar approaches have produced nearly 7% CdTe solar cells.[24] Table 1 summarizes ncPV performance achieved to date.

Table 3.1. Reported efficiencies of ncPV devices using various materials, device geometries and processing conditions.

Nanocrystal Material	Device Geometry	η (%)	Jsc (mA/cm^2)	Voc (mV)	FF	Processing T (°C)/ atmosphere	Ref.
Colloidal Nanocrystals							
$CuInSe_2$	Au/**$CuInSe_2$**/CdS/ZnO/ITO	3.1	16.3	410	0.46	RT/air	13
$CuInSe_2$	Mo/**$CuInSe_2$**/CdS/ZnO/ITO	0.24	3.2	300	0.25	RT/air	12
CZTS	Au/**CZTS**/CdS/ZnO/ITO	0.23	1.95	320	0.37	RT/air	14
CdSe & CdTe	Ca/**CdTe**/**CdSe**/ITO	2.9	13.2	450	0.49	400/air	7
Cu_2S-CdS	Al/**CdS**/**Cu_2S**/ITO	1.6	5.63	600	0.47	150/unk	11
PbS & TiO_2	SnO_2:F/**TiO_2**/**PbS**/Au/Al	5.1	16.2	510	0.58	RT/air	16
PbS &TiO2	SnO_2:F/**TiO_2**/**PbS**/Au/Al	5.5	20.6	480	0.56	RT/air	17
PbS & TiO2	SnO_2:F/**TiO_2**/**PbS**/Au/Al	6.0	20.2	480	0.62	RT/air	15
Nanocrystal Absorbers as a precursor for high temperature sintered films							
$CuInSe_2$	Mo/**$CuInSe_2$**/CdS/ZnO/ITO	2.8	25.8	280	0.39	500/ Se	23
CIGSSe	Mo/**CIGSSe**/CdS/ZnO/ITO	5.5	23.7	460	0.51	500/Se	22
CZTS	Mo/**CZTS**/CdS/ZnO/ITO	0.8	11.5	210	0.33	500/Se	21
CZTSSe	Mo/**CZTSSe**/CdS/ZnO/ITO	7.2	31.2	430	0.54	500/Se	20
CZTGeSSe	Mo/**CZTGeSSe**/CdS/ZnO/ITO	6.8	21.5	640	0.49	500/Se	19
CdTe	ITO/**CdTe**/ZnO/Al	6.9	20.7	590	0.56	350/air	24

3.4. EXPERIMENTAL

3.4.1. Fabrication of $CuInSe_2$ Nanocrystal-based Solar Cells

Prototype utilizing $CuInSe_2$ nanocrystals were first fabricated using a dropcast film of nanocrystals dispersed in tetrachloroethane onto a patterned molybdenum coated glass substrate.

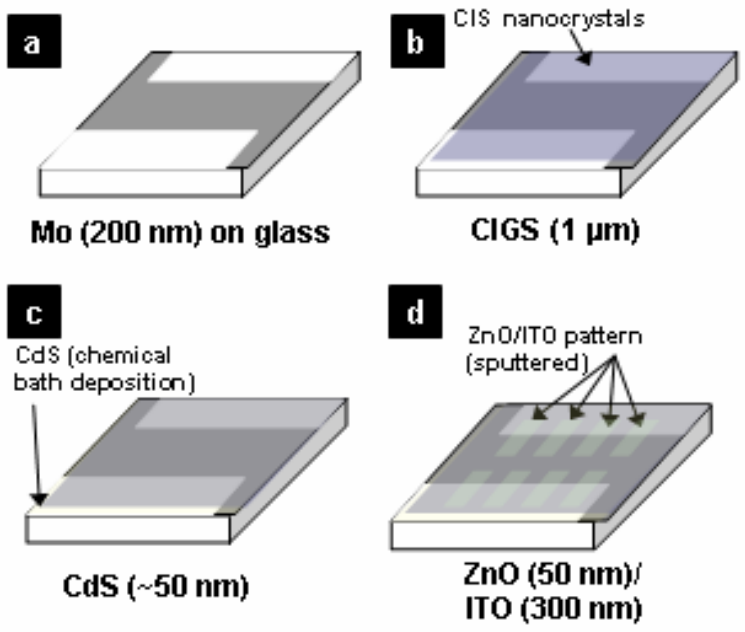

Figure 3.2. Fabrication of PV device structure, proceeding from (a) Mo deposition on soda lime glass, (b) $CuInSe_2$ nanocrystal ink deposition, (c) CdS chemical bath deposition and (d) ZnO/ITO deposition. Eight devices are fabricated on each substrate and tested.

3.4.2. Nanocrystal Film Deposition and Photovoltaic Device Fabrication

Thick films (~1 µm) of nanocrystals were deposited onto 12 × 25 mm glass or Mo-coated glass substrates by dropping 150 µL of TCE dispersions with nanocrystal concentrations of 5 mg/mL. The film was fully dried by placing the substrate in a vacuum chamber at room temperature for 12 h.

Photovoltaic test structures were fabricated with a conventional sandwich-type Mo/$CuInSe_2$/CdS/ZnO/indium tin oxide (ITO) configuration. The molybdenum (Mo) back contact was first deposited on soda lime glass (Delta Technologies, 25 × 25 × 1.1 mm polished float glass) by radio frequency (rf) sputtering from a pure Mo target

(99.999%, Lesker) in ultrapure Ar (99.999%, Praxair) at 5 mTorr. Radio frequency sputtering was used instead of DC sputtering because it has been reported to provide a film with a better combination of substrate adhesion and good conductivity.(35) The $CuInSe_2$ nanocrystal layer was deposited by drop casting it from TCE dispersions and then placing the film under vacuum overnight at room temperature to dry.

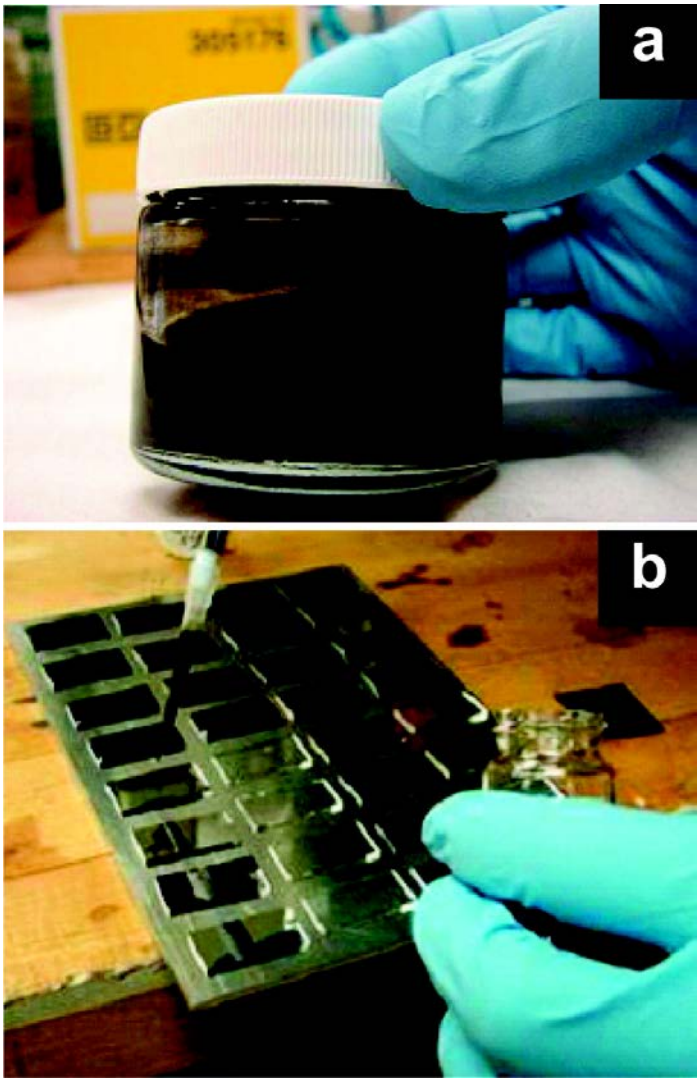

Figure 3.3. Photograph of (a) a CuInSe2 nanocrystal dispersion and (b) the deposition of thin films on an array of glass substrates. After depositing the films, the substrates were placed in a vacuum oven at room temperature for 12 h.

A CdS buffer layer was deposited from solution using a procedure and parameters outlined by McCandless and Shafarman.[25] Stock aqueous solutions of 0.015 M cadmium sulfate (Aldrich, 99.999%), 1.5 M thiourea (Fluka, 99%), and 14.28 M ammonium

hydroxide (Fisher Scientific, Certified ACS) were made and used in preparation of working solutions by mixing 1.25 mL of the $CdSO_4$ solution, 2.2 mL of the $CS(NH_2)_2$ solution, and 2.8 mL of the NH_4OH solution. Substrates were placed on a hot plate for 10 min that had been preheated to 90 °C, after which 0.5 mL of the working solution was deposited on each substrate. The substrates were immediately covered to reduce the loss of ammonia from the solution. After 2 min the substrates were removed from the hot plate, rinsed with DI water, and laid flat to dry. The i-ZnO/ITO top contact was deposited by rf sputtering from pure targets of each material: ZnO (99.9%, Lesker) was deposited using 0.5% O2 in Ar (99.95%, Praxair) and ITO (99.99% In2O3:SnO2 90:10, Lesker) was deposited in Ar. The final active region of the device was 8 mm2 (a 4 mm × 2 mm rectangle).

3.4.3. Device Testing

The electrical properties of the PV devices were characterized using a Karl Suss Probe station and an Agilent 4156C Parameter Analyzer. Detailed studies of power conversion efficiencies were done using a Keithley 2400 General Purpose Sourcemeter and a Xenon Lamp Solar Simulator (Newport) equipped with an AM1.5 filter. Incident photon conversion efficiency (IPCE) spectra were gathered using a lock-in amplifier (Stanford Research Systems, model SR830), a monochromator (Newport Cornerstone 260 1/4M), and a Si photodiode calibrated by the manufacturer (Hamamatsu).

3.5. RESULTS AND DISCUSSION

3.5.1. Drop-cast devices on Mo-coated glass

The current−voltage characteristics and the incident photon conversion efficiency (IPCE) of a typical PV device made with $CuInSe_2$ nanocrystals are shown in Figure 14. The measured power conversion efficiencies (η) of 32 devices ranged between 0.01 and 0.24%. The IPCE matches approximately the absorbance spectra of the $CuInSe_2$ nanocrystals (Figure 14b), confirming that the device response results from the nanocrystals. The relatively high IPCE of 22% for wavelengths between 400 and 500 nm tails off at higher wavelengths. The long-wavelength IPCE cutoff at 1050 nm corresponds approximately to the optical gap of the $CuInSe_2$ nanocrystals as it should, and the sharp drop in IPCE at wavelengths <400 nm is the result of ZnO light absorption. The ZnO layer is essentially serving as a photon cutoff filter in the device.

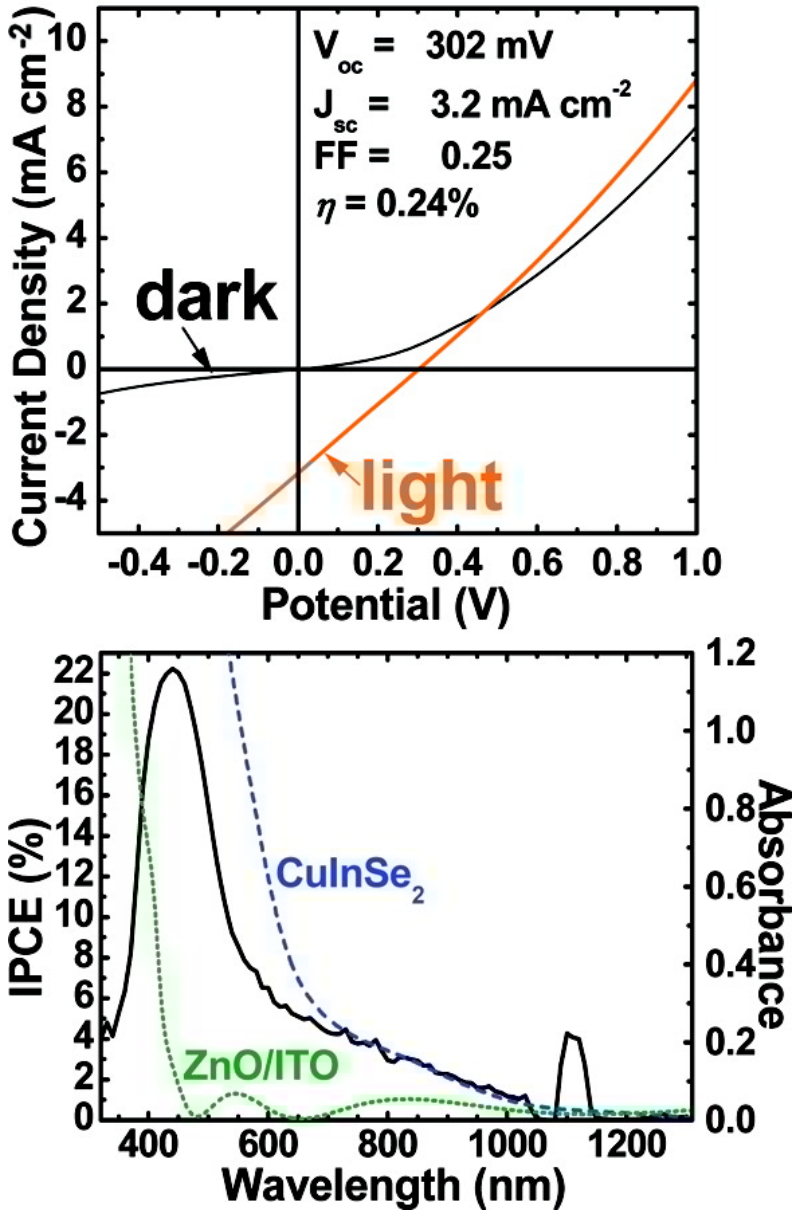

Figure 3.4. (a) Current−voltage characteristics and (b) IPCE spectra of a $CuInSe_2$ nanocrystal photovoltaic device (solid line) with absorbance curves of $CuInSe_2$ and ITO/ZnO layers (dashed). The IPCE spectrum was measured at zero bias. The nanocrystal absorber layer was 700 nm thick, consisting of oleylamine-capped $CuInSe_2$ nanocrystals with an average diameter of 15 nm.

The photovoltaic response of devices made from $CuInSe_2$ nanocrystal layers was reproducible and demonstrated that these nanocrystals have potential as light absorbing materials in PVs. However, the PV efficiencies in these particular devices are relatively low and require significant improvement for practical applications. Device efficiencies might be improved increasing the $CuInSe_2$ film thickness to absorb more photons, and the device structures themselves are relatively complicated with many factors that can decrease efficiency. The open circuit voltages (Voc) of the $CuInSe_2$ nanocrystal devices were actually quite reasonable, typically near 300 mV, which is getting close to the high-efficiency vapor-deposited $CuInSe_2$ devices (typical Voc values are 400 mV). The short circuit current densities (Jsc) and fill factors (FF), however, were quite low, with typical Jsc values of 3 mA cm^{-2} (compared to Jsc of 35 mA cm^{-2} for the highest efficiency (19%) vapor-deposited CIGS device) and FFs close to 0.25. The diode response was also relatively poor (see Appendix for data and analysis), with an ideality factor (A) much larger than 1, revealing that the device has high series and low shunt resistances. The high series resistance is partly attributed to high ITO sheet resistances (>300 Ω/□) and relatively resistive nanocrystal films. Four-point probe measurements gave resistivities of approximately 1 kΩ·cm, which are about 3 orders of magnitude more resistive than conventional CIGS films with good photovoltaic efficiencies. High shunt conductance (or low shunt resistance) in the devices can result from many factors, including holes or cracks in the nanocrystal film and penetration of the CdS or sputtered ZnO layers to the back contact.

3.5.2. PV devices fabricated by spray-deposition of CIS nanocrystals

Since the absorber layers are not processed at high temperature, alternative substrates and contacts can be used, including transparent conductive ITO or mechanically flexible plastic. Fig. 3 shows photographs of different kinds of PV devices that could be prepared by spray-depositing CIS nanocrystal absorber layers. IS nanocrystal layers were spray-coated with an airbrush (Iwata Eclipse HP-CS) operated at 50 psig of back pressure. The devices generally consist of a sandwiched construction of the p-type light-absorbing nanocrystal layer interfaced with an n-type semiconductor (CdS, ZnO) positioned between two planar conducting contacts. The thin CdS layer (5–10 nm) also helps protect the CIS nanocrystal layer during sputtering of the top layers.

Figure 3.5. Photograph of oleylamine-capped CIS nanocrystals in toluene being sprayed onto a substrate. (courtesy Austin American Statesman).

3.5.2.1. Au back contact

Conventional vapor-deposited CIGS PVs are fabricated on soda lime glass substrates with Mo back contacts because it can withstand the high selenization/annealing temperatures used to process the CIGS layer. The work function of Mo, however, is a poor choice for devices, as it creates a Schottky barrier with the CIS layer. During high temperature annealing, an interfacial $MoSe_2$ layer is created that provides ohmic contact to the CIGS layer, so this is not a problem. However, without annealing, the Schottky barrier between Mo and CIS significantly limits device performance.

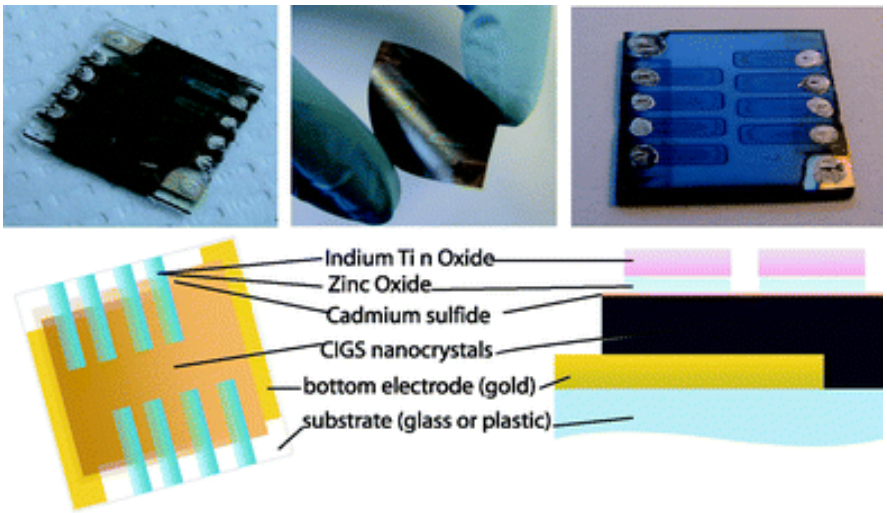

Figure 3.6. (top) photographs of spray coated devices on glass (left and right) and kapton (middle) substrates. (bottom) Schematic of Device structure.

Gold (Au) has a higher work function than Mo and should make a better back contact metal for the p-type CIS nanocrystal layer. Au is not used in conventional CIGS PVs because it cannot withstand the high-temperature annealing conditions. We have

found that CIS nanocrystal PVs made with Au contacts on glass outperform those made with Mo contacts. Au contacts are also easy to deposit on plastic substrates for flexible devices. Fig. 4 shows device characteristics of PV devices made from spray-deposited CIS nanocrystal layers on Au contacts on (4a) glass and (4b) plastic substrates. Optimized devices using this method had power conversion efficiencies as high as 3.1%.

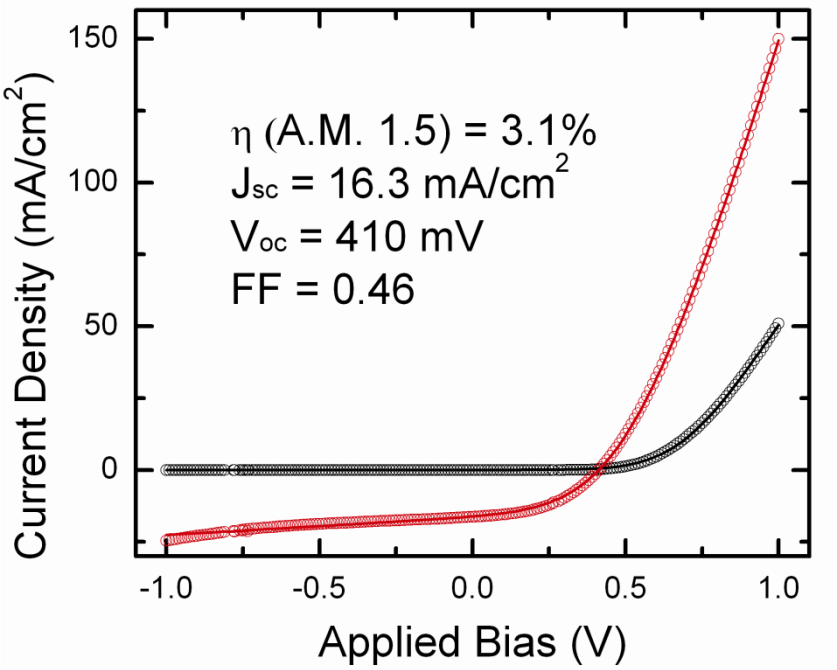

Figure 3.7. I-V characteristics of a device with power conversion efficiency of 3.1% under AM1.5 illumination. Dark conditions (black) and under AM1.5 irradiation (red). The device parameters are obtained by a best fit of Eqn (1) (solid lines) to the data (○).

3.5.3. Thickness limitations

Device efficiencies of 3% are too low for commercialization and need to be improved. The highest efficiency devices are actually composed of relatively thin nanocrystal layers that are only about 150 nm thick. We have found that increasing the nanocrystal layer thickness enhances light absorption but it does not improve device efficiency. Figure 4 shows I-V characteristics of devices made with nanocrystal films of increasing thickness. Jsc actually decreased when the nanocrystal films were made thicker, even though more electrons and holes are being photogenerated. This indicates that the photogenerated carriers cannot be extracted from the nanocrystal layer unless they are relatively close to the junctions.

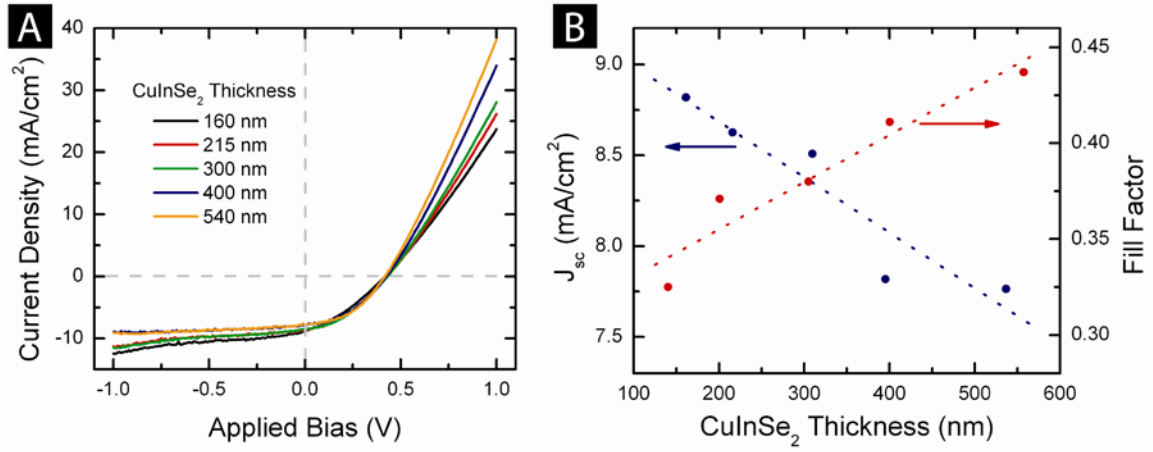

Figure 3.8. (A) I-V measurements of devices with varying thickness of spray deposited $CuInSe_2$ nanocrystal film and (B) calculated device parameters associated with these devices.

Measurements of the incident photon-to-electron conversion efficiency (IPCE) provide additional insight into how well the devices are performing and what the limiting factors are. In IPCE measurements, the short circuit current is measured as a function of the wavelength of the incident illumination. Figure 5A shows IPCE measurements for devices with varying nanocrystal layer thickness. The IPCE data is essentially an external quantum efficiency (at zero bias) that does not account for how much light is absorbed by the device—it is a measure of charge carriers extracted based on the number of photons that are illuminating the device. Another useful quantity is the internal quantum efficiency, which provides an accounting of the photon absorption and tells what fraction of the photogenerated carriers are actually extracted from the device.

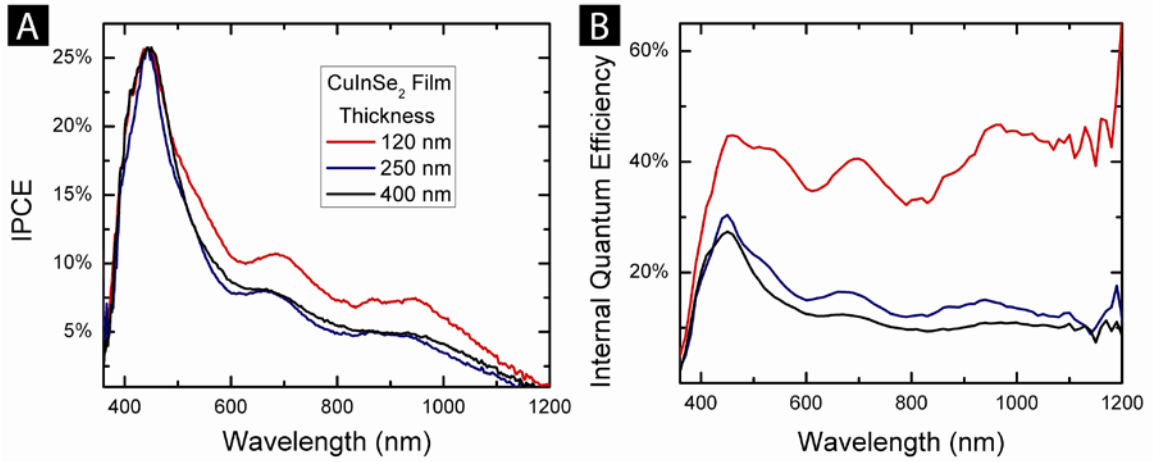

Figure 3.9. (A) IPCE measurements of a set of devices with different thicknesses of the $CuInSe_2$ nanocrystal film thickness shows similar trend between the different thicknesses. (B) Internal quantum efficiency data of the same devices reveals how thinner devices extract photogenerated carriers at a better efficiency.

The internal quantum efficiency of the devices, *IQE(λ)*, is the ratio of the wavelength-dependent IPCE, *IPCE(λ)*, to the fraction of the incident light at that wavelength that is absorbed by the $CuInSe_2$ nanocrystal films, *f(λ)*. *f(λ)* is determined from the transmittance of the top window layer, $T_{top}(\lambda)$; the transmittance of the $CuInSe_2$ nanocrystals layer, $T_1(\lambda)$; and the reflectivity of the back contact, $R_{BC}(\lambda)$.

$$f(\lambda) \approx T_{top}(\lambda)\left[1 - T_1(\lambda)^2 R_{BC}(\lambda)\right] \quad (2)$$

It should be noted that this estimate of the *IQE(λ)* does not account for internal reflection or optical interference effects that may also contribute to *f(λ)* and represents an upper bound. Figure 5B shows the device *IQE(λ)* for devices with different nanocrystal layer thickness. Consistent with the reduced Jsc for devices with thicker nanocrystal films, the thinner devices have much higher IQE, indicating that they are much better at extracting photogenerated carriers, across a wide range of wavelength, than the thicker devices.

The higher IQE and more efficient device performance of the thinner devices is also enhanced by light reflection from the back contact. Especially, the thinner films benefit from a "second pass" of light reflected off the back contact. This is evident in the IPCE measurements at longer wavelengths (600 nm to 1200 nm) where only a very small fraction of the incident light is absorbed by the thinner layers on the first pass. As the films get thicker, a large fraction of the incident photons are absorbed deeper in the nanocrystals layer and the resulting photogenerated carriers are unable to be efficiently

extracted. This data also indicates that the photogenerated carriers can only be extracted efficiently when they are generated close to the $CuInSe_2$/CdS/ZnO heterojunction.

3.5.4. Estimate of Depletion Region

The thickness of the active region in the nanocrystal layer in the device was determined by measuring the impedance of the devices. Figure 6C shows typical impedance data on a $CuInSe_2$ nanocrystal PV device with slightly modified structure. The device geometry (shown in Figure 6A) was devised to ensure that carrier depletion was limited to the spray deposited $CuInSe_2$ film. Circuit model shown in Figure 6B provides the best fit to the impedance data gathered from the diode. The capacitance of the space charge region C_{sc}, was extracted to determine the majority carrier density and an effective depletion width in the nanocrystal layer using a Mott-Schottky analysis. C_{sc} is related to the doping level N_A, and applied voltage V:

$$\frac{1}{C_{sc}^{\ 2}} = \left(\frac{2}{qN_A \varepsilon_s \varepsilon_0 A^2} \right) \left(V - V_{bi} - \frac{kT}{q} \right) \tag{3}$$

In Eqn (3), V_{bi} is the built-in voltage of the junction, q is the elementary charge of an electron, ε_0 is the vacuum permittivity and ε_s is the relative permittivity of bulk $CuInSe_2$ (≈ 10). Using the bulk permittivity is likely an overestimate. An overestimate in the permittivity would yield an underestimate underestimate in N_A and an overestimate in x_p. 2D shows C_{sc}^{-2} plotted against V. Values of N_A and V_{bi} were determined by fitting Eqn (3) to the data. The depletion layer width can be estimated from the relation:

$$V_{bi} = \frac{q}{2\varepsilon_s \varepsilon_0} \left[N_A x_p^{\ 2} + N_D x_n^{\ 2} \right] \tag{4}$$

N_A and N_D are acceptor and donor concentrations in the p-type and n-type layers, respectively, and x_p and x_n are the depletion layer widths of the p-type and n-type layers, respectively. With the device design shown in Figure 6A, depletion occurs only in the p-type nanocrystal layer, and Eqn (4) simplifies to

$$x_p^2 = \frac{qN_A V_{bi}}{2\varepsilon_s \varepsilon_0} \tag{5}$$

In a typical device the depletion region thickness was found to be 55 nm in the dark. When the device was illuminated, the depletion region thickness was found to decrease to 45 nm (under AM1.5 illumination). The change in doping level in the CdS layer under light leads to a noticeable change in the device properties, as discussed above. Further work is underway to gain a more detailed understand about the band alignment between layers in the nanocrystal devices.

3.6. CONCLUSIONS

Films of $CuInSe_2$ nanocrystals used as the absorber layer in conventional layered Mo/$CuInSe_2$/CdS/ZnO/ITO PV devices gave reproducible photovoltaic responses with power conversion efficiencies up to 0.2% and IPCE as high as 22% for photons with 400−500 nm wavelength. These devices provide a baseline performance and demonstrate as a proof-of-concept that these nanocrystals can be used in PVs. Practical devices, however, require higher efficiencies. There are many ways to try to improve PV efficiency, including using nanocrystals with shorter chain capping ligands, incorporating Ga into the films, and using various chemical or thermal treatments of the nanocrystal layers to increase their conductivity. New device architectures that are more suitable to

using nanocrystal absorber layers and low-temperature manufacturing steps may also provide ways to increase device efficiency and eliminate the need for high temperature processing. These are all topics for further study.

Power conversion efficiencies above 3% under AM1.5 are demonstrated for ambient processed $CuInSe_2$ nanocrystal-based PVs using Au as the back contact. The extraction of photogenerated carriers from deep within the $CuInSe_2$ nanocrystal film remains a major challenge. The high concentration of crystal interfaces leads to high recombination. A Mott-Schottky analysis of the space-charge capacitance in the device revealed that the active region of the device is only about 50 nm thick, which is consistent with IPCE and IQE measurements on devices with varying nanocrystal film thickness. Future efforts must focus on increasing the thickness of the space charge region to extract carriers deeper in the nanocrystal layer in order to improve device efficiency.

3.7. REFERENCES

1. Jackson, P.; Hariskos, D.; Lotter, E.; Paetel, S.; Wuerz, R.; Menner, R.; Wischmann, W.; Powalla, M. *Progress in Photovoltaics: Research and Applications* **2011,** 19, (7), 894-897.

2. Xuanzhi, W. *Solar Energy* **2004,** 77, (6), 803-814.

3. Nelson, J., *The Physics of Solar Cells*. Imperial College Press: 2003.

4. Shockley, W.; Queisser, H. J. *Journal of Applied Physics* **1961,** 32, (3), 510 - 519.

5. Greenham, N. C.; Peng, X.; Alivisatos, A. P. *Physical review. B, Condensed matter* **1996,** 54, (24), 17628-17637.

6. Huynh, W. U.; Dittmer, J. J.; Alivisatos, A. P. *Science* **2002,** 295, (5564), 2425-7.

7. Gur, I.; Fromer, N. A.; Geier, M. L.; Alivisatos, A. P. *Science* **2005,** 310, (5747), 462-5.

8. McDonald, S. A.; Konstantatos, G.; Zhang, S.; Cyr, P. W.; Klem, E. J.; Levina, L.; Sargent, E. H. *Nature materials* **2005,** 4, (2), 138-42.

9. Koleilat, G. I.; Levina, L.; Shukla, H.; Myrskog, S. H.; Hinds, S.; Pattantyus-Abraham, A. G.; Sargent, E. H. *ACS nano* **2008,** 2, (5), 833-40.

10. Luther, J. M.; Law, M.; Song, Q.; Perkins, C. L.; Beard, M. C.; Nozik, A. J. *ACS nano* **2008,** 2, (2), 271-80.

11. Wu, Y.; Wadia, C.; Ma, W.; Sadtler, B.; Alivisatos, A. P. *Nano Lett* **2008,** 8, (8), 2551-5.

12. Panthani, M. G.; Akhavan, V.; Goodfellow, B.; Schmidtke, J. P.; Dunn, L.; Dodabalapur, A.; Barbara, P. F.; Korgel, B. A. *J Am Chem Soc* **2008,** 130, (49), 16770-7.

13. Akhavan, V. A.; Panthani, M. G.; Goodfellow, B. W.; Reid, D. K.; Korgel, B. A. *Optics express* **2010,** 18 Suppl 3, A411-20.

14. Steinhagen, C.; Panthani, M. G.; Akhavan, V.; Goodfellow, B.; Koo, B.; Korgel, B. A. *Journal of the American Chemical Society* **2009,** 131, (35), 12554-5.

15. Tang, J.; Kemp, K. W.; Hoogland, S.; Jeong, K. S.; Liu, H.; Levina, L.; Furukawa, M.; Wang, X.; Debnath, R.; Cha, D.; Chou, K. W.; Fischer, A.; Amassian, A.; Asbury, J. B.; Sargent, E. H. *Nature materials* **2011,** 10, (10), 765-771.

16. Barkhouse, D. A.; Debnath, R.; Kramer, I. J.; Zhitomirsky, D.; Pattantyus-Abraham, A. G.; Levina, L.; Etgar, L.; Gratzel, M.; Sargent, E. H. *Adv Mater* **2011,** 23, (28), 3134-8.

17. Pattantyus-Abraham, A. G.; Kramer, I. J.; Barkhouse, A. R.; Wang, X.; Konstantatos, G.; Debnath, R.; Levina, L.; Raabe, I.; Nazeeruddin, M. K.; Gratzel, M.; Sargent, E. H. *ACS nano* **2010,** 4, (6), 3374-80.

18. Bar, M.; Repins, I.; Contreras, M. A.; Weinhardt, L.; Noufi, R.; Heske, C. *Appl Phys Lett* **2009,** 95, (5), 3.

19. Ford, G. M.; Guo, Q.; Agrawal, R.; Hillhouse, H. W. *Chemistry of Materials* **2011,** 23, (10), 2626-2629.

20. Guo, Q.; Ford, G. M.; Yang, W.-C.; Walker, B. C.; Stach, E. A.; Hillhouse, H. W.; Agrawal, R. *Journal of the American Chemical Society* **2010,** 132, (49), 17384-17386.

21. Guo, Q.; Ford, G. M.; Hillhouse, H. W.; Agrawal, R. *Nano Letters* **2009,** 9, (8), 3060-3065.

22. Guo, Q.; Hillhouse, H. W.; Agrawal, R. *Journal of the American Chemical Society* **2009,** 131, (33), 11672-11673.

23. Guo, Q.; Kim, S. J.; Kar, M.; Shafarman, W. N.; Birkmire, R. W.; Stach, E. A.; Agrawal, R.; Hillhouse, H. W. *Nano Letters* **2008,** 8, (9), 2982-2987.

24. Jasieniak, J.; MacDonald, B. I.; Watkins, S. E.; Mulvaney, P. *Nano Letters* **2011,** 11, (7), 2856-2864.

25. McCandless, B. E.; Shafarman, W. N. Chemical Surface Depostion of Ultra-Thin Semiconductors. 6,537,845, 2003.

Chapter 4: Thermal and Chemical Processing of Nanocrystal films for Photovoltaics

4.1. INTRODUCTION

The ligands bound to colloidal nanocrystal are essential for controlled synthesis, as well as chemically and electronically passivating the nanocrystal surfaces.[1] For many electronic applications, these bulky and insulating organic ligands are undesirable because they are poor electrical conductors.[2] For practical thin film photovoltaic devices, films need to be at least ~1 micrometer in thickness to absorb the incoming light.[3] In conventional crystalline inorganic photovoltaics, grain sizes are often this size, and carrier transport between grains is rarely a dominant mechanism. A major disadvantage of using colloidal nanocrystals in PVs is that carriers need to hop between several nanocrystals to travel from their generation location to the collection electrodes.[4] In this chapter we evaluate various methods of removing or replacing organic ligands to achieve increases in film conductivity.

Numerous approaches to improving charge transport in nanocrystal films have been explored. Replacing bulky ligands with conjugated like pyridine in a post-deposition ligand exchange has shown some promise.[5, 6] Post-deposition exchange with small molecules like ethanedithiol and hydrazine have resulted in carrier mobilities as high as ~0.1 $cm^2 V^{-1} s^{-1}$.[7] Exchange with hydrazine-based metal chalcogenide ligands has yielded films with mobilities of up to 16 $cm^2 V^{-1} s^{-1}$.[8]

4.2. NANOCRYSTAL FILM DEPOSITION

4.2.1. Drop Casting

Nanocrystal films were deposited from either drop casting from a concentrated dispersion of nanocrystals in tetrachloroethylene (TCE), spin coating, dip coating, or spray coating. TCE allowed for slow evaporation of solvent compared higher volatility solvents such as chloroform or toluene. SEM images comparing film qualities of nanocrystals deposited from TCE compared to chloroform is shown in Figure 4.1.

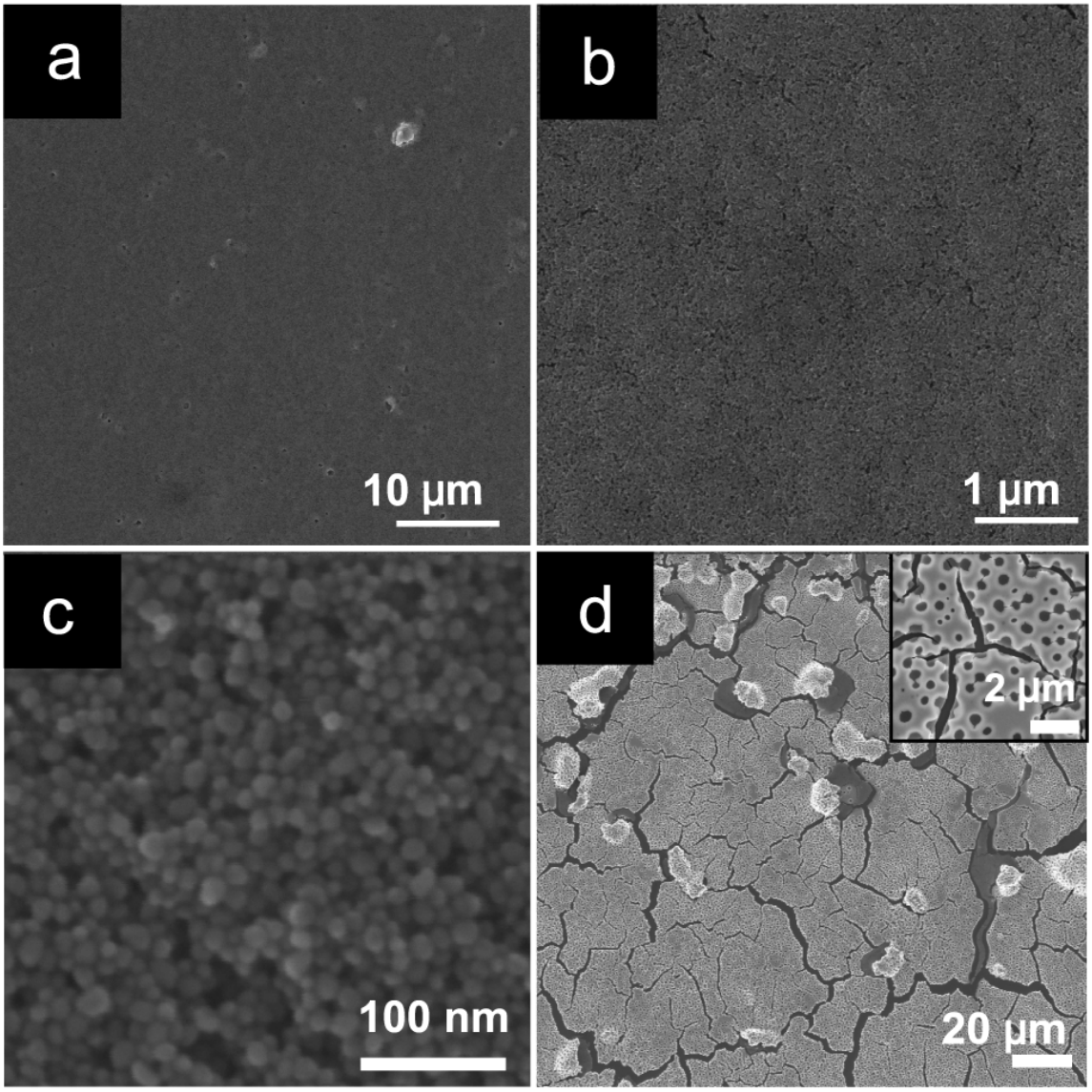

Figure 4.1. SEM images of CIS film drop cast from 5 mg/ml in TCE at various magnifications (a-c), CIS film dropped from 5mg/ml in Chloroform chloroform (d)

4.2.2. Dip coating

Figure 4.2 shows a profilometry measurement of a dip-coated nanocrystal film. This nanocrystal film was formed by multiple dipping steps. The film thickness depended on many parameters, including dipping speed, soak time, number of subsequent dips, dipping angle, solvent and nanocrystal concentration. For thinner films, the controlling parameter for thickness was the nanocrystal concentration. Multiple dips were explored as a way to increase film thickness, but this approach did not lead to thicker films. The striations in the film in Figure 4.2 were the result of subsequent dips. The striations had an increased thickness (i.e., the peaks in the thickness profile) but the total thickness of the film did not increase. This is probably due to simultaneous redispersion and deposition during the subsequent dip-coating steps.

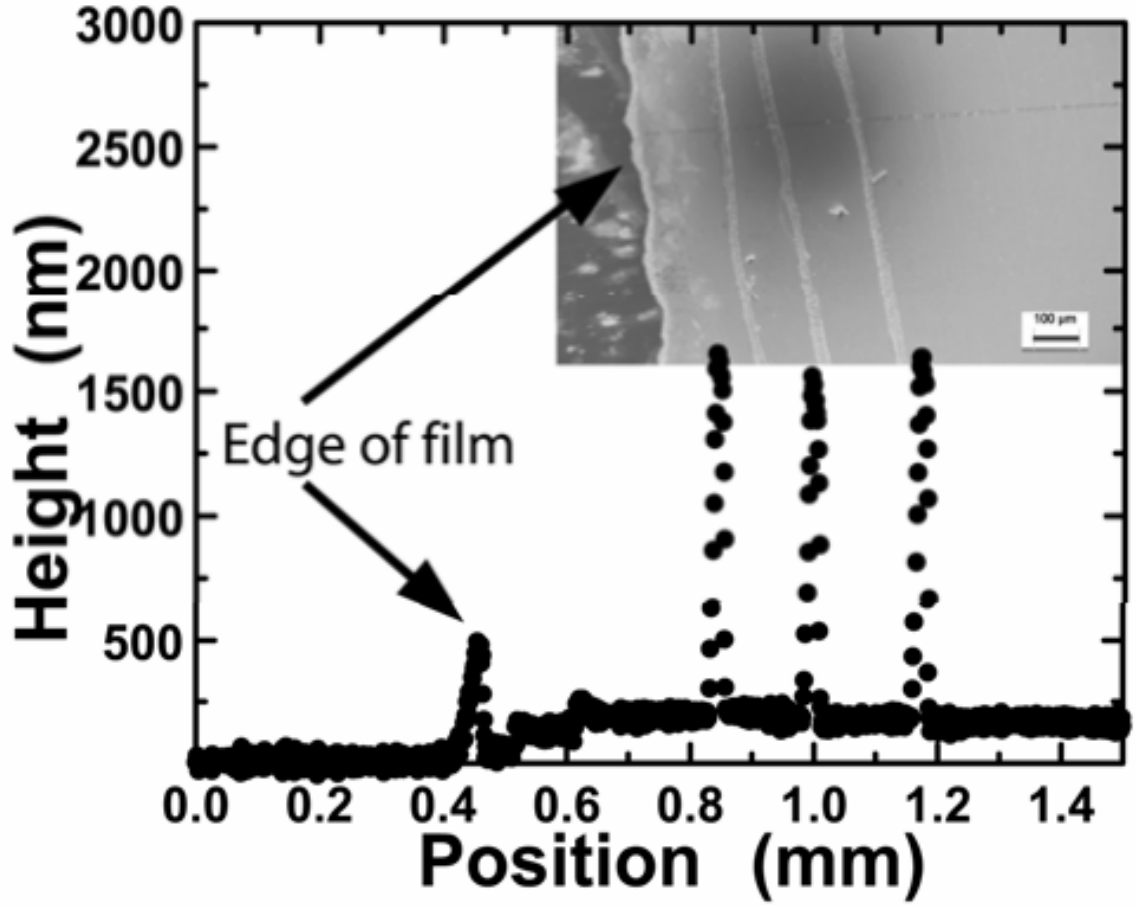

Figure 4.2. Profile of a dip-coated CIS film. Inset: SEM image of film dipped 4 times.

4.3. EXPERIMENTAL

4.3.1. Film treatments

The as-cast nanocrystal films showed very high resistivities due to ligands adsorbed onto the nanocrystal surfaces. To remove the ligands from the film, four routes were explored: thermal annealing, UV-ozone treatment, oxygen plasma treatment, and chemical treatments. All treatments were performed on copper indium selenide nanocrystal films ($CuInSe_2$; CIS), and thermal annealing experiments were performed on

both CIS and $CuIn_{0.56}Ga_{0.44}Se_2$ (CIGS) nanocrystals. Defect-free, ~600 nm-thick films are obtained by dispersing nanocrystals in TCE at relatively high concentrations (5 mg/mL) and drop casting the dispersion on a glass or Mo-coated glass substrate. 150 μL of these dispersions were drop cast onto a 12 x 25 mm substrate. The nanocrystal suspension was evaporated in a vacuum chamber at room temperature for 12 hours to remove solvent and completely dry the film.

4.3.2. Thermal annealing

The as-prepared nanocrystal films were annealed using a variety of different approaches, including heating under controlled atmosphere, and treatment by UV-ozone and oxygen plasma. Films were heated by placing the nanocrystal-covered substrate inside a tube furnace equipped with a 1 in. inner diameter quartz tube under gas flows (N_2, or 93%/7% N_2/H_2 mixture) or under air by detaching the gas fittings and using room air as the environment. Thermal treatments were done for one hour with a 25°C/min. ramp rate to the setpoint temperature.

4.3.3. UV-ozone and oxygen plasma treatment of nanocrystal films.

4.3.3.1. UV-ozone treatment

Nanocrystal films were placed in a Jelight Model 42 UV-Ozone chamber approximately 1 cm from the UV lamp. The UV-ozone chamber is equipped with low-pressure Hg-vapor grid with a lamp intensity of 28mW/cm2. Films were treated for 1 to 20 minutes.

4.3.3.2. Oxygen Plasma treatment

Nanocrystal films were placed in an Oxford Plasmalab 80 Plus RIE. A pressure of 600 mTorr and RF power of 50 W were used. Treatments were performed for up to 20 minutes.

4.3.4. Chemical Treatment

4.3.4.1. Hydrazine

Nanocrystal films were soaked in solutions of hydrazine of various concentrations in acetonitrile for at least 60 minutes.

4.3.4.2.Ethanedithiol

CIS nanocrystals spray coated onto a gold-coated glass substrate were soaked in a solution of 0.1 M ethanedithiol in acetonitrile for at least 60 minutes.

4.3.4.3.Methanol/acetone

CIS nanocrystals spray coated onto a gold-coated glass substrate were soaked in a 10% methanol solution in acetone for at least 60 minutes.

4.3.5. CIS Reaction Modifications

Previous research has determined that nanocrystal reactions that use tertiary phosphine chalcogenides as a chalcogen source can benefit from introducing a secondary phosphine to increase reactivity. This increased reactivity can increase yield. In these experiments, diphenylphosphine DPP was either 1. Added to the TBP:Se stock solution or 2. Used as a replacement for TBP in the reaction protocol described in Chapter 2, section 2.2.1.

4.4. RESULTS

4.4.1. Annealing under different gas environments

4.4.1.1. Annealing in air

CIS films annealed in air showed a slight reduction in the full width at half maximum in reflections upon annealing between 50 and 250°C. At 150°C, a peak emerges at approximately 32° 2θ, which matches up to crystalline Se. The Se may come from either excess precursor left in the nanocrystal solution that crystallizes upon heating, or from degassing from the nanocrystals.

At temperatures greater than 250°C, In_2O_3 begins to form, as well as CuO at ~500°C. This oxidation and change in structure is accompanied by a change in color from black/brown to light brown and semi-transparent. Figure 4.3 shows XRD patterns of the CIS films under different annealing temperatures in an air environment.

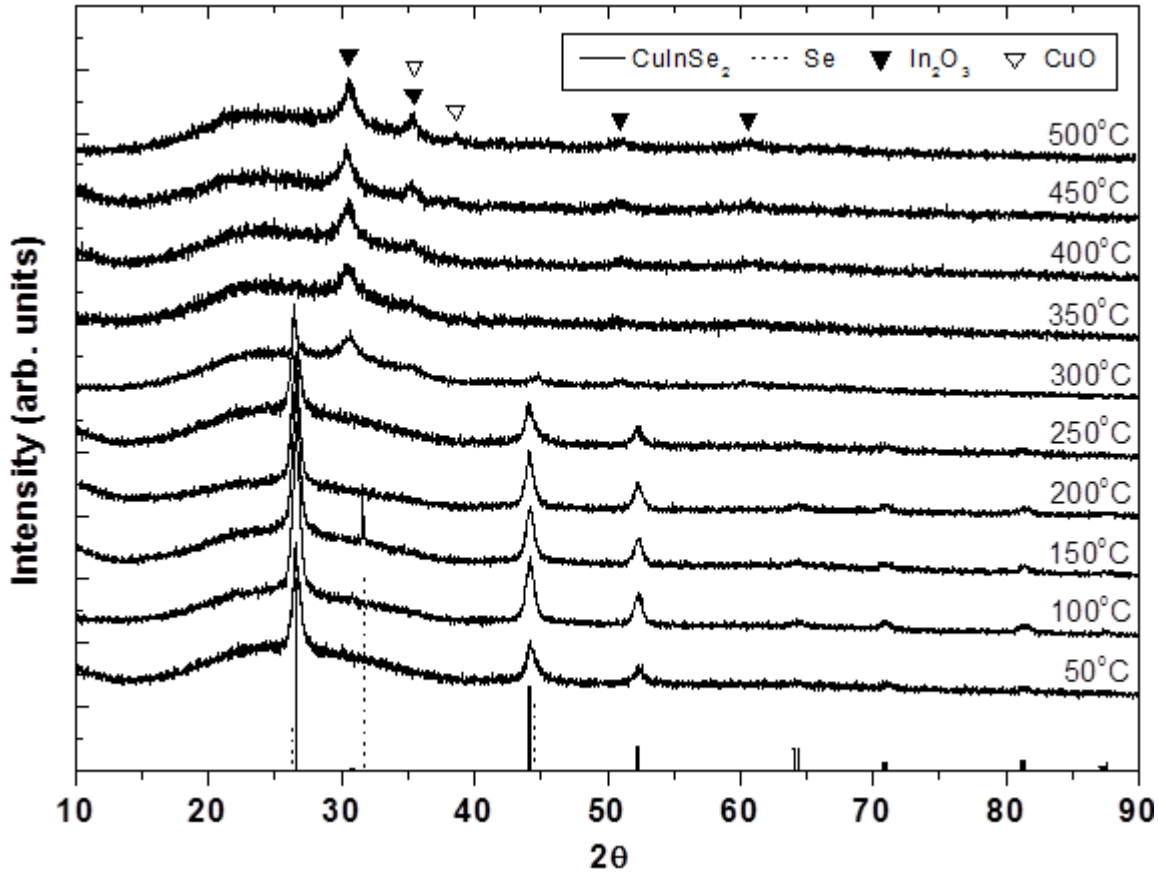

Figure 4.3. XRD spectra of CIS nanocrystal films annealed between 50 and 500°C in air.

4.4.4.2. Annealing in nitrogen

CIS films annealed in unpurified nitrogen showed a slight reduction in the full width at half maximum in reflections upon annealing between 50 and 500°C. At 150°C, a peak emerges at approximately 32° 2θ, which matches up to crystalline Se. The Se may come from either excess precursor left in the nanocrystal solution that crystallizes upon heating, or from degassing from the nanocrystals.

At temperatures greater than 300°C, In_2O_3 begins to form. This could be due to a slight amount of oxygen present in the unpurified nitrogen. Figure 4.4. shows XRD of nanocrystal films annealed in air.

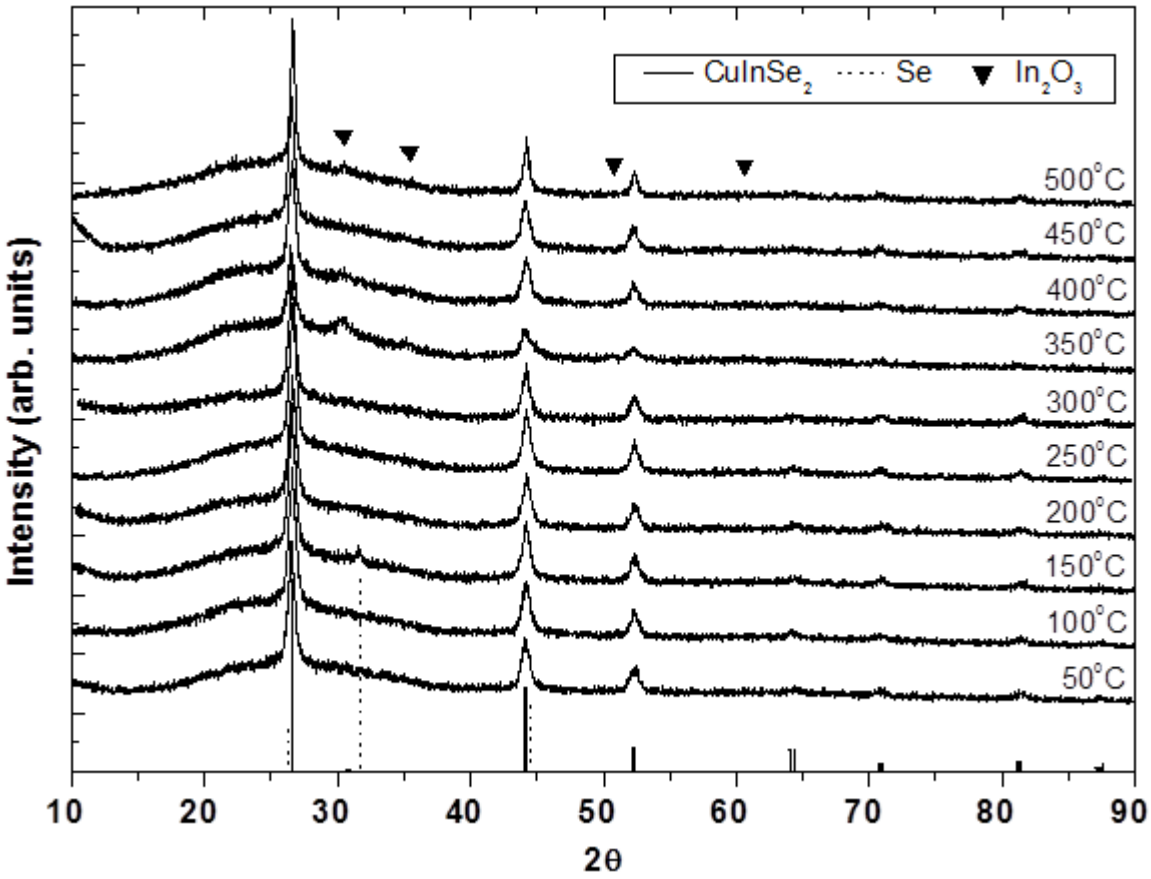

Figure 4.4. XRD spectra of CIS nanocrystal films annealed between 50 and 500 C in unpurified nitrogen.

4.4.4.3. Annealing in forming gas

CIS films annealed in forming gas showed a reduction in the full width at half maximum in reflections upon annealing between 50 and 500°C. At 150°C, a peak emerges at approximately 32° 2θ, which matches up to crystalline Se. The Se may come from either excess precursor left in the nanocrystal solution that crystallizes upon heating, or from degassing from the nanocrystals. No other phases are observed when annealing under forming gas. Figure 4.5 shows XRD patterns of films annealed under forming gas.

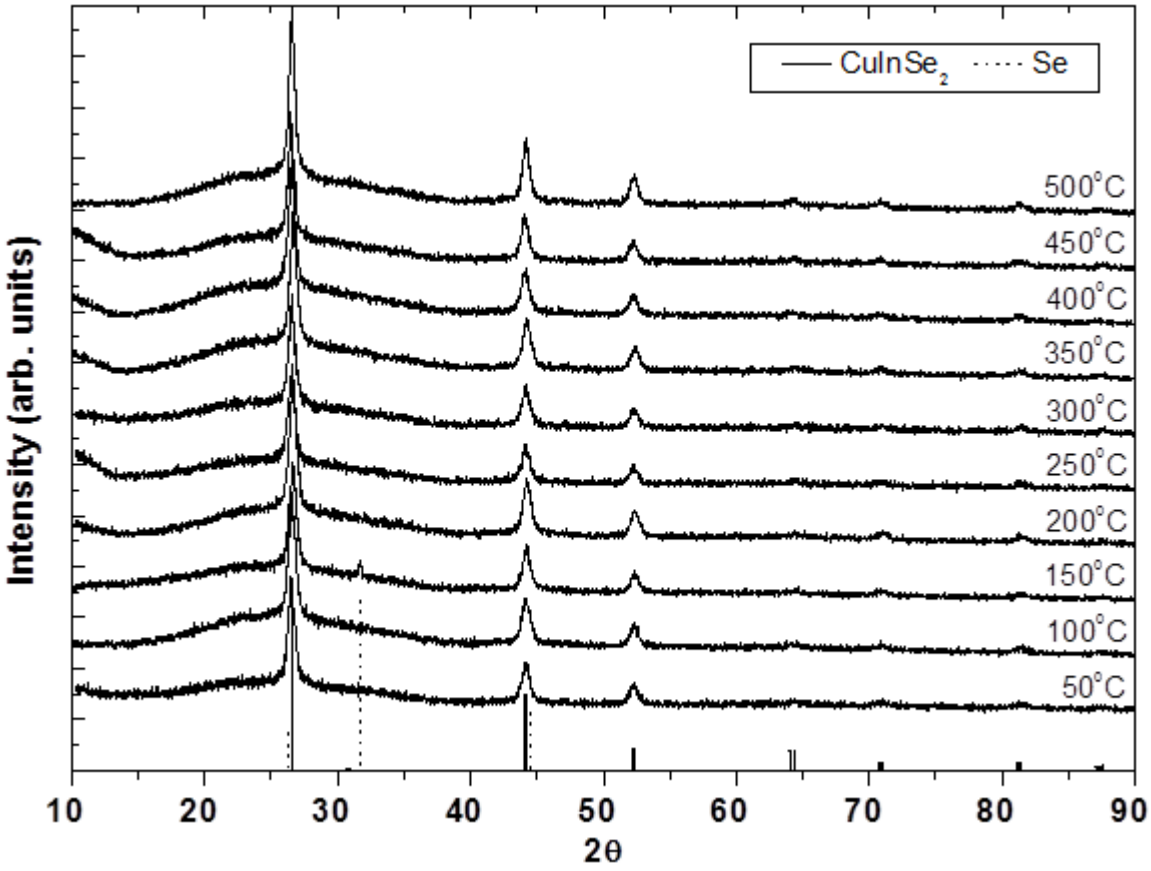

Figure 4.5. XRD spectra of CIS nanocrystal films annealed between 50 and 500°C in forming gas (7% H2, balance N2).

4.4.4.4. Oxygen content after annealing

Figure 4.6 shows the ratio of measured oxygen concentration compared to the sum of Cu and In concentrations measured by EDS. Under all gas environments, the oxygen content remains similar to the non-annealed 25°C) for temperatures under 200°C. At 200°C, the oxygen content in the sample in the air-annealed sample increases dramatically, indicating significant oxidation. At 350°C, the sample annealed under nitrogen shows oxygen levels higher than that of forming gas at the same temperature.

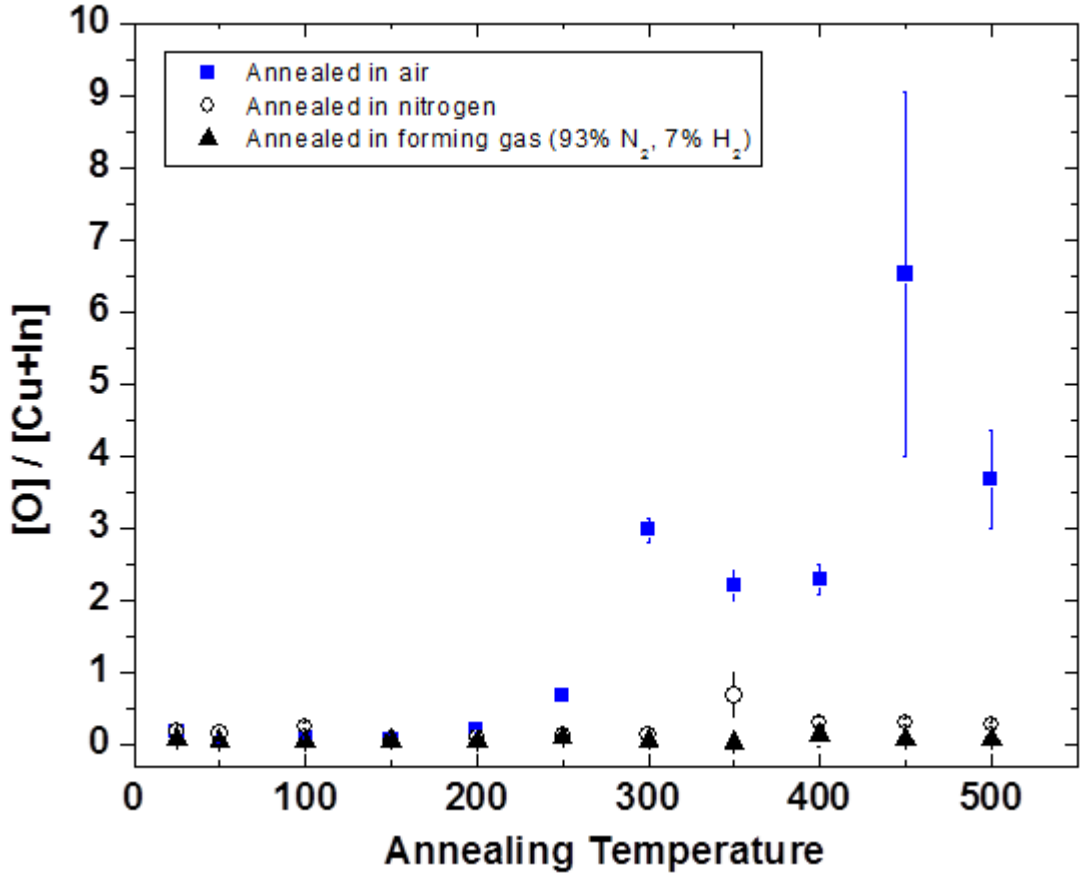

Figure 4.6. Oxygen content of CIS films as a function of annealing temperature under air, nitrogen, and forming gas environments.

4.4.4.5. Conductivity after annealing

Four point probe conductivity was measured on films after annealing (Figure 4.7). Initially, films had a sheet resistance of ~1000 Ω cm. Annealing in air resulted in the largest reduction in sheet resistance, by ~3 orders of magnitude after annealing to 250°C. This increase in conductivity could be due to removal of ligands, or creation of a surface oxide that is conductive. Annealing under forming gas and nitrogen result similar decreases in sheet resistance up to ~300°C, with a ~10x decrease in sheet resistance with

annealing at 100°C and a ~20x decrease in sheet resistance upon annealing at 250°C. At higher temperatures, the nitrogen annealed CIS films exhibit lower sheet resistances compared to films annealed likely due to oxidation. Further study must be done to determine whether the decreased sheet resistance is due to an increase in carrier mobility due to increased nanocrystal coupling, or an increase in carrier concentration resulting from slight compositional changes (Se degassing) and or surface states (ligand removal, oxidation). This reduction in sheet resistance could potentially lead to improved device performance in solar cells if the reduced sheet resistance is due to increased mobility.

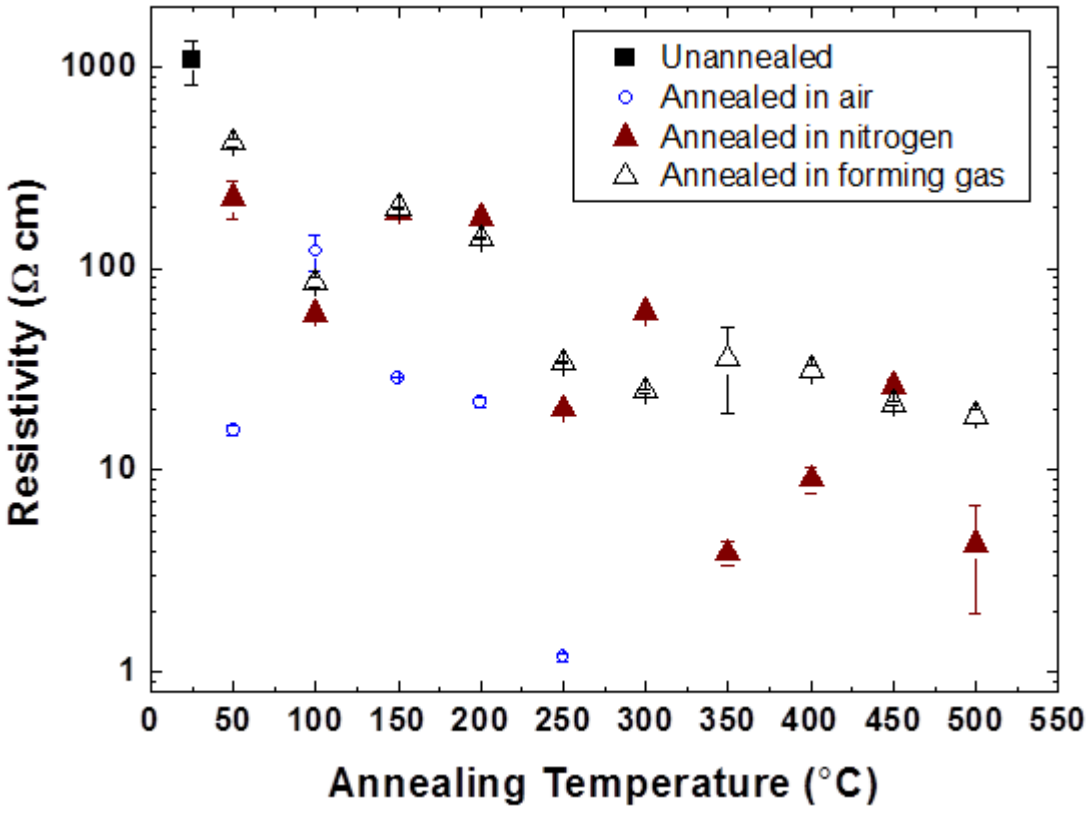

Figure 4.7. 4-point probe conductivity of films annealed between 50 and 500 C in air, nitrogen, and forming gas.

4.4.2. Oxygen plasma and UV-ozone treatment of CIS films

UV-ozone and oxygen plasma treatments were done on films in attempt to oxidatively remove or "burn" away ligands. These techniques are commonly used to remove organic material from silicon wafers and other substrates.

4.4.2.1. Effect of UV ozone and Oxygen plasma on Crystal Structure

There is no observed crystallographic change by exposing CIS nanocrystal films to oxygen plasma. Figure 4.8 shows XRD patterns of CIS films exposed to UV ozone between 1 and 10 minutes.

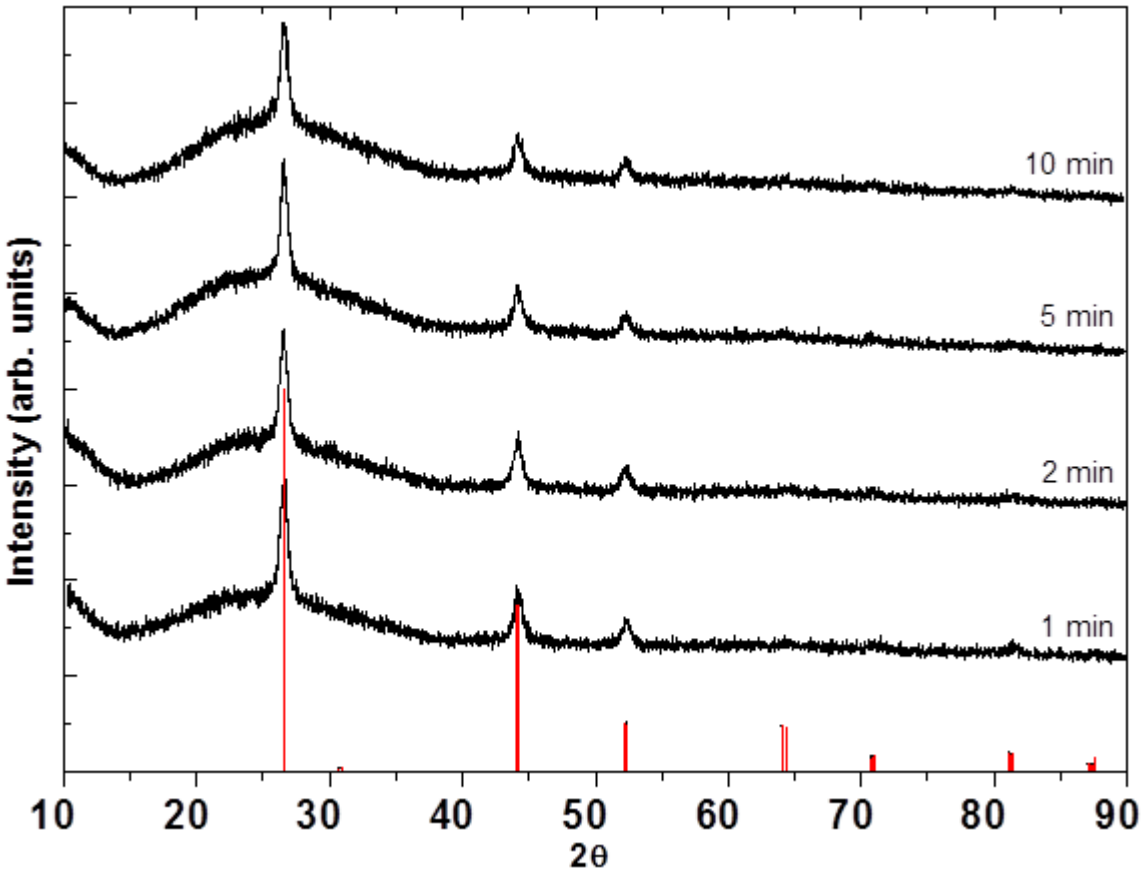

Figure 4.8. XRD patterns of CIS films exposed to Oxygen plasma between 1 and 10 minutes.

There is no observed crystallographic change by exposing CIS nanocrystal films to UV-ozone. Figure 4.9 shows XRD patterns of CIS films exposed to UV ozone between 1 and 10 minutes.

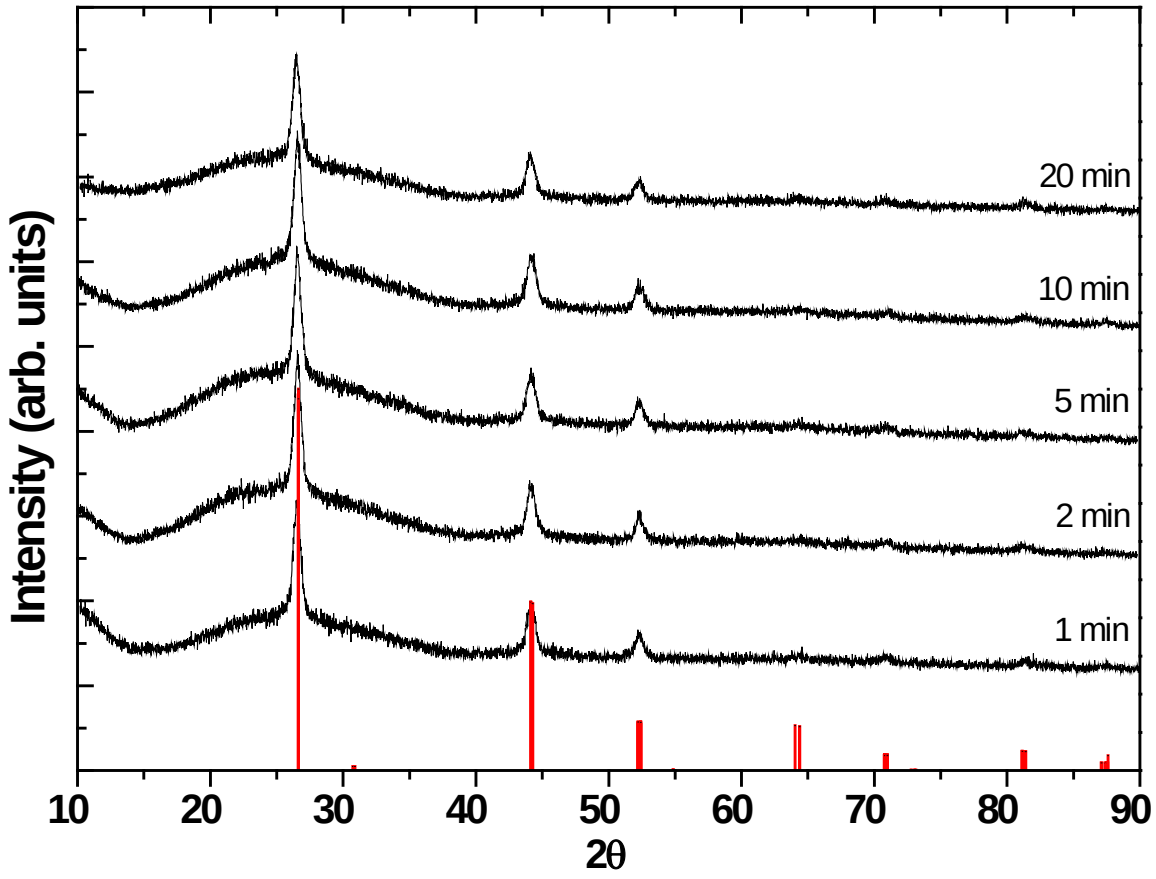

Figure 4.9. XRD patterns of CIS films exposed to UV ozone between 1 and 20 minutes.

4.4.2.2. XPS of UV-ozone treated films

XPS of UV-ozone treated films (Figure 4.10) shows significant surface oxidation, resulting in a relative increase of signal of a peak at 60.5 eV relative to the Se 3d peak (~56 eV). This corresponds to oxidation of surface selenium atoms.

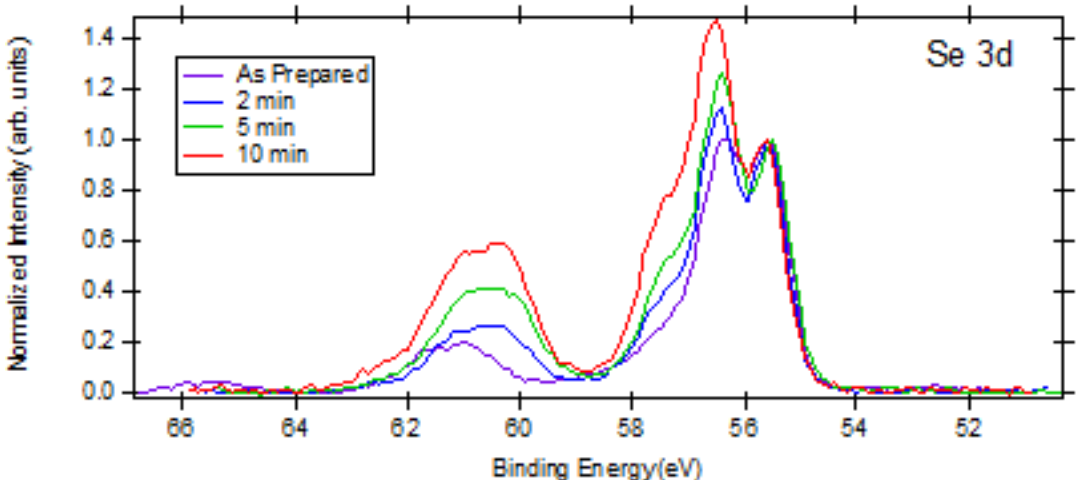

Figure 4.10. XPS of UV-ozone treated nanocrystals.

4.4.2.3. Resistivity of UV ozone and Oxygen plasma treated CIS films

The sheet resistance of UV ozone and Oxygen plasma treated CIS films (Figure 4.11) increased with any amount of processing. Initially, films had sheet resistances of ~200 – 300 Ω cm. After only one minute of either UV ozone or Oxygen plasma treatment, the sheet resistance rose to over 1000 Ω cm. After 10 minutes, sheet resistances were over 10,000 Ω cm. There was not a significant difference in the sheet resistances for the same processing time for each treatment. After 20 minutes of UV ozone exposure, the sheet resistivity was over 200,000 Ω cm.

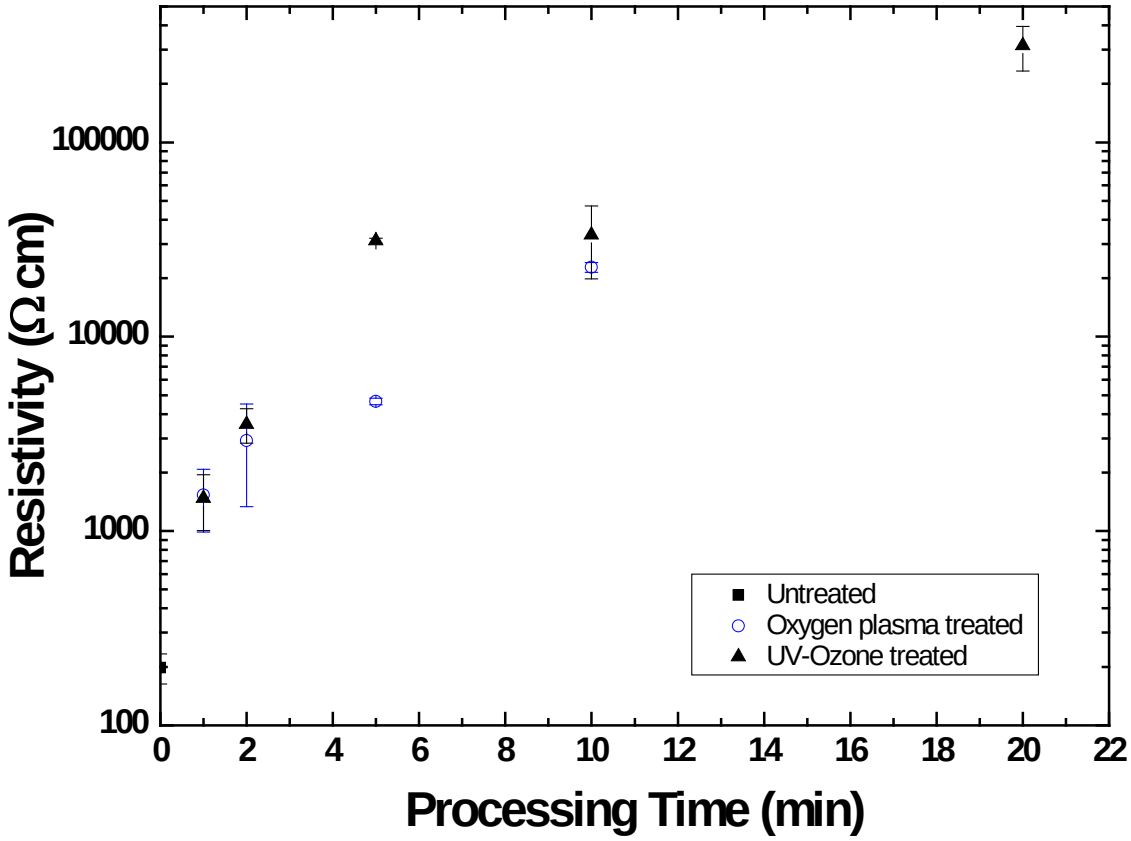

Figure 4.11. Sheet resistance of UV ozone and Oxygen Plasma treated films as a function of processing time.

4.4.3. Chemical Treatments of CIS Nanocrystal films, Effects on PV Device Behavior

Devices utilizing spray coated CIS nanocrystal films soaked in various solutions were fabricated. This was in effort to displace the ligands coating the surface and increase interparticle coupling, improving device efficiency. For each experiment, a 900 nm thick CIS nanocrystal film was spray coated onto a gold-coated (thermal evaporation) patterned glass substrate. CdS deposited by chemical bath deposition, using a method described by by McCandless and Shafarman.[9] A transparent top contact of intrinsic ZnO

and In_2O_3:SnO_2 (ITO) was deposited by sputtering. Detailed studies of power conversion efficiencies were done using a Keithley 2400 General Purpose Sourcemeter and a Xenon Lamp Solar Simulator (Newport) equipped with an AM1.5 filter. Series and shunt resistances (Rs and Rsh, respectively) were determined by fitting the following equation using least squares regression to I-V curves under dark conditions:

$$J = J_0\left(e^{\frac{q(V+JAR_s)}{kT}} - 1\right) - \frac{V + JAR_s}{R_{sh}} \quad (1)$$

4.4.3.1. Untreated Film

Devices were fabricated using a 900 nm CIS film with no film treatments to use as a reference. I-V characteristics of a typical device under dark and AM1.5 illumination are shown in Figure 4.12. Of 8 devices tested, the average PCE was 0.42+/- 0.07

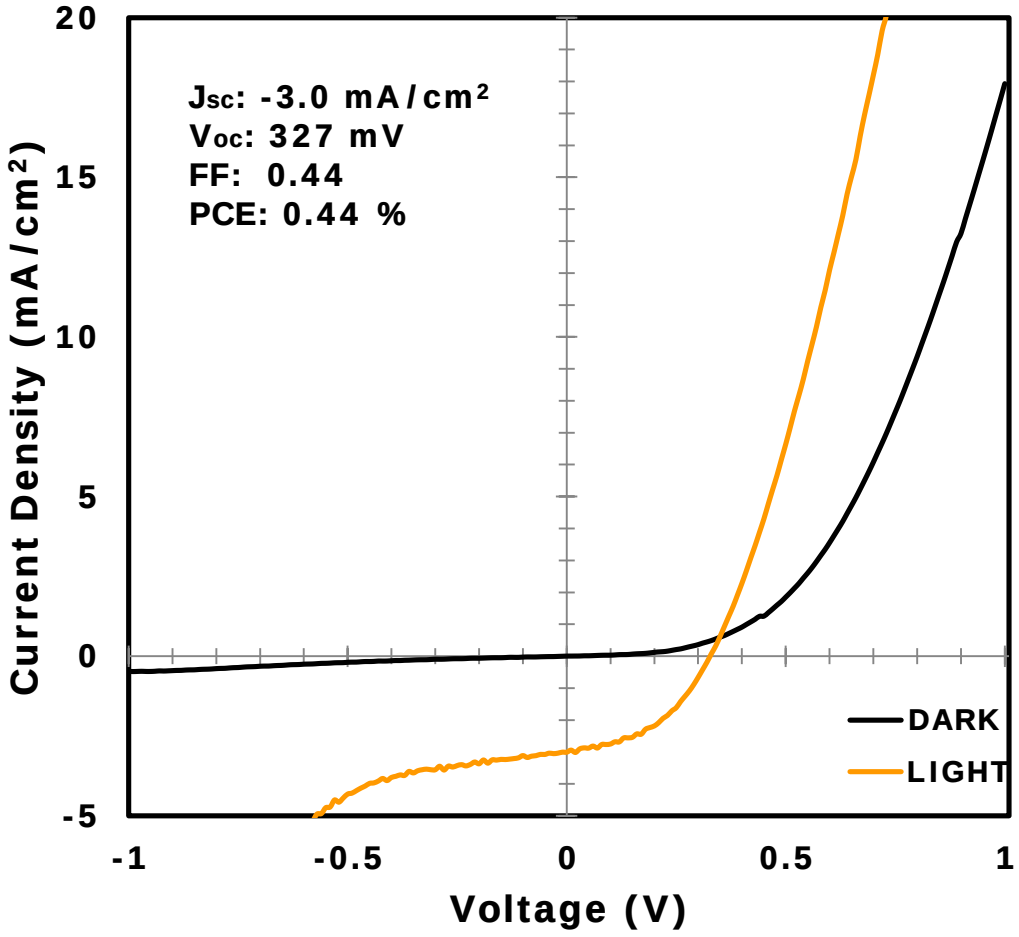

Figure 4.12. I-V characteristics of a typical PV device fabricated using an untreated CIS film as the absorber layer. Measurements were performed in the dark and under AM1.5 illumination.

4.4.3.2. Ethanedithiol (EDT) treated film

Devices were fabricated using a 900 nm CIS film treated with EDT. I-V characteristics of a typical device under dark and AM1.5 illumination are shown in Figure 4.13. Of 5 devices tested, the average PCE was 0.55+/- 0.04%.

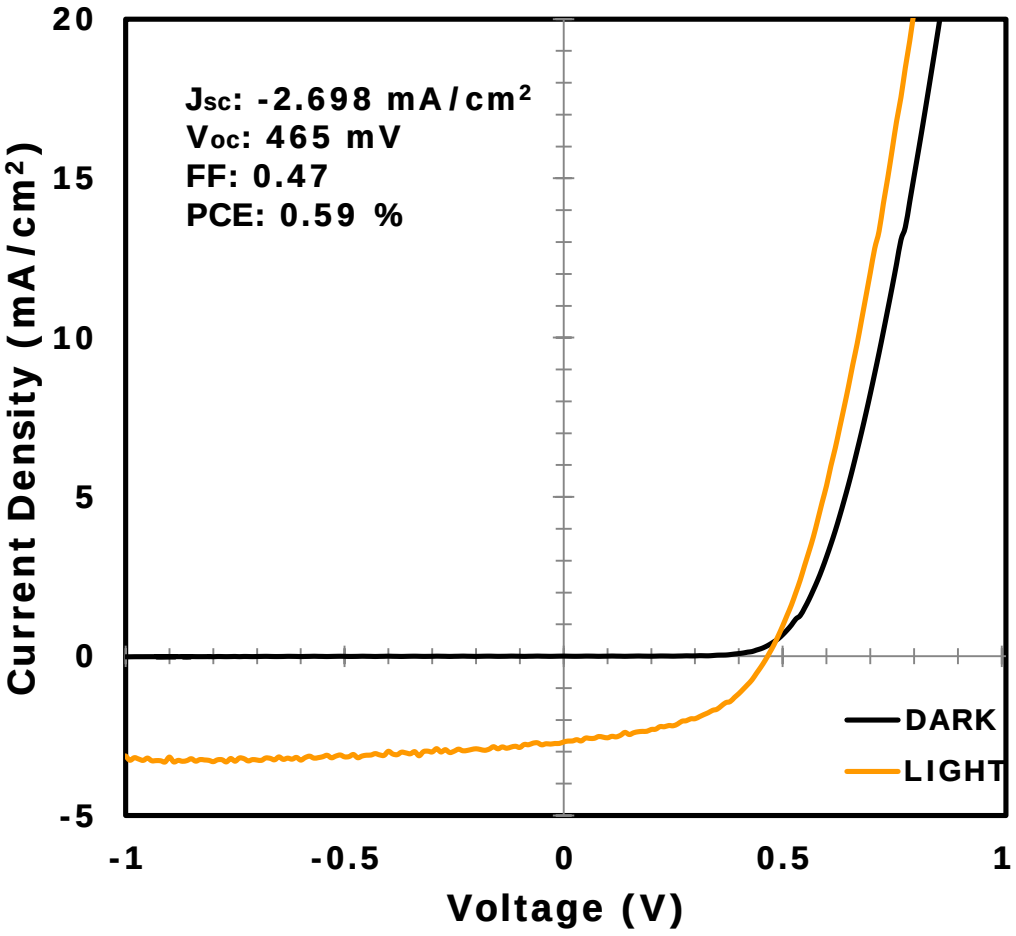

Figure 4.13. I-V characteristics of a typical PV device fabricated using an EDT-treated CIS film as the absorber layer. Measurements were performed in the dark and under AM1.5 illumination.

4.4.3.3. Hydrazine (HYZ) treated film

Devices were fabricated using a 900 nm CIS film treated with HYZ. J-V characteristics of a typical device under dark and AM1.5 illumination are shown in Figure 4.14. Of 5 devices tested, the average PCE was 0.16+/- 0.03%. One interesting observation about devices using HYZ-treated absorbers is that the J-V curves in the light and dark do not cross each other, which occurs frequently in untreated devices, as well as devices treated using other methods. This crossover is typically attributed to an energetic barrier at the CdS/CIS interface. This occurs because Cu ions diffuse into the CdS layer. It is possible that treating with HYZ changes the quasi-fermi level of electrons so this barrier does not exist, or that the HYZ removes Cu ions that would diffuse into the interface, avoiding this problem altogether.

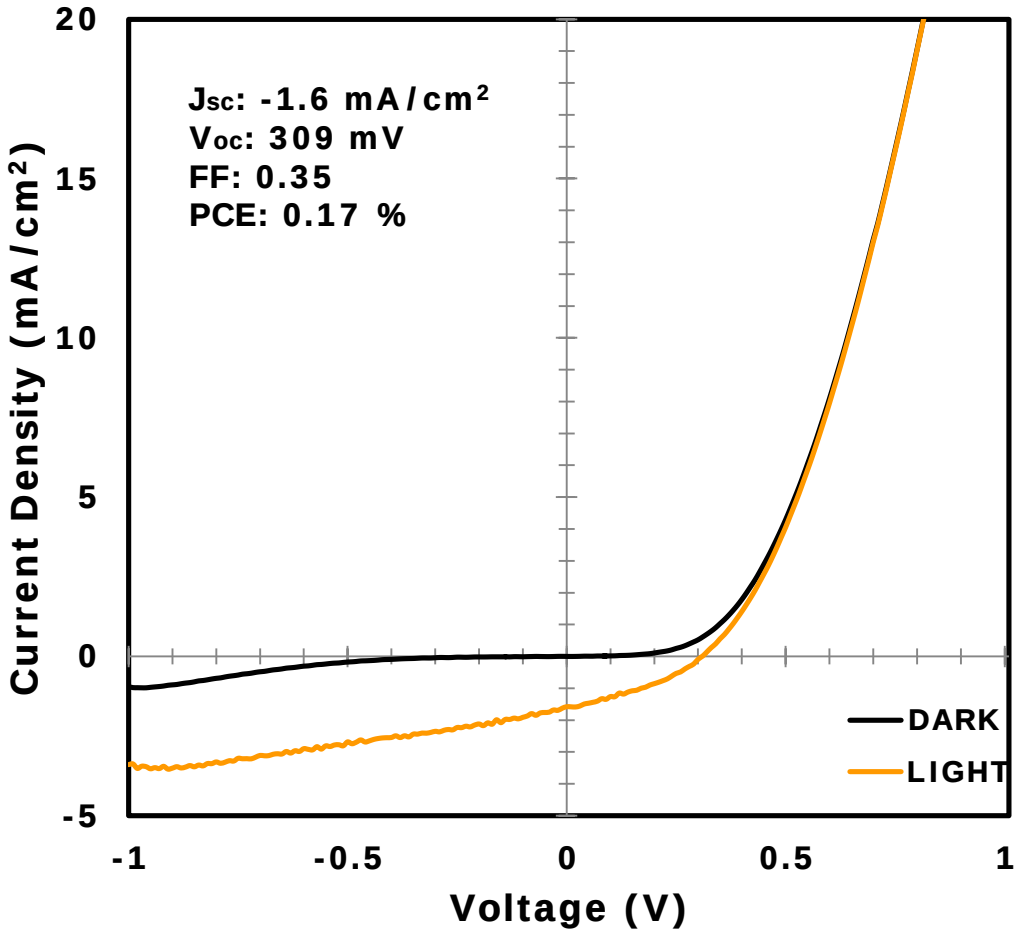

Figure 4.14. I-V characteristics of a typical PV device fabricated using an HYZ-treated CIS film as the absorber layer. Measurements were performed in the dark and under AM1.5 illumination.

4.4.3.4. Methanol (MeOH) treated film

Devices were fabricated using a 900 nm CIS film treated with methanol in acetone. J-V characteristics of a typical device under dark and AM1.5 illumination are shown in Figure 4.15. Of 5 devices tested, the average PCE was 0.22+/- 0.05%.

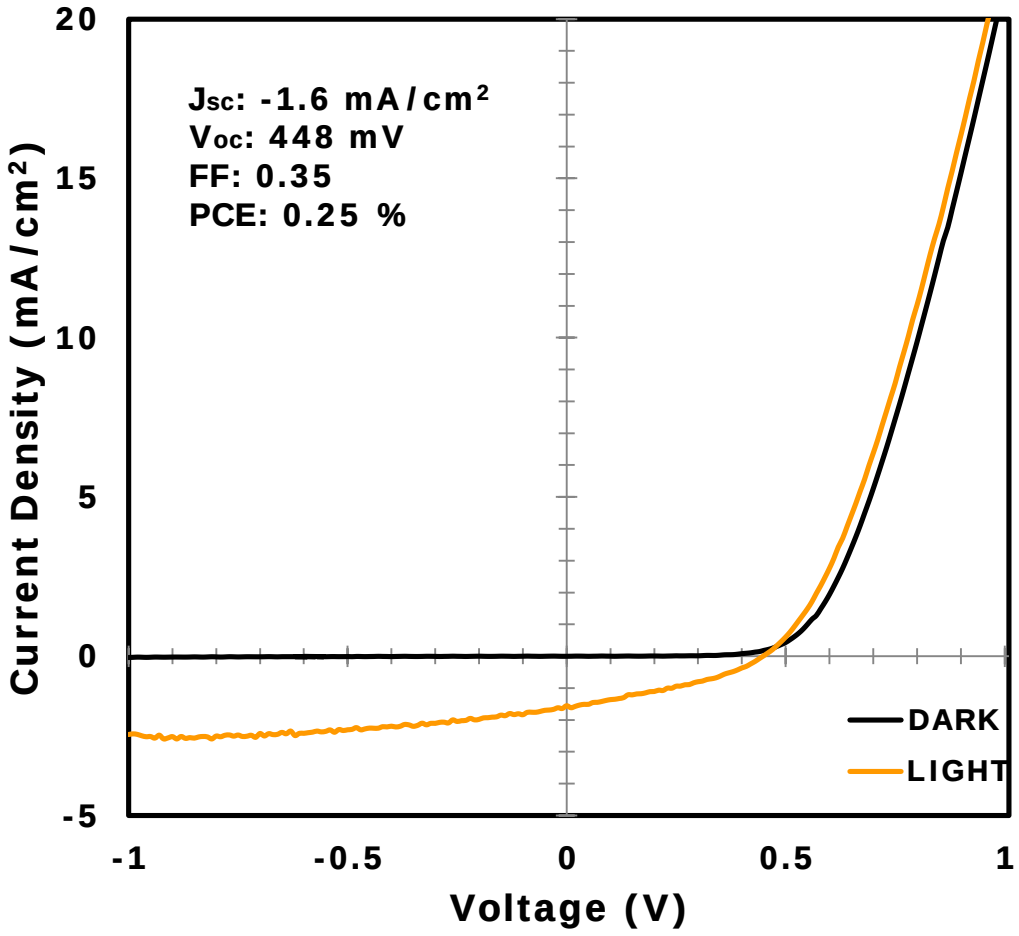

Figure 4.15. I-V characteristics of a typical PV device fabricated using an absorber layer soaked in a methanol/acetone solution. Measurements were performed in the dark and under AM1.5 illumination.

4.4.4. Use of Secondary Phosphines in CIS NC Reaction

4.4.4.1. Adding diphenylphosphine to reaction

Figure 4.16 shows the I-V characteristics of a solar cell made from CIS nanocrystals with 2 mmol (~150 μL) diphenylphosphine (DPP) added to the reaction.

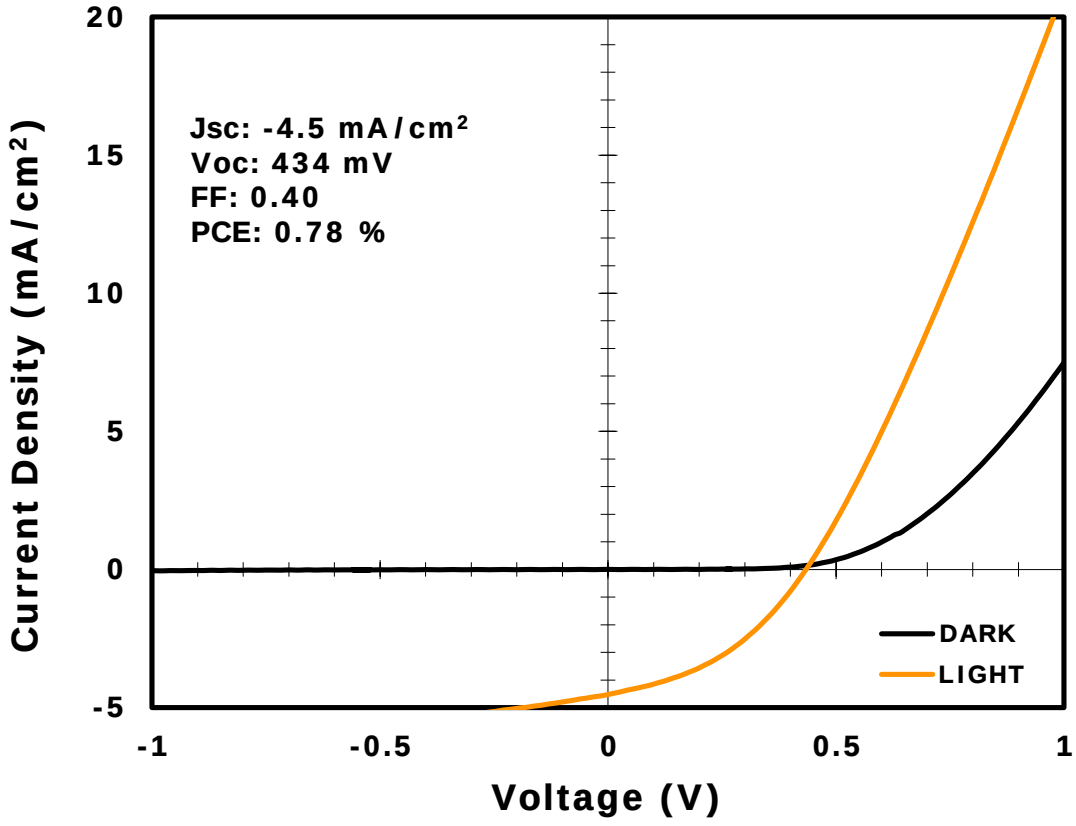

Figure 4.16. I-V characteristics of a CIS nanocrystal device with DPP added to the CIS nanocrystal reaction.

These measured Jsc, Voc, and resulting PCE are consistent with devices made without TBP.

4.4.4.1. Replacing TBP with DPP

Replacing TBP with DPP in the CIS nanocrystal reaction had a dramatic impact in the device Voc. Figure 4.17 shows typical I-V characteristics from a device made with particles synthesized using DPP:Se instead of TBP.

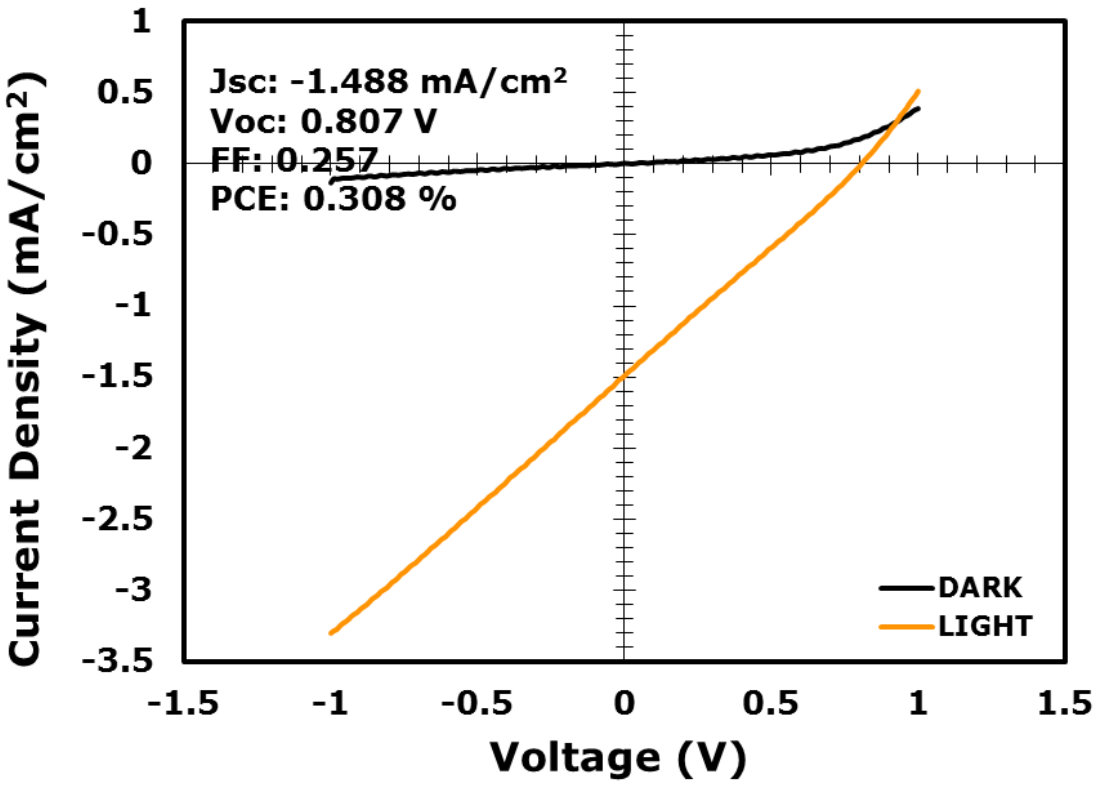

Figure 4.17. I-V characteristics of a typical CIS nanocrystal device with DPP added to the CIS nanocrystal reaction.

The Voc measured in these devices was typically around 700 to 800 mV. This is nearly double typical values for Voc with CIS particles synthesized using TBP:Se as the selenium source. The diode behavior looks unusual. The straight-line behavior implies a

very low shunt resistance, possibly due to high film conductivity. The high conductivity along with high Voc is consistent with a very high carrier concentration in the film.

4.5. DISCUSSION

4.5.1. Annealing of CIS nanocrystal Films

Annealing of CIS nanocrystal films resulted in increases of film conductivity for all environments. Annealing under air and unpurified nitrogen result in oxidation and some phase transformations for temperatures over 200°C. Not surprising phase transformations to crystalline oxides occur at lower temperature in air compared to nitrogen. A dramatic decrease in sheet resistance can be correlated with formation of these crystalline oxides. Surprisingly, crystalline Se forms in every sample at 150°C. One aspect of annealing under high temperatures that may be undesirable is "outgassing" of Se from films. Crystalline Se forms within the film at 150°C, while at higher temperatures, Se deposits are found on the tube furnace walls directly above the substrate. The effect of Se outgassing on the electronic properties of CIS is unknown, but it likely creates undesirable defects in the crystal lattice.

4.5.2. Oxygen Plasma and UV ozone Treatments of CIS Films

Even short processing of CIS films in a UV ozone or Oxygen plasma environment result in severe oxidation. This oxidation is confirmed by XPS to be surface oxidation of Se. While no crystallographic change is found – the XRD peaks remain identical in these processing, the sheet resistance *increases* by several orders of magnitude. Interestingly, annealing in air at lower (<250°C) does not cause any change in in crystal structure,

while oxidizing the material but causes an equally remarkable decrease in sheet resistance. Further study could enlighten how the mechanistic differences in these treatments create films that cause an apparently similar reaction (surface oxidation with no crystallographic change) but opposite effects in sheet resistance.

4.5.3. Chemical Treatment of Absorber Films

Chemical treatment of absorber films yielded varying results. Compared to a control device with no absorber treatment, treatment with ethanedithiol yielded superior efficiency via an increase in Voc and FF. Treatment with hydrazine caused a slight reduction in Voc accompanied by a large decrease in Jsc. Surprisingly, soaking the films in a methanol/acetone solution causes a large increase in Voc, but a significant decrease in Jsc compared to the control. The PCE, Jsc, Voc, FF, Rs, and Rsh averages for these treatments is shown in Figure 4.16.

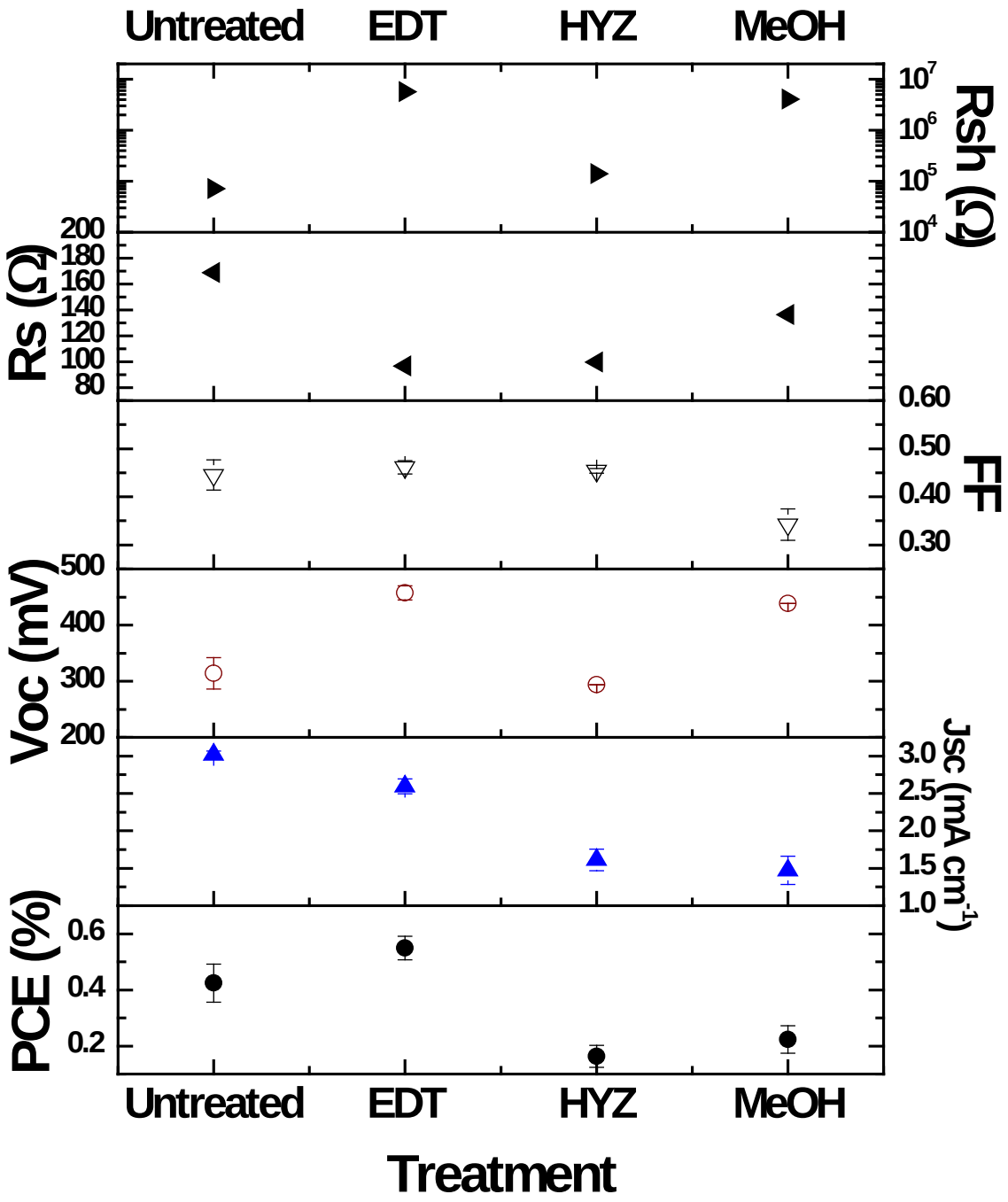

Figure 4.16. PCE, Voc, Jsc, FF, Rs, and Rsh as a function of chemical treatment. Error bars indicate standard deviation of measurement of at least 4 devices.

Another interesting aspect to note is the series and shunt resistances of these devices. Treating with hydrazine and ethanedithiol is expected to displace ligands from the nanocrystal film and replace them with the respective molecules. The effect of these treatments is a decrease in total device series resistance of ~40% compared to the control. This is a dramatic decrease in series resistance, as the top contact features a resistive intrinsic ZnO layer, as well as a sub-optimal ITO layer which add an appreciable amount of series resistance to the device.

While EDT treatment increases the device Voc by 46% and reduces Rs by ~40%, the Jsc decreases by 20%. This behavior is consistent with an increase in hole concentration in the CIS film. Increasing the concentration of free holes in the CIS film would increase the Voc, as Voc is proportional to the logarithm of the majority carrier concentration.[10] This increase in carrier concentration would cause a decrease in depletion width. As discussed in Chapter 3, the depletion region decreases with an increase in Voc. The depletion region for untreated films is found to be low (~50 nm), and a further increase in free carrier concentration would further reduce the depletion region, reducing the effective "useful" region of the absorber – the region of the absorber where photogenerated carriers can be extracted efficiently. In these devices the increase in Voc overcame the decrease in Jsc to cause an overall increase in PCE.

Hydrazine is a known n-type dopant in nanocrystal films.[2] However, the high vacuum condition necessary for depositing top contacts most likely causes most or all of the hydrazine to desorb from the nanocrystal surface. The Voc of HYZ treated films is ~7% lower than the untreated film.

Soaking the CIS films in a methanol/acetone solution resulted in a 39% increase in Voc. This is a surprising result, and may be attributed to a reduction in free ligand or some other species that acts as a trap. It is worth noting that Rsh increases by nearly two orders of magnitude compared to the control. It is possible that soaking in the solution allows for some conformational change in the film that reduces shunting, increasing Voc. The decrease in Jsc is more difficult to explain, and further work must be done in order to understand this behavior.

4.5.4. Use of a Secondary Phosphine Selenide as Se precursor

Using diphenylphosphine selenide as a Se precursor results in a surprising and unexpected increase in Voc. Recent work by the Norris and Aydil groups have found a similar result in PbSe nanocrystal-based solar cells.[11] In this study, nanocrystals synthesized using DPP had a significantly *lower* Voc compared to nanocrystals synthesized with a tertiary phosphine selenide. These results imply that the ligands used during synthesis can play a crucial role in the electronic properties of nanocrystal films.

4.6. CONCLUSIONS

Thermal processing of CIS nanocrystal films resulted in decreases in sheet resistance regardless of the environment. Annealing in air and nitrogen resulted in phase transformation to oxides at high temperature. No phase transformations occurred in CIS nanocrystal films heated under forming gas up to 500°C. Oxidative treatments (UV ozone and oxygen plasma) oxidized surfaces and caused a dramatic increase in sheet resistance, which increased with increased processing time. No change in crystal structure (phases, intensity, or peak shape) was found during these oxidative treatments.

Interestingly, low temperature (< 250°C) annealing in air causes oxidation that results in a decrease in sheet resistance.

The effect of chemical treatments on Voc was either positive (EDT, methanol/acetone) or negative (HYZ). While the power conversion efficiencies did not improve by very much using chemical treatments (a modest improvement for EDT treated films), this study does show some promise in manipulating the carrier concentration. Changing the selenium precursor resulted in a drastic increase of Voc, which combined with the very low shunt resistance of the device, indicates that the film could be very highly doped. Controlling carrier concentrations in films is crucial to developing highly efficient nanocrystal-based solar cells.

4.7. REFERENCES

1. Murray, C. B.; Norris, D. J.; Bawendi, M. G. *Journal of the American Chemical Society* **1993,** 115, (19), 8706-8715.

2. Talapin, D. V.; Murray, C. B. *Science* **2005,** 310, (5745), 86-89.

3. Jackson, P.; Hariskos, D.; Lotter, E.; Paetel, S.; Wuerz, R.; Menner, R.; Wischmann, W.; Powalla, M. *Progress in Photovoltaics: Research and Applications* **2011,** 19, (7), 894-897.

4. Yu, D.; Wang, C.; Wehrenberg, B. L.; Guyot-Sionnest, P. *Physical review letters* **2004,** 92, (21), 216802.

5. Law, M.; Luther, J. M.; Song, Q.; Hughes, B. K.; Perkins, C. L.; Nozik, A. J. *J Am Chem Soc* **2008,** 130, (18), 5974-85.

6. Gur, I.; Fromer, N. A.; Alivisatos, A. P. *The journal of physical chemistry. B* **2006,** 110, (50), 25543-6.

7. Luther, J. M.; Law, M.; Song, Q.; Perkins, C. L.; Beard, M. C.; Nozik, A. J. *ACS nano* **2008,** 2, (2), 271-80.

8. Lee, J.-S.; Kovalenko, M. V.; Huang, J.; Chung, D. S.; Talapin, D. V. *Nature Nanotechnology* **2011,** 6, (6), 348-352.

9. McCandless, B. E.; Shafarman, W. N. Chemical Surface Depostion of Ultra-Thin Semiconductors. 6,537,845, 2003.

10. Nelson, J., *The Physics of Solar Cells*. Imperial College Press: 2003.

11. Leschkies, K. S.; Beatty, T. J.; Kang, M. S.; Norris, D. J.; Aydil, E. S. *ACS nano* **2009,** 3, (11), 3638-3648.

Chapter 5: $CuInS_XSe_{2-X}$ (CISS) Nanocrystals for *in vivo* Imaging

5.1. INTRODUCTION

Semiconductor nanocrystals dots have emerged as a competitive technological option due to their interesting electronic and optical properties. Recently, nanocrystals with emission or absorption in the near-infrared (NIR) have found applications in light-emitting diodes[1, 2], photovoltaics,[3-6] and as fluorescent probes for bioimaging.[7-9] Nanocrystals with optical properties in the NIR are especially of interest for use for biological applications, due to low absorbance of tissue and water within the 650900 nm spectral window.[10] Hessel and coworkers recently synthesized $Cu_{2-x}Se$ nanocrystals that have strong NIR absorbance and demonstrated their potential for photothermal therapy.[11] A noninvasive fluorescent probe is ideally nontoxic and can emit light in response to external stimuli.

5.2. EXPERIMENTAL

5.2.1. CISS Nanocrystal Encapsulation

We used CISS nanocrystals encapsulated in a microparticle based oral vaccine system to demonstrate biological imaging in deep tissue. Previous work has illuminated the ability of a protein, invasin, to target intestinal M cells, which play a critical role in gut immunity.[12, 13] These M cells are extremely rare, occurring on the order of 1 in 10,000,000 enterocytes.[14] Thus the ability to target these M cells may play an essential role in developing a feasible oral vaccine. The affinity of invasin for its receptor, α5β1,

can be abrogated upon a single amino acid mutation, D911A. [15] In this study we tested the targeting ability of an invasin-functionalized vaccine delivery system. We encapsulated the CISS nanocrystals in poly (lactic-co-glycolic) acid microparticles to serve as a contrast agent for whole animal fluorescent imaging. Previous work has been done using quantum dots for in-vivo imaging, including CdSe[16-18], InAs,[19] and $CuInS_2$. [20] These studies all delivered the nanocrystals via injection into muscle or bloodstream. To encapsulate the nanocrystals in PLGA microparticles, organic-ligand capped CISS nanocrystals were added to the oil phase of a water/oil/water emulsion used to produce the microparticles. We utilized two sample groups: 1) microparticles conjugated to the extracellular portion of wild-type invasin expressed as a fusion protein on the C-terminus of maltose binding protein (MBP), 2) microparticles conjugated to the same protein with the D911A mutation. SEM and fluorescence microscopy were used to image the CISS nanocrystal-loaded microparticles are shown in Figure 5.1. SEM shows that the microparticles have sizes between approximately 500 and 2000 nm. Fluorescence microscopy images of the microparticles taken while exciting the sample with a green light confirms that the CISS nanocrystals are encapsulated within the spheres.

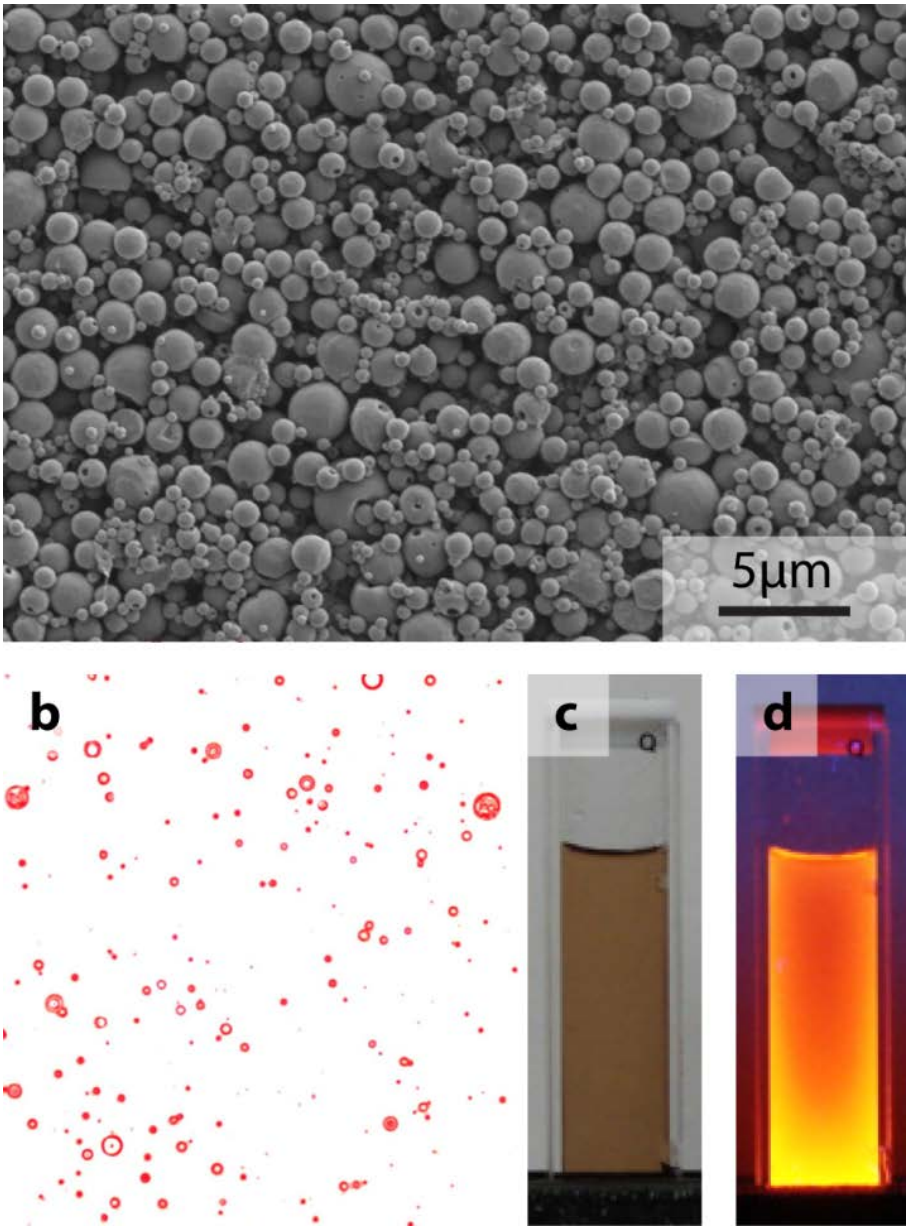

Figure 5.1. (a) SEM images and (b) fluorescence microscopy images of CISS nanocrystal-loaded PLGA microparticles. Photographs showing dispersions of ZnS@CISS nanocrystals in cuvettes before encapsulation (c) in room light and (d) under a fluorescent lamp.

5.2.2. Conjugation of PLGA Microparticles with MBP-INV fusion protein

420mg of PLGA microparticles encapsulating CISS nanocrystals were resuspended in 16.8ml of 0.1M MES buffer 0.5M NaCl (pH 5.0). 100ul ddH_2O containing 280mg of EDC and 100ul ddH_2O containing 320mg of Sulfo-NHS were added to the microparticle suspension. The reaction was rotated for 2 hours at room temperature. After activation, the 2x8ml of the suspension were transferred to new 50ml conicals. 200mM HEPES 200mM NaCl pH 7.4 was added to 50ml and the microparticles were pelleted. The activated microparticles were resuspended with 10ml of 200mM HEPES 200mM NaCl pH 7.4. 10ml of the same buffer containing 10mg of the respective MBP-INV variant, wild-type or D911A, was added to the microparticles and rotated for 2 hours at room temperature. The microparticles were then washed twice in 10mM HEPES 50mM NaCl pH 7.4 and resuspended in 3ml ddH_2O containing 20mg of α,α-Trehalose. The samples were frozen in liquid nitrogen lyophilized as before.

5.2.3. In vivo Fluorescene Imaging

6-8 week old female albino (BALB/c) mice were purchased from Jackson Laboratories and housed in at the Animal Resource Center, The University of Texas at Austin, in accordance with Institutional Animal Care and Use Committee (IACUC) Guidelines. The mice received an alfalfa free diet (2019 Tekland Global 19% Protein Extruded Rodent Diet) for 7 days prior to commencement of the study in order to reduce intestinal autofluorescence, and were maintained on this diet throughout the duration of the study. Mice were fasted for 3 hours prior to dosing. 50mg of microparticles were dosed in 200ul 5% w/v sodium bicarbonate via intragastric gavage (3 mice per sample group). Immediately after dosing, the subjects were anesthetized in an incubation chamber with 3% isoflurane. The subjects were transferred to an IVIS Spectrum (Caliper

Life Sciences) and anesthesia was maintained using 1% isoflurane during imaging. Imaging was carried out using epifluorescence with 14 filter sets for subsequent autofluorescence subtraction. After imaging, the subjects were placed back into conventional housing with food and water *ad libitum*. Mice were imaged again at 18 hours post-does under the same conditions. After 45 hours post-dose, the mice were sacrificed, imaged, then the intestines were removed for further imaging.

5.2.4. Analysis of Fluorescence Imaging Data

For the 15 minute time point, the signal-to-noise ratio was sufficiently intense enough that autofluorescence subtraction was unnecessary and the samples were analyzed with the highest contrast filter set (640nm/760nm). For all subsequent time points spectral unmixing was carried out to pull out the nanocrystal fluorescence from tissue autofluorescence using Living Image 4.0 (Caliper Life Science). For whole animal images, the following excitation/emission filter sets were used: 570/700, 605/720, 605/740, 605/760, 605/780, 605/800, 640/700, 640/720, 640/740, 640/760, 640/780, and 640/800. The samples were unmixed using a two fluorophore setting: tissue autofluorescence set to "Auto" and Fixed, nanocrystal fluorescence set to "AF750Ex", an internal spectrum standard which matched well with our nanocrystal fluorescence spectrum. Regions of Interest (ROIs) were drawn around the abdominal. Total Radiant Efficiency [$p/s\mu W^{-1}cm^2$] was reported. For intestinal images a three fluorophore setting was used to additionally subtract the stage fluorescence. The previous filter sets were used plus the addition of 570/800. Note: the D911A sample 3 was not used for analysis as the initial image showed substantial fluorescence around the mouth, relative to the

stomach, that may have been slowly ingested, thereby altering later relative fluorescence comparisons.

5.3. Results and Discussion

5.3.1. Fluorescence Retention in Mice

The microparticles encapsulating the CISS nanocrystals were orally administered to mice and imaged at various time points to track the fluorescence retention in the GI tract, which should correlate to M cell uptake. Fluorescence images of representative mice fed CISS nanocrystal loaded PLGA microparticles are shown in Figure 5.2.

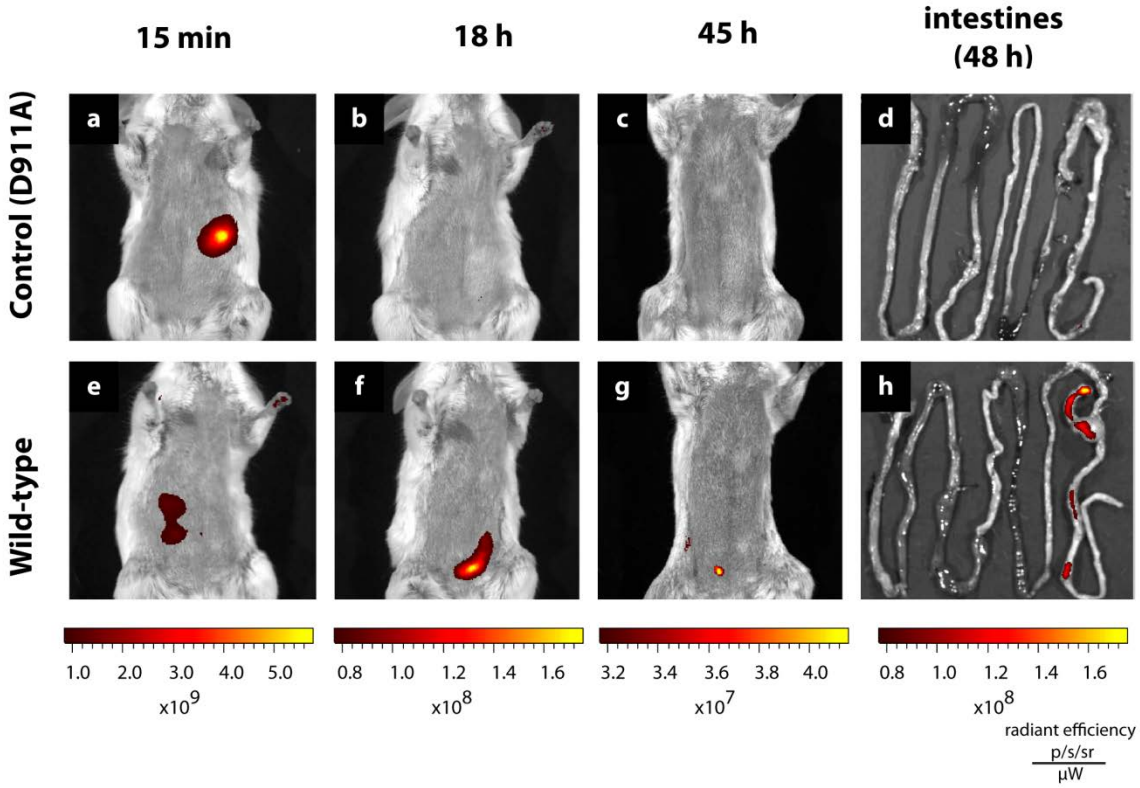

Figure 5.2. Representative images of in-vivo fluorescence measurements tracking the same subjects at 15 min (a,e), 18 h (b,f), 45h (c,g) after dosing and the intestines after dissection at 48h (d,h). Mice were administered CISS nanocrystal-loaded PLGA microparticles conjugated with either wild type invasin-MBP fusion protein (e-h) or the same protein with the D911A mutation abrogating the targeting ability (a-d).

The CISS nanocrystals were clearly able to identify the location of the microparticles in vivo. Quantitative analysis was performed by integrating the intensities over a region of interest (ROI). The relative intensities over time are shown in Figure 5.3. The ROI was

such that it encompasses the entire abdomen. For images with weaker signals (18h, 45h, intestines), the images were spectrally unmixed using Living Image 4.0 to distinguish tissue autofluorescence from nanocrystal fluorescence.

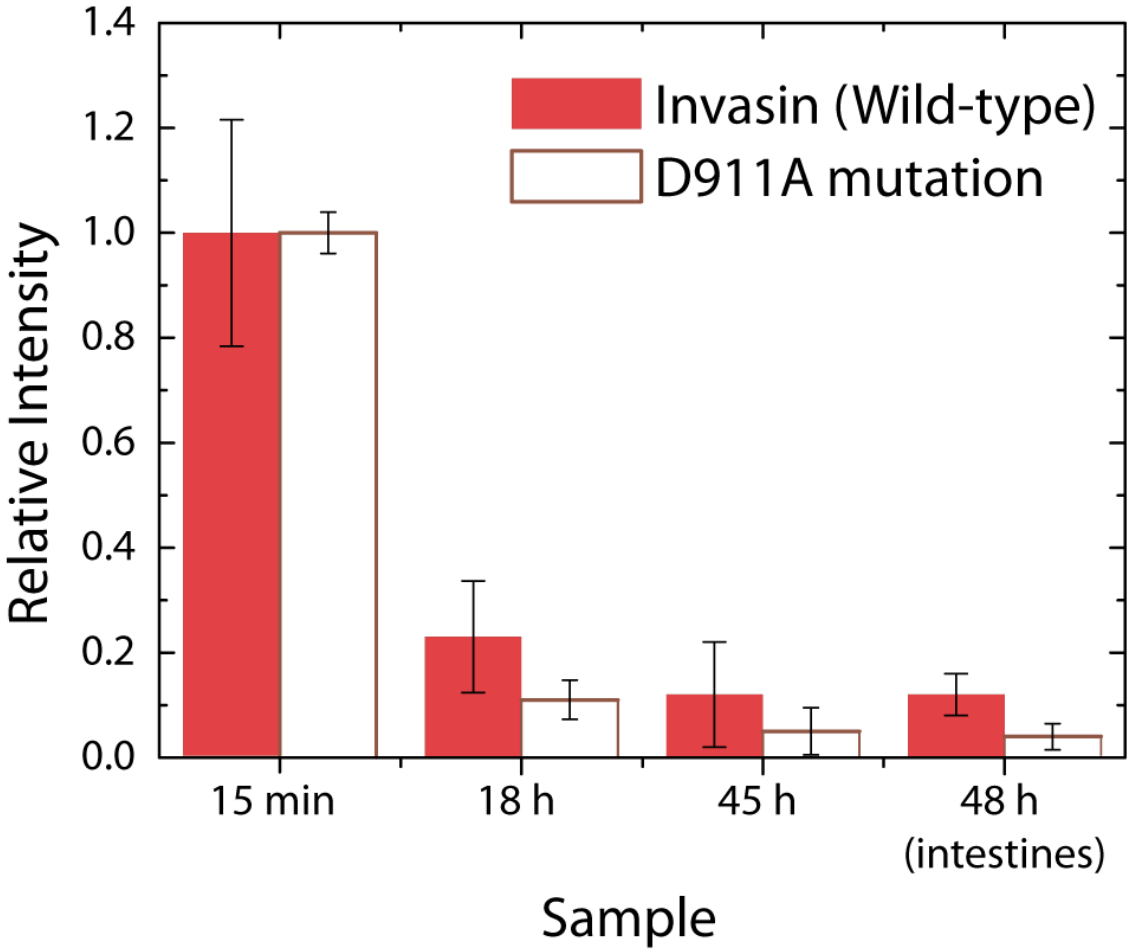

Figure 5.3: Comparison of fluorescence signal from the nanocrystals at 15 min, 18 h, 45 h in vivo, and the intestines at 48 hours post-mortem. Error bars correspond to the standard deviation of measurements of multiple mice for each experiment.

5.4. CONCLUSIONS

We have developed a simple method to synthesize quaternary quantum dots with size-dependent PL. The PL quantum yield of CISS particles was around 10% which increased to 40% after overgrowth of a ZnS shell. In addition, the synthetic method has potential to be applied to other ternary or quaternary systems, allowing for further exploration in the luminescent properties of compound semiconductor nanocrystals. These nanocrystals are attractive for biomedical imaging due to their nontoxic nature, high PL quantum yield, and PL emission that is tunable in the NIR. We demonstrate the in vivo imaging ability of the nanocrystals in deep tissue, where tissue autoflourescence is maximal and excitation light is minimal. The CISS nanocrystals hold tremendous promise as a new material as a biocompatible diagnostic agent.

5.5. REFERENCES

1. Puzzo, D. P.; Henderson, E. J.; Helander, M. G.; Wang, Z.; Ozin, G. A.; Lu, Z. *Nano Letters* **2011,** 11, (4), 1585-1590.

2. Steckel, J. S.; Coe-Sullivan, S.; Bulović, V.; Bawendi, M. G. *Advanced Materials* **2003,** 15, (21), 1862-1866.

3. Gur, I.; Fromer, N. A.; Geier, M. L.; Alivisatos, A. P. *Science* **2005,** 310, (5747), 462-5.

4. Panthani, M. G.; Akhavan, V.; Goodfellow, B.; Schmidtke, J. P.; Dunn, L.; Dodabalapur, A.; Barbara, P. F.; Korgel, B. A. *J Am Chem Soc* **2008,** 130, (49), 16770-7.

5. Pattantyus-Abraham, A. G.; Kramer, I. J.; Barkhouse, A. R.; Wang, X.; Konstantatos, G.; Debnath, R.; Levina, L.; Raabe, I.; Nazeeruddin, M. K.; Gratzel, M.; Sargent, E. H. *ACS nano* **2010,** 4, (6), 3374-80.

6. Guo, Q.; Ford, G. M.; Hillhouse, H. W.; Agrawal, R. *Nano Letters* **2009,** 9, (8), 3060-3065.

7. Michalet, X.; Pinaud, F. F.; Bentolila, L. A.; Tsay, J. M.; Doose, S.; Li, J. J.; Sundaresan, G.; Wu, A. M.; Gambhir, S. S.; Weiss, S. *Science* **2005,** 307, (5709), 538-544.

8. Medintz, I. L.; Uyeda, H. T.; Goldman, E. R.; Mattoussi, H. *Nature materials* **2005,** 4, (6), 435-446.

9. Hessel, C. M.; Rasch, M. R.; Hueso, J. L.; Goodfellow, B. W.; Akhavan, V. A.; Puvanakrishnan, P.; Tunnel, J. W.; Korgel, B. A. *Small* **2010,** 6, (18), 2026-34.

10. Farokhzad, O. C.; Langer, R. *Advanced Drug Delivery Reviews* **2006,** 58, (14), 1456-1459.

11. Hessel, C. M.; V, P. P.; Rasch, M.; Panthani, M. G.; Koo, B.; Tunnell, J. W.; Korgel, B. A. *Nano Lett* **2011,** 11, (6), 2560-6.

12. Clark, M. A.; Hirst, B. H.; Jepson, M. A. *Infect. Immun.* **1998,** 66, (3), 1237-1243.

13. Hussain, N.; Florence, A. T. *Pharmaceutical Research* **1998,** 15, (1), 153-156.

14. Tyrer, P. C.; Ruth Foxwell, A.; Kyd, J. M.; Otczyk, D. C.; Cripps, A. W. *Vaccine* **2007,** 25, (16), 3204-3209.

15. Leong, J. M.; Morrissey, P. E.; Marra, A.; Isberg, R. R. *The EMBO Journal* **1995,** 14, (3), 422-431.

16. Liu, W.; Choi, H. S.; Zimmer, J. P.; Tanaka, E.; Frangioni, J. V.; Bawendi, M. *J Am Chem Soc* **2007,** 129, (47), 14530-1.

17. Soltesz, E. G.; Kim, S.; Kim, S. W.; Laurence, R. G.; De Grand, A. M.; Parungo, C. P.; Cohn, L. H.; Bawendi, M. G.; Frangioni, J. V. *Annals of surgical oncology* **2006,** 13, (3), 386-96.

18. Stroh, M.; Zimmer, J. P.; Duda, D. G.; Levchenko, T. S.; Cohen, K. S.; Brown, E. B.; Scadden, D. T.; Torchilin, V. P.; Bawendi, M. G.; Fukumura, D.; Jain, R. K. *Nature medicine* **2005,** 11, (6), 678-82.

19. Allen, P. M.; Liu, W.; Chauhan, V. P.; Lee, J.; Ting, A. Y.; Fukumura, D.; Jain, R. K.; Bawendi, M. G. *J Am Chem Soc* **2010,** 132, (2), 470-1.

20. Li, L.; Daou, T. J.; Texier, I.; Kim Chi, T. T.; Liem, N. Q.; Reiss, P. *Chemistry of Materials* **2009,** 21, (12), 2422-2429.

Chapter 6: Optical Properties of Silicon Nanocrystals

6.1. INTRODUCTION

As an indirect band gap semiconductor, bulk Si is a poor emitter and absorber of light.[1] Silicon solar cells require hundreds of microns to absorb all the incoming light, while photoluminescence of Si is only typically observed at cryogenic temperatures. Indirect transitions must occur with assistance from a phonon. Nanoscale silicon has demonstrated the ability to emit light with relatively high efficiency.[2] Red emission was observed in electrochemically etched porous silicon by Canham and coworkers in the early 1990's,[3, 4] which sparked an interest in luminescenct silicon nanostructures. Si quantum dots can be very bright light emitters. Alkyl-passivated colloidal Si nanocrystals have been reported with visible wavelength photoluminescence quantum yields of up to 60%.[2] LEDs have been made with Si nanocrystals to achieve (with ITO:PEDOT:TPD:Si NCs:Alq3:LiF/Al structure) power efficiencies (EQEs) of 8.6%—the highest of any ncLED to date.[5] These devices however had a spectral dependence on device current, which was attributed to nanocrystal polydispersity.

6.2. EXPERIMENTAL METHODS

6.2.1. Decomposition of hydrogen silsesquioxane to oxide-embedded nanocrystals

Si nanocrystals were prepared using a method similar to that described by Hessel and coworkers.[6] Si nanocrystals are first obtained by thermal decomposition of hydrogen

silsesquioxane (HSQ). HSQ is placed in a quartz crucible and heated under a flow of 90% Ar/10% H_2 to a temperature between 1100 and 1400°C, depending on the desired nanocrystal size. The sample is held at the temperature for 1 hour before allowing the furnace to cool to room temperature. A brown/black glassy product is obtained. This product is ground for 20 min in an agate mortar and pestle then further pulverized to ~200 nm by shaking in a wrist-action shaker for 9 hr with 30 g of 3 mm borosilicate glass beads. Mechanical reduction of the oxide-embedded Si nanocrystal grain size is essential for uniform etching of the oxide matrix.

6.2.3. Etching of Oxide matrix

100 – 500 mg of the ~200 nm powder of oxide-embedded Si nanocrystals is suspended in a solution of 13 mL of 48% HF and 2 mL of 25% HCl in the dark for 6 hr. This procedure etches the oxide and yields hydride-terminated Si nanocrystals. The nanocrystals are isolated from the HF solution by centrifugation at 9000 rpm for 3 min.

6.2.5. Hydrosilylation of H-terminated Si Nanocrystals

After centrifugation, the supernatant is discarded and the light brown precipitate is rinsed twice with excess ethanol, once with excess toluene, and finally dispersed in a 4:1 ratio of 1-dodecene and 1-octadecene. The resulting brown, turbid dispersion is transferred to a 3 neck round bottom flask and degassed using freeze-pump-thaw cycles on a Schlenk line. The dispersion is heated at 190°C overnight. After about 30 min of heating, the turbid brown dispersion begins to turn into an optically clear yellow-orange dispersion. The alkene-passivated Si nanocrystals are washed three times by

precipitation using acetone as an antisolvent, and dispersed in a minimal amount of toluene. Methanol/chloroform was also sometimes used as an antisolvent/solvent pair. The concentrated nanocrystal dispersions are dried at the bottom of a round bottom flask, then heated under vacuum for 24 hr at 200°C to remove excess ligand. The nanocrystals are finally dispersed in toluene for subsequent characterization. The mass yield of ligand stabilized Si nanocrystals is about 10% with respect to the oxide-embedded Si nanocrystal powder.

6.3. CHARACTERIZATION OF ORGANIC-PASSIVATED SI NANOCRYSTALS

6.3.1. X-Ray Diffraction

X-ray diffraction (XRD) was performed on a Rigaku R-Axis Spider diffractometer with an image plate detector using CuKα radiation (λ = 1.5418Å) and a graphite monochromator. The instrument was controlled using Rapid/XRD diffractometer control software (Version 2.3.8, Rigaku Americas Corporation, The Woodlands, TX). 2DP Spider software (Version 1.0, Rigaku Americas Corporation, The Woodlands, TX) was used to integrate the two dimensional image into a one dimensional pattern. A blank was subtracted to reduce background signal. XRD samples were prepared by scraping a small amount (≤ 1mg) of dried Si nanocrystals and mounting the mixture on a Hampton Research Cryoloop. A drop of mineral oil was sometimes used to help adhere the Si NC powder to the holder. XRD patterns were collected for ~15 min.

6.3.1. Transmission Electron Microscopy of Si Nanocrystals

Bright field and high angle annular dark field STEM images were acquired digitally using a JEOL model JEM-ARM200F operated at 120 kV. STEM samples were prepared by drop coating a 3 μL aliquot of 0.1 mg graphene in 1 mL of ethanol onto a lacey carbon grid (lacey carbon coated copper, Electron Microscopy Sciences), and allowed to dry for 1 hr. A 5 μL aliquot of a very dilute Si nanocrystal dispersion was then drop-coated onto the graphene coated grid and heated at 200°C for 8 hr under a dynamic flow of N_2.

6.3.1. Photoluminescence of Ligand-passivated Si Nanocrystals

Optical absorbance spectroscopy was performed at room temperature on a Cary 500 UV-vis-NIR spectrophotometer using a quartz cuvette with a 10 mm optical path length. Photoluminescence (PL) and photoluminescence excitation (PLE) spectra were acquired on a Fluorolog-3 spectrophotometer (Horiba Jobin Yvon) using a monochromated 450 W xenon lamp light source with an InGaAs photomultiplier tube for visible detection and a Hamamatsu H10330-45 detector for NIR detection. The visible detector was cooled by a circulating cooler and thermoelectric cooler, while the NIR detector was cooled by a thermoelectric cooler alone. A reference silicon photodiode was used to adjust for intensity differences in the lamp spectrum for PLE measurements. The PL quantum yield (QY) was determined by comparing the integrated photon count of nanocrystal samples to IR-26, a NIR emitting dye with a quantum yield of 0.05%. Although this dye is not ideal because it has a relatively low quantum yield of only

0.05%, there are very few NIR-emitting dyes available. The quantum yield (QY) was determined by comparing the integrated photon count of the nanocrystal sample to IR-26, a near infrared dye with a QY = 0.05%. The QY was calculated by first obtaining the photon count, *P*, of the emission spectrum using

$$P = \int \frac{I}{E} dE \tag{1}$$

Where *I* is the PL intensity and *E* is the photon energy in units of eV. The QY of the Si nanocrystals, QY_{NC}, is calculated by the relationship

$$QY_{NC} = QY_{ref} \frac{A_{ref}}{A_{NC}} \frac{P_{NC}}{P_{ref}} \frac{n_{NC}}{n_{ref}} \tag{2}$$

where the subscripts *ref* and *NC* refer to values associated with IR-26 and the Si nanocrystals, respectively, *A* is the absorbance at the PL excitation wavelength, *P* is the photon count, n_{NC} *and* n_{ref} *are* the refractive indexes of the solvents; toluene (n_{NC} = 1.497) for and chloroform (n_{ref} = 1.446).

6.4 Results and Discussion

6.4.1. X-ray diffraction of Si Nanocrystals

Figure 4 shows XRD data for alkene-passivated Si nanocrystals produced at various HSQ decomposition temperatures. All of the XRD patterns index to diamond cubic Si, with significant size-dependent peak broadening. The broad reflection at 2*q* of approximately 20^{o} results from crystallized organic ligands.

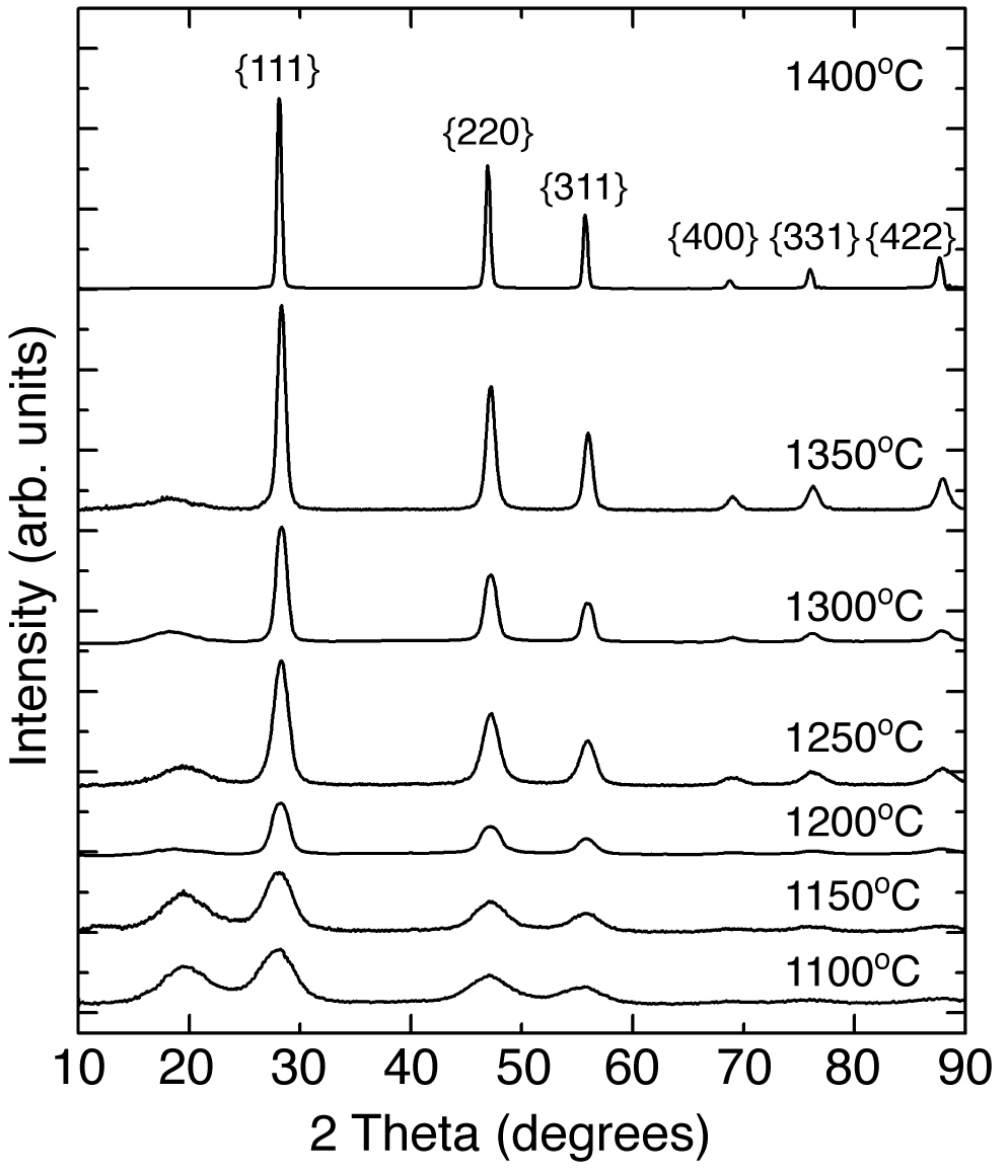

Figure 6.1. XRD of ligand-passivated Si nanocrystals. The diffraction patterns correspond to diamond cubic Si (JCPDS no. 027-1402; a = b = c = 5.43 Å).

6.4.3. Transmission Electron Microscopy

Figure 6.2 shows Cs-corrected STEM images of Si nanocrystals on a graphene support. Figure 6.2(a) shows a nanocrystal in bright-field STEM mode. The nanocrystal is imaged down the [110] done axis. Lattice fringes can clearly be seen, and measurement of the (100) planes is 5.4Å, which matches bulk Si.

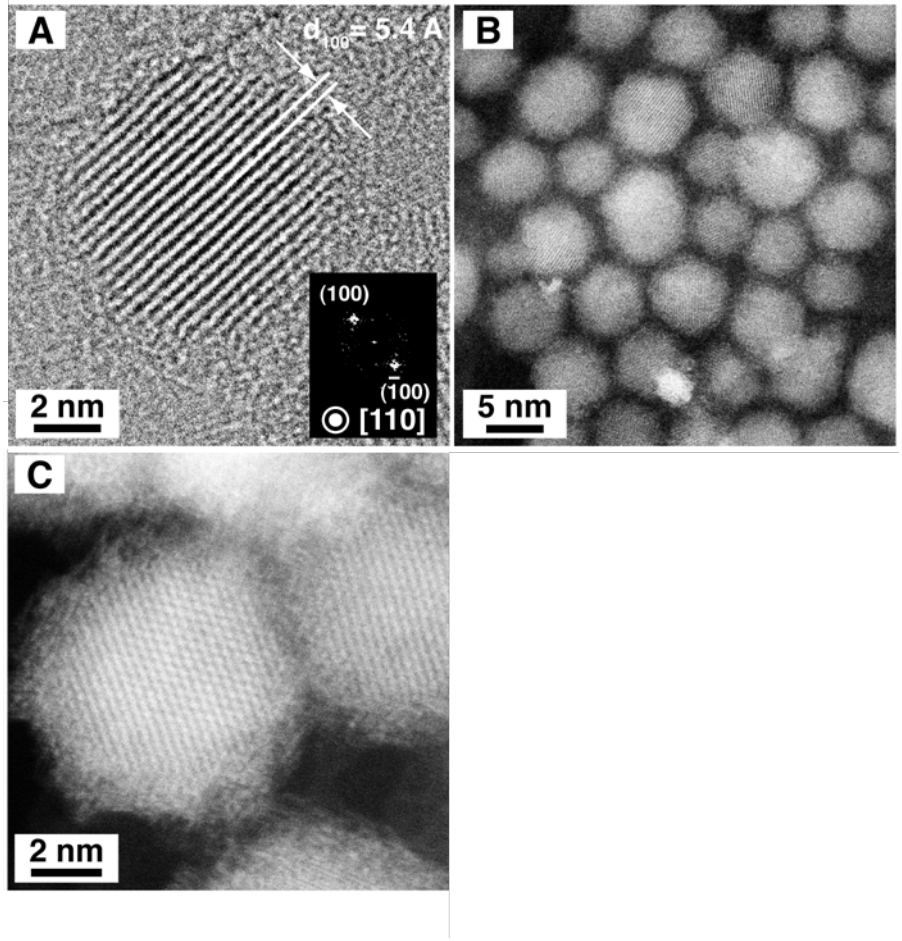

Figure 6.2. (a) Bright-field and (b,c) dark-field STEM images of alkene-passivated Si nanocrystals supported on few-layer graphene.

6.4.3. Photoluminescence of Si Nanocrystals

Figure 6.3 shows room temperature PL and PLE spectra of octadecene/dodecene-stabilized Si nanocrystals. As summarized in Table 2, the PL emission peaks range from approximately 720 nm (3 nm diameter) out to 1060 nm (12 nm diameter), near the bulk band gap of Si, with quantum yields of 8% for the smallest (3 nm diameter) nanocrystals decreasing with increasing diameter down to 0.4% for the 12 nm nanocrystals. A decrease in PL QY with increasing size has also been observed from other types of nanocrystals as well. For the largest light-emitting nanocrystals, the line-shape of the PL peak becomes non-Gaussian with a noticeable drop in intensity at ~1150 nm, which may be the fundamental long wavelength limit for the emission from alkyl-passivated Si nanocrystals. Nanocrystals larger than about 12 nm did not have measurable PL. Table 6.1 shows the PL maxima quantum yield as a function of heating temperature. Note also that the QY of the Si nanocrystal PL is relatively high compared to organic fluorophores, as few molecular dyes exist that emit in this wavelength range.[34, 51] This is important with respect to biological imaging applications in which biocompatible contrast agents with NIR emission are desirable.

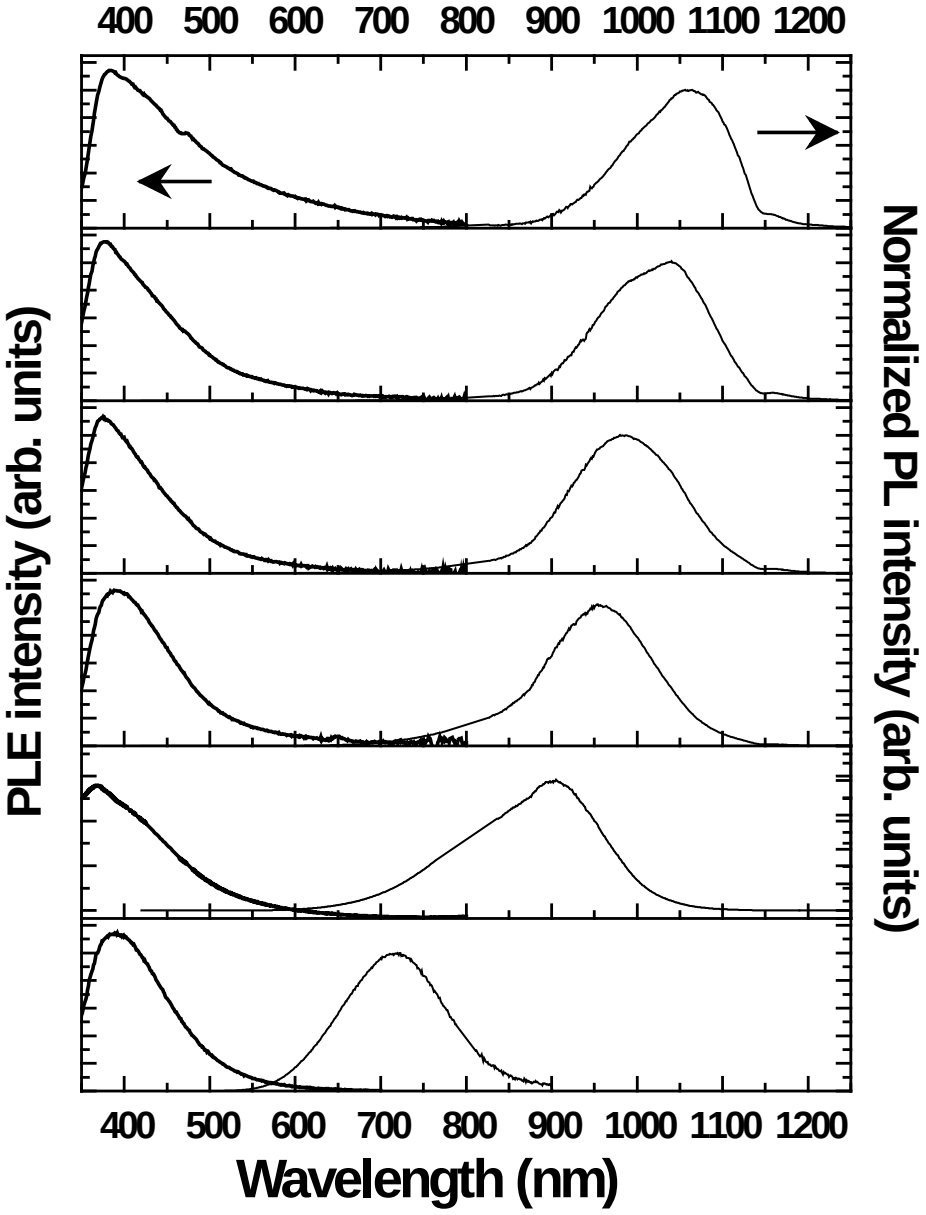
400 500 600 700 800 900 1000 1100 1200
PLE intensity (arb. units)
Normalized PL intensity (arb. units)
400 500 600 700 800 900 1000 1100 1200
Wavelength (nm)

Figure 6.3. Room temperature PL (λexc=400 nm) and PLE (measured at emission maximum) spectroscopy of alkane-stabilized Si nanocrystals dispersed in toluene. The spectra have been normalized in intensity to demonstrate the peak shift with processing temperature. For PLE spectra a reference silicon photodiode was used to adjust for intensity differences in the lamp spectrum for the measurements.

Table 6.1. PL Maximum and quantum yield as a function of nanocrystal size

Reaction Temperature (°C)	Particle Diameter (nm)	PL Maximum (nm)	Quantum Yield (%)
	SAXS	λ_{ex} = 420 nm	via IR-26
1100	2.7±0.6	718	8
1150	2.9±1.0	903	5
1200	5.0±1.3	957	3
1250	6.0±1.7	986	1
1300	8.8±1.8	1035	0.6
1350	11.8±2.1	1064	0.4

6.5. CONCLUSIONS

The optical data reported here are relevant to studies using luminescent Si nanocrystals as contrast agents for bioimaging. Si nanomaterials have received attention for applicability in medicine because they are biocompatible and biodegradable, which is

a significant advantage over heavy metal containing quantum dots such as CdSe.[7-9] Si nanocrystals exhibit size-tunable emission with red to NIR wavelength, but there is a large wavelength difference between the emitting wavelengths and the wavelengths needed for excitation with strong emission. This presents a major challenge. For example, the region of strong light absorption for high brightness emission in the case of small (2-3 nm) Si nanocrystals occurs below about 500 nm, which overlaps with the absorption of water, hemoglobin and oxyhemoglobin in human tissue.[10] This limits the applicability of small Si nanocrystals for single photon bioimaging applications. Our data show that this limitation can be overcome by shifting the absorption to the red with increased Si nanocrystal size. The PL quantum yield decreases slightly as the nanocrystal size increases, however it remains relatively high compared to other NIR-emitters.

6.6. REFERENCES

1. Chelikowsky, J. R.; Cohen, M. L. *Physical Review B* **1974,** 10, (12), 5095-5107.

2. Jurbergs, D.; Rogojina, E.; Mangolini, L.; Kortshagen, U. *Appl. Phys. Lett.* **2006,** 88, (23), 233116.

3. Canham, L. T. *Applied Physics Letters* **1990,** 57, (10).

4. Cullis, A. G.; Canham, L. T. *Nature* **1991,** 353, (6342), 335-338.

5. Cheng, K.-Y.; Anthony, R.; Kortshagen, U. R.; Holmes, R. J. *Nano Letters* **2011,** 11, (5), 1952-1956.

6. Hessel, C. M.; Henderson, E. J.; Veinot, J. G. C. *Chemistry of Materials* **2006,** 18, (26), 6139-6146.

7. Liu, W.; Choi, H. S.; Zimmer, J. P.; Tanaka, E.; Frangioni, J. V.; Bawendi, M. *J Am Chem Soc* **2007,** 129, (47), 14530-1.

8. Buzea, C. *Biointerphases* **2007,** 2, (4), MR17.

9. Deka, S.; Quarta, A.; Lupo, M. G.; Falqui, A.; Boninelli, S.; Giannini, C.; Morello, G.; De Giorgi, M.; Lanzani, G.; Spinella, C.; Cingolani, R.; Pellegrino, T.; Manna, L. *J Am Chem Soc* **2009,** 131, (8), 2948-58.

10. Weissleder, R. *Nat Biotech* **2001,** 19, (4), 316-317.

Chapter 7: Graphene as a Support for Transmission Electron Microscopy

7.1. INTRODUCTION

Transmission electron microscopy (TEM) is one of the most widely used and effective tools for evaluating nanomaterials. It provides direct visualization of nanocrystals with nanometer-scale resolution, providing a measure of size, shape, and crystal structure. TEM can reveal the presence of defects and collective interactions. For TEM, nanocrystals are commonly imaged on thin (usually ~20 nm) amorphous carbon supports. In TEM, imaging contrast arises from electron scattering when interacting with the sample, which is dependent on the sample thickness, atomic number, and crystallographic orientation. For very small, amorphous, and low atomic number nanomaterials (such as silicon) the carbon substrate can substantially obscure the TEM images due to random scattering of the transmitted electrons. For mechanical stability, an amorphous carbon film needs to be about 20 nm thick. Graphene on the other hand, is composed of a single atomic layer of carbon atoms that is only 3.4 Å thick.[1] It is mechanically stable because of the uninterrupted 2D network of sp^2 bonded carbon atoms. Graphene is an order of magnitude thinner than the thinnest commercially available amorphous carbon films. In addition to its mechanical stability, graphene is electrically and thermally conductive, making it a useful TEM support that helps dissipate electrostatic charging and heating of the samples under the electron beam. The carbon atoms in graphene are also highly ordered, which can enable background subtraction of acquired images with little information loss. Many methods now exist for

preparing graphene,[2-4] making it readily available and economical to use. For this reason, graphene has been proposed by multiple groups as a potential support for metal nanocrystals for many applications, including fuel cells and catalysis.[5-7] Several research groups have studied the structure of graphene in detail by TEM[8-12] and STEM,[2, 13] and have even been able to image the presence and dynamics of adatoms and adsorbed molecular species on graphene.[11] Graphene has also been used as a support for imaging nanoparticles for unprecedented clarity. For instance, Lee and coworkers imaged adsorbed citrate molecules on gold nanocrystals using graphene supports.[14] McBride and coworkers produced lattice-resolved images of sub-2nm CdSe nanocrystals and highly detailed electron energy loss spectroscopy maps of $CuInSe_2$ nanocrystals on graphene.[15] In fact, the organic ligand shell was even visible with the near absence of the carbon background.[15] Due to the high thermal and electrical stability of graphene, it has been used as a substrate for in-situ high-temperature electrical measurements probe and monitor the effects of adsorbates on the conductivity of graphene.[16] TEM has been used to image cobalt nanocrystals on graphene[17] and nanocrystals on boron nitride,[18] another ultrathin low atomic number material. Here, we report TEM and STEM images of hydrogen-terminated (unpassivated) and organic monolayer-passivated silicon nanocrystals using graphene as an imaging support. TEM characterization of nanomaterials is critical to understanding the dependence of size, shape, and defects to the optical and electronic properties of it.

7.2. EXPERIMENTAL

7.2.1. Nanocrystal synthesis and preparation

Organic ligand-stabilized nanocrystals were synthesized following procedures developed by Hessel, et al. [19, 20] Hydrogen silsesquioxane (HSQ) is heated to temperatures between 1100 and 1400°C under inert atmosphere to produce oxide-embedded Si nanocrystals. The nanocrystals are liberated from the SiO_2 matrix by etching with a mixture of 13 mL of 48% hydrofluoric acid and 2 mL of 25% hydrochloric acid for 6 hours in the dark. The product is centrifuged at 8000 rpm for 3 min. to obtain a pellet of nanocrystals and then three cycles of centrifugation/redispersion are carried out: twice in ethanol, once in toluene to remove excess HF and other impurities. The nanocrystals are redispersed and refluxed in a 4:1 dodecene:octadecene mixture at 190°C for 8 hours. This procedure yields alkyl-passivated Si nanocrystals. The nanocrystals are precipitated by adding ethanol or acetone and centrifugation at 8000 rpm for 3 min. to obtain a pellet of nanocrystals. The alkene-capped nanocrystals were subjected to several iterations of redispersion in toluene and precipitation with ethanol or acetone to remove excess alkene. The final dispersion in toluene was centrifuged to precipitate any poorly-capped particles and agglomerates. This dispersion was dried at the bottom of a round bottom flask, purged with N_2, and heated to 200 C under vacuum (~150 mTorr) overnight to remove excess alkenes. This dispersion was then redipsersed in a small amount of toluene.

7.2.2 TEM Sample Preparation

TEM substrates were prepared by drop casting graphene dispersed in ethanol onto a copper TEM grid with a lacey carbon support (Electron Microscopy Sciences). Graphene was either purchased from Electron Microscopy Sciences (0.1 mg/mL in ethanol) or synthesized by hydrazine reduction of graphene oxide.[21, 22] Si nanocrystals were deposited on the graphene TEM substrates by drop casting a dilute (< 1 mg/ml) dispersion of Si nanocrystals in ethanol (unpassivated) or toluene (alkene-passivated). After drying in air for at least one hour, the TEM grids were placed in a tube furnace and heated to 200°C overnight under forming gas (7% H_2, 93% N_2) to remove excess alkene, solvent, and other organics. This post-deposition heating was not performed on the unpassivated Si nanocrystals.

7.3. High-resolution Transmission Electron Microscopy (HRTEM) of Si Nanocrystals

7.3.1. Conventional HRTEM and Scanning Transmission Electron Microscopy (STEM)

HRTEM image were acquired using a JEOL 2010F with a 200 kV accelerating voltage. Aberration (Cs) corrected STEM images were acquired with a JEOL JEM-ARM200F microscope operating at 80 or 120 kV. Bright field images were acquired using an in-line detector, and dark field images were acquired with a high-angle annular dark field (HAADF) detector. The graphene TEM supports were prepared by drop-casting graphene from ethanol dispersions onto lacey carbon-coated copper mesh TEM grids. The colloidal Si nanocrystals were synthesized following the procedures

developed by Hessel, et al.[19, 20] The clearest TEM images were obtained by drop-casting the alkene-passivated nanocrystals on the graphene-coated TEM grids, allowing them to dry in air for one hour and then placing them in a tube furnace at 200°C overnight under forming gas (7% H_2, 93% N_2) to remove excess alkene, solvent, and organic contamination. TEM grids with unpassivated Si nanocrystals did not undergo this post-deposition heating.

7.4. Results and Discussion

7.4.1. Bright- and Dark-field STEM of Si Nanocrystals on Graphene

Figure 1 shows bright and dark-field STEM images obtained simultaneously using in-line and high-angle annular dark field (HAADF) detectors on a JEOL JEM ARM200F microscope operated at 120 or 80 kV accelerating voltage. The graphene tends to form agglomerates of wrinkled and curled sheets as in the low magnification images in Figures 1A and 1B. The areas with the lowest image contrast correspond to extended regions of graphene that yield the clearest images of Si nanocrystals. At higher magnification, as in Figure 1C and 1D, the Si nanocrystals are clearly visible. Lattice resolution is observed in both the bright-field and dark-field STEM images.

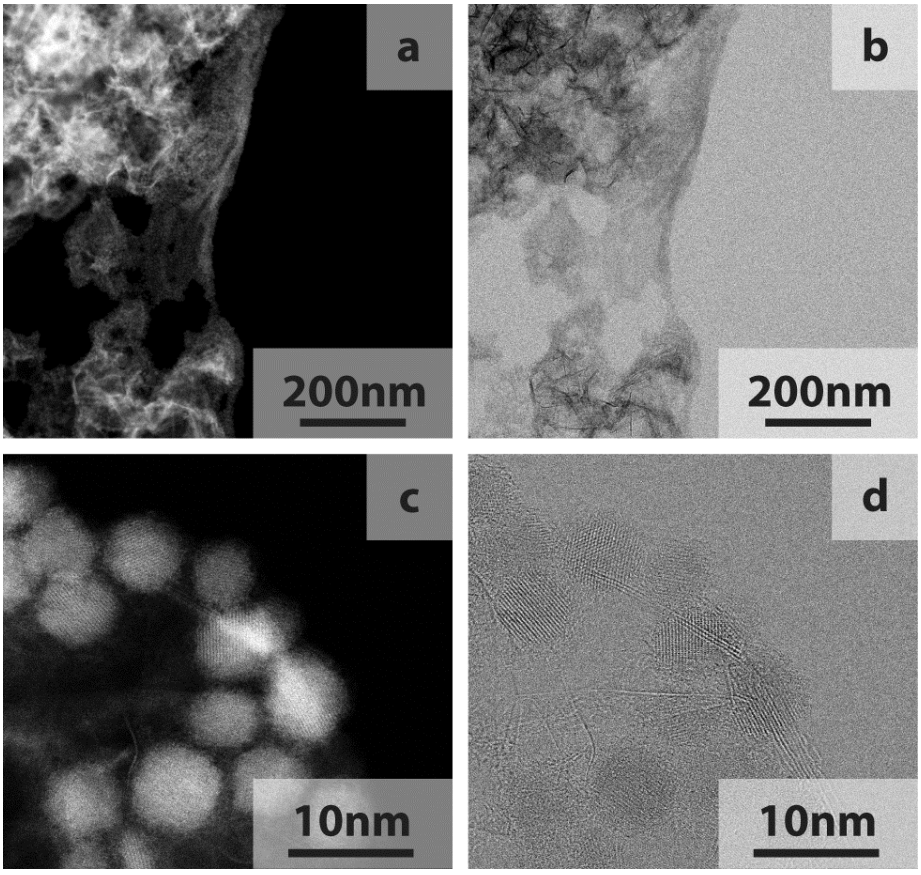

Figure 7.1. Low magnification (a,c) dark-field and (b,d) bright field spherical aberration (Cs) corrected STEM images obtained using a JEOL JEM ARM200F microscope operated at 120 kV accelerating voltage. The bright field and dark field images were obtained simultaneously using in-line and high-angle annular dark field (HAADF) detectors.

7.4.2. Comparison of Graphene and Amorphous Carbon Substrates using Conventional HRTEM

Single-layer graphene can degrade rapidly under an electron beam at accelerating voltages much greater than 100 kV.[11, 23] However, stable imaging of Si nanocrystals was possible at 200 kV accelerating voltage when the nanocrystals were supported on few-layer graphene. Although single-layer graphene provides the ultimate imaging resolution, few-layer graphene was also quite good. Figure 2 shows a comparison

between TEM images of alkene-passivated Si nanocrystals on few-layer graphene and a typical amorphous carbon support obtained using a JEOL 2010F TEM operated at 200 kV. The image of the Si nanocrystal on few-layer graphene is much clearer. The mottled background of the amorphous carbon substrate leads to significant variation in the image contrast and an unclear particle edge; whereas, the image contrast is much more uniform across the entire particle on the graphene support. Nonetheless, the imaging resolution and contrast was found to be much better using lower accelerating voltage (~100 kV) and single-layer graphene as a support. In few layer graphene, the carbon lattice cannot be resolved and the support is thick enough to obscure the image, making it difficult to resolve nanocrystals smaller than about 4 nm in diameter.

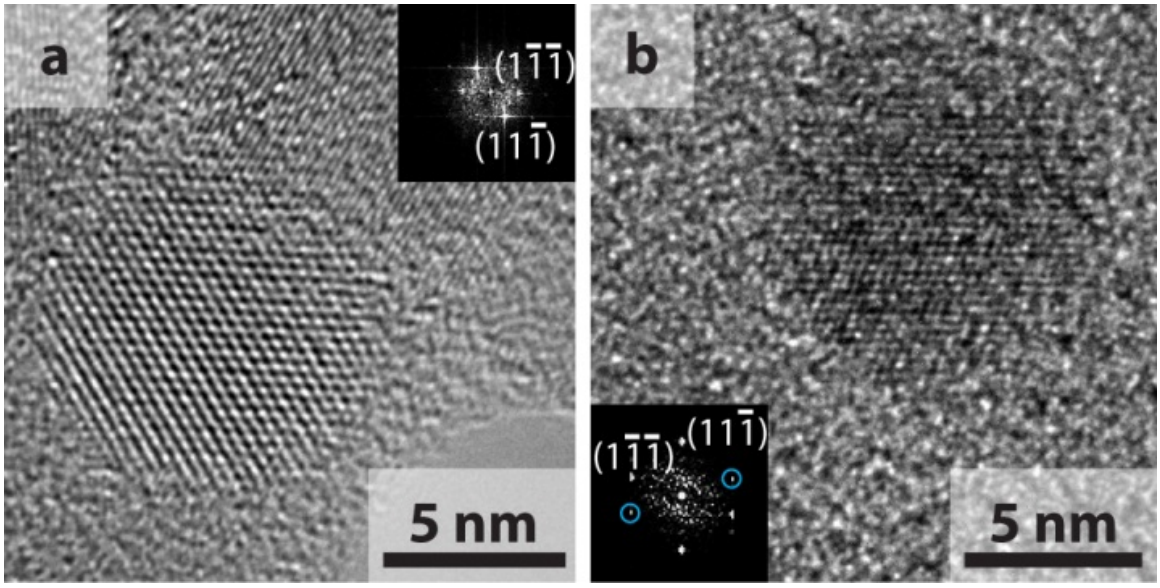

Figure 7.2. TEM images acquired with a JEOL 2010F microscope operated at 200 kV of alkene-passivated Si nanocrystals on (a) few-layer graphene and (b) standard amorphous carbon film. Both nanocrystals are imaged with similar crystallographic orientation down the Si [110] zone axis. (Insets) Fast Fourier transforms (FFTs) of the TEM images.

7.4.3. Comparison of Graphene and Amorphous Carbon Substrates using Aberration-corrected STEM

Figure 3 shows bright and dark-field STEM images of Si nanocrystals acquired at 120 kV on single-layer graphene supports compared to amorphous carbon. Line profiles of the image contrast across each nanocrystal show that the nanocrystals imaged on graphene have much higher resolution. When imaged on graphene, the contrast in the bright field STEM images is highly dependent on the nanocrystal orientation, whereas the contrast in dark field depends primarily on the atomic number of the material. The Si nanocrystals imaged by dark field STEM on amorphous carbon (Figure 3e) have higher

imaging contrast than the nanocrystals imaged in bright field TEM due to the sensitivity on Z-contrast. However, the precise location of the edges of the Si nanocrystals is difficult to determine when imaged on the amorphous carbon substrate in either bright or dark field.

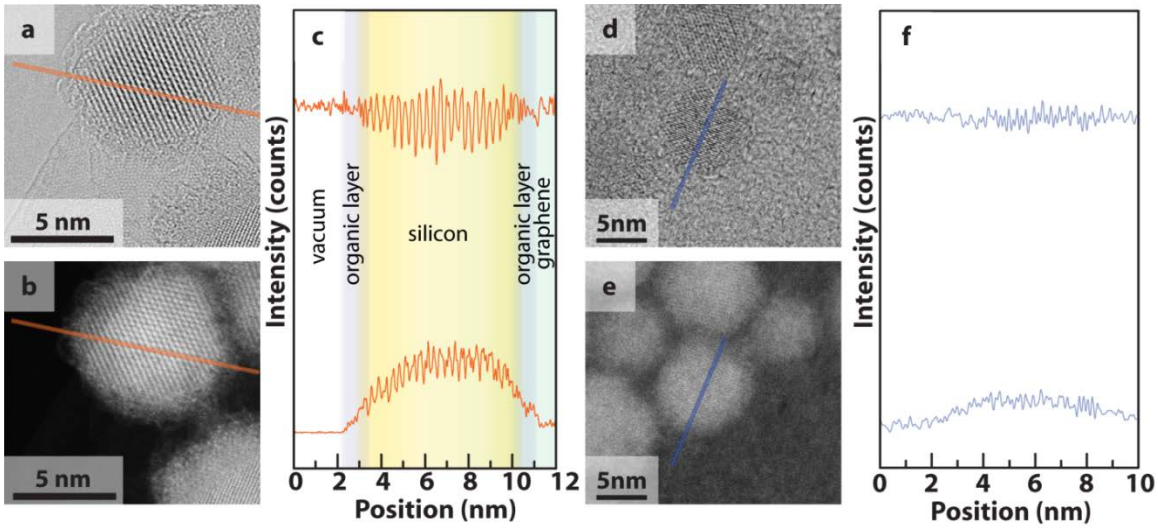

Figure 7.3. Comparison of STEM images of Si nanocrystals on graphene and amorphous carbon supports. A silicon nanocrystal supported on graphene imaged in (a) bright field and (b) dark field and (c) intensity profiles (top: bright field, bottom: dark field) obtained along the orange line. A group of silicon nanocrystals supported on amorphous carbon in (d) bright field and (e) dark field, and (f) intensity profiles (top: bright field, bottom: dark field) obtained along the blue lines.

In Figure 7.3(a), there is only a very subtle difference in image contrast between the graphene support and vacuum. In fact, there is more difference in contrast between the graphene support and the capping ligand shell.

7.4.4. Imaging of the Inorganic-Organic Interface

Using graphene as a support and an aberration-corrected STEM, detailed images of the inorganic-organic interface with near atomic resolution of the capping ligand layers could be obtained. Figure 4 shows a variety of high resolution dark and bright field STEM images of Si nanocrystals. On flat areas of few-layer graphene, the aliphatic chains are visible in both bright- and dark-field. There has been a report of the nanocrystal-organic interface of citrate-capped Au nanocrystals imaged by high resolution aberration-corrected TEM on graphene.[14] However, to our knowledge this is the first report of electron microscopy imaging of the hydrocarbon chains typically used as capping ligands for steric stabilization of hydrophobic nanocrystals.

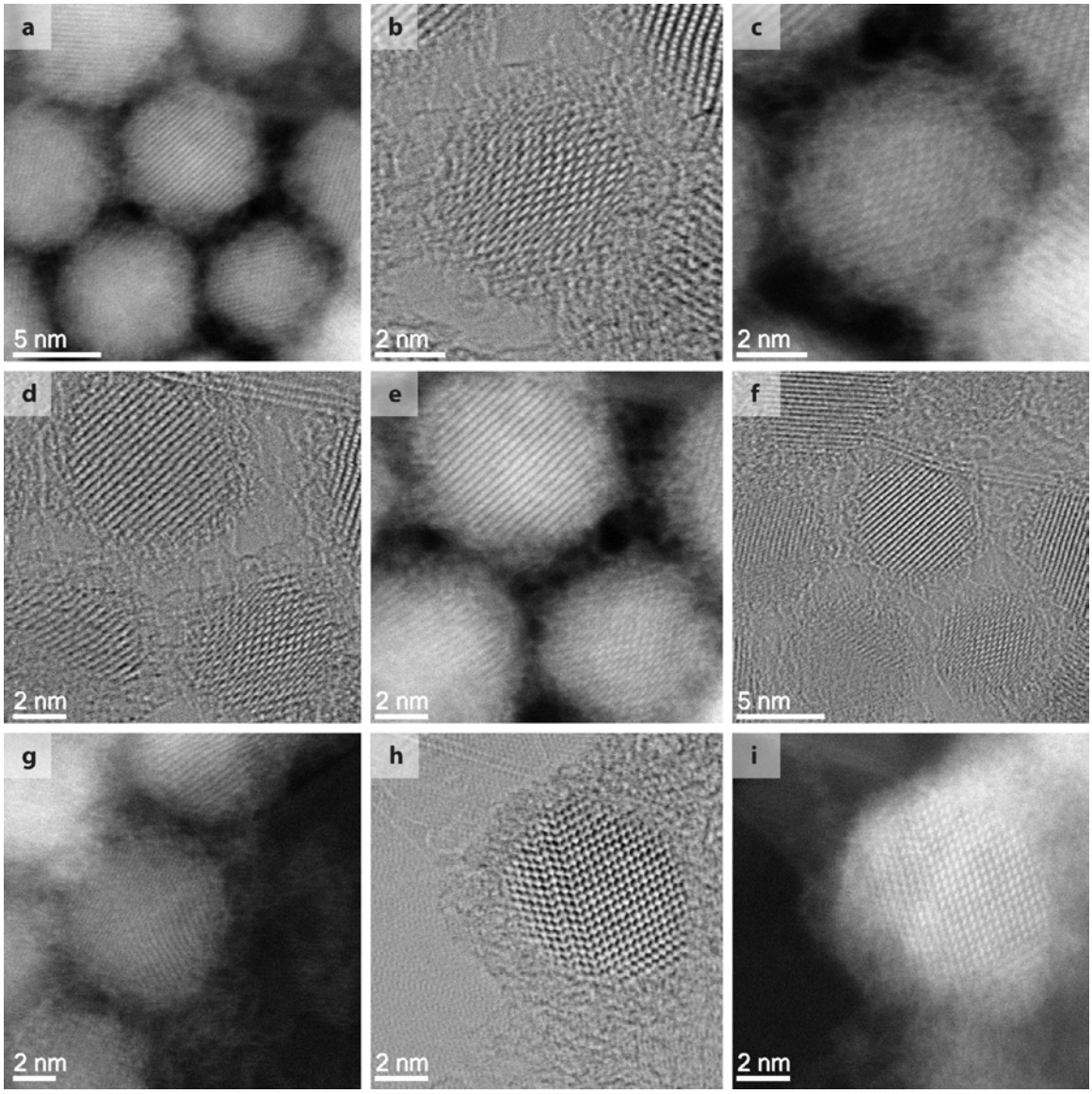

Figure 7.4. Dark field and Bright field STEM images of alkene-passivated silicon nanocrystals acquired with a JEOL JEM-ARM200F operating at 80 kV. The nanocrystal in (h) and (i) is enveloped in excess organic.

In some areas, residual hydrocarbon is present (as in Figures 7.4(h) and (i)). This residual organic material has a distinct, relatively dense appearance in both the bright and dark-field images. When excess organic is not present, the organic capping ligand layer looks to be quite diffuse. Individual molecules are visible and there is significant void space between neighboring nanocrystals. In contrast, when nanocrystals are found suspended over vacuum, the ligand layer appears to be denser, bridging between nanocrystals, as in Figure 5. It appears that the interaction between the ligands and the underlying substrate are stabilizing and limit the lateral interactions between neighboring nanocrystals and their capping ligands. When the nanocrystals were observed on stepped graphene or over vacuum, like the particle in Figure 3a-b, the ligands appear to curl and interdigitate, interacting much more strongly.

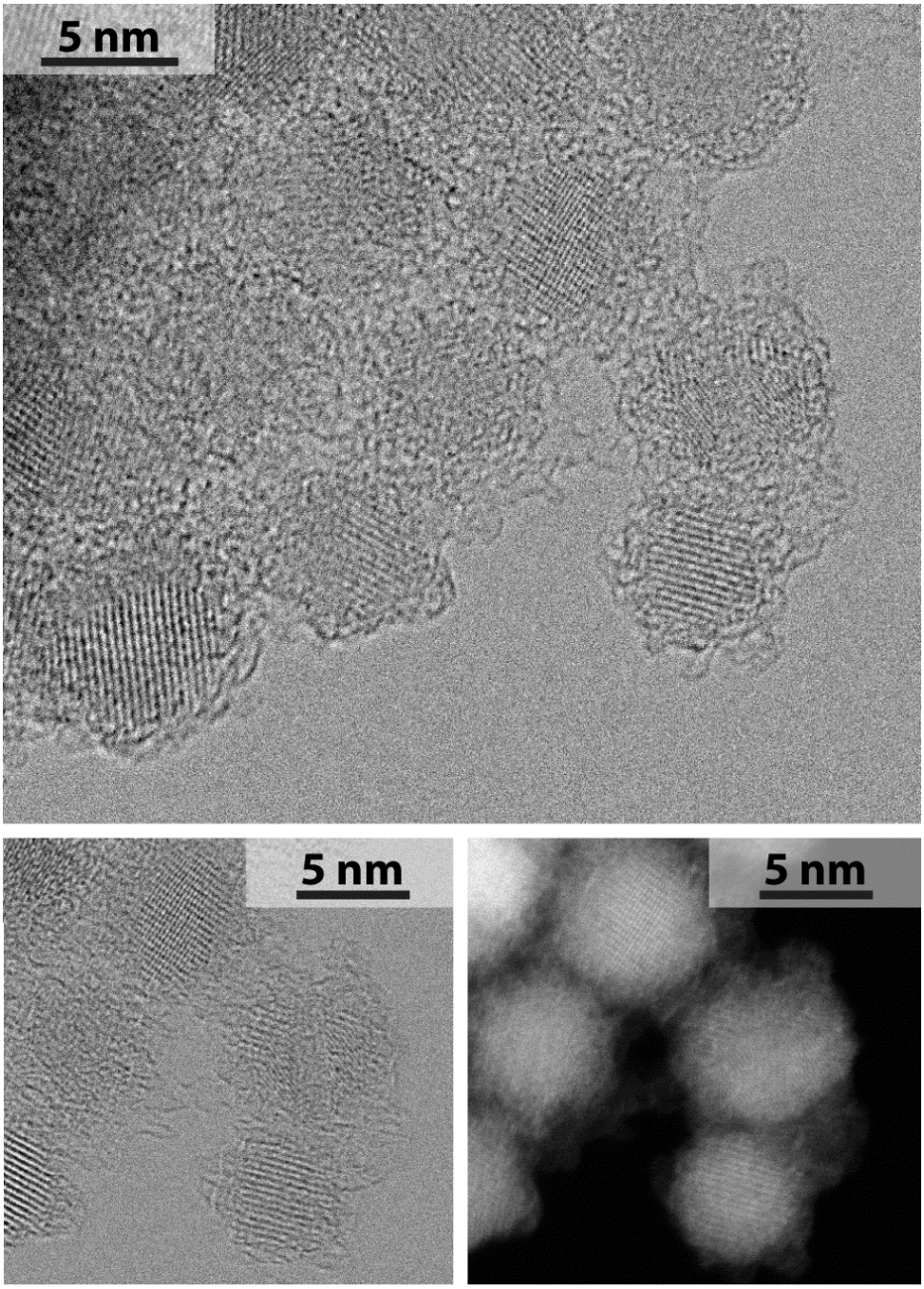

Figure 7.5. STEM images of a monolayer of alkene-passivated nanocrystals suspended over vacuum.

The observed conformations of ligands adsorbed to the graphene substrate remained intact under prolonged exposure to the electron beam (>10 min) at 80 kV under scanning mode. The buildup of carbon from organic contaminants is a common problem in TEM due to the small, high energy probe that can gather and polymerize carbonaceous molecules. [24] The capping ligands employed here for the Si nanocrystals are relatively non-volatile and may help limit the carbon buildup under electron beam, in contrast to what has been observed with more volatile ligands.[25]

7.4.5. Imaging of Hydrogen-terminated Silicon Nanocrystals

In comparison, Si nanocrystals that were not capped with organic ligands were also imaged. Figure 7.6 shows STEM images of Si nanocrystals taken immediately from the HF/HCl etch. The surfaces of these nanocrystals are predominantly terminated with hydrogen. No ligand shell is observed in either the dark or bright field STEM images. However, the surfaces of these nanocrystals tended to have a very thin (< 1 nm) amorphous layer, which may be a result of some oxidation. Dark field STEM imaging revealed the presence of many small (< 2nm) amorphous clusters around the nanocrystals, which were not visible in bright field. These clusters have lower contrast than the crystalline silicon particles and may be residual silicon dioxide remaining from the HF/HCl etch, or perhaps amorphous Si clusters formed during the nanocrystal synthesis. These tiny clusters are not visible in the bright field images, and are not observed in the alkene-passivated nanocrystal samples. These clusters are either removed

during the hydrosilylation/cleaning steps or it is possible that the ligands have similar contrast to these clusters, making them impossible to see.

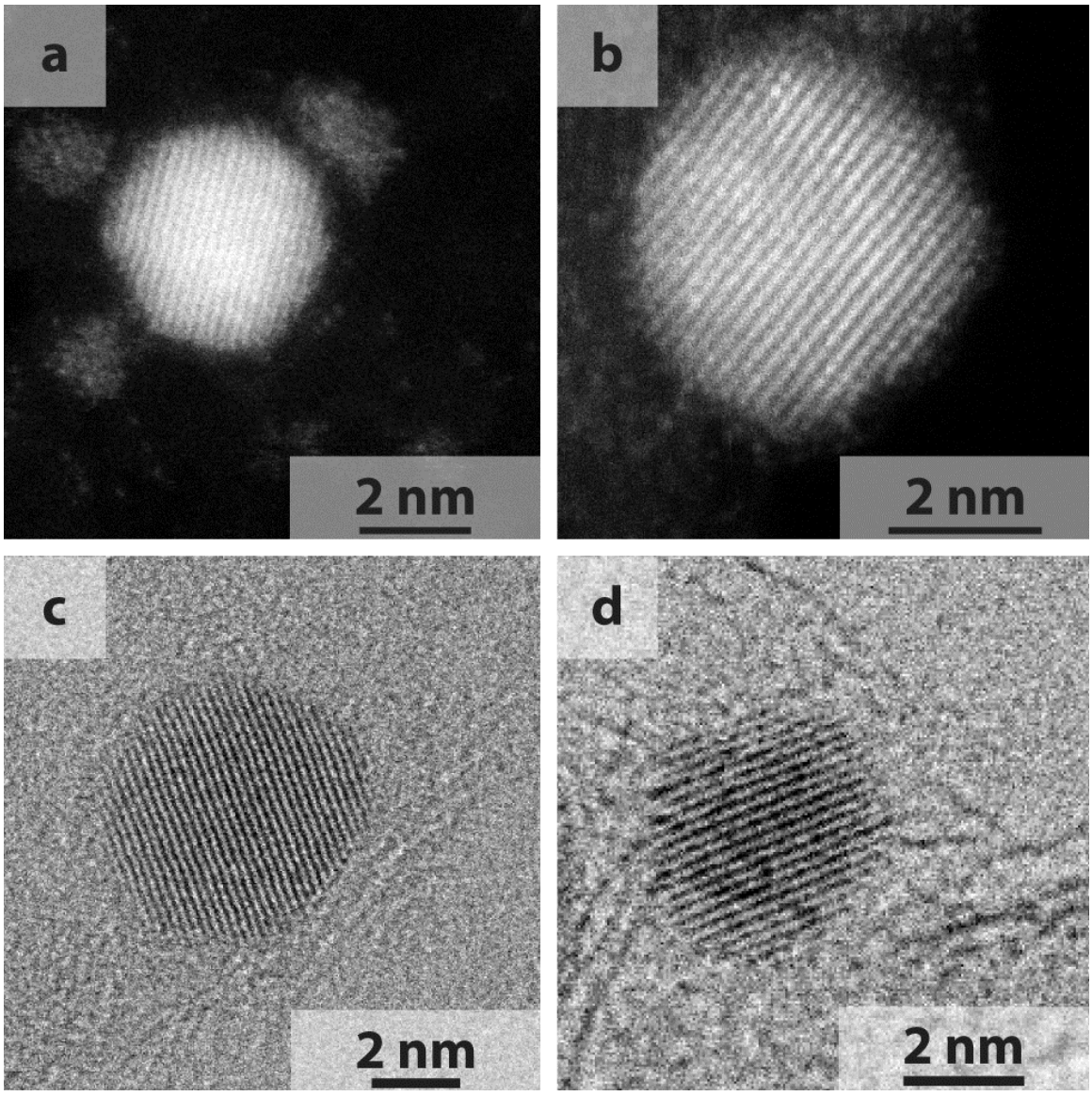

Figure 7.6. Dark field (a,b) and bright field (c,d) STEM images of Si nanocrystals isolated after acid etching of the SiO_2 matrix prior to hydrosilylation with alkene capping ligands.

7.4.6. Imaging of Defects in Si Nanocrystals

Many of the Si nanocrystals had a significant amount of twinning. Figure 7 shows a number of STEM images of Si nanocrystals on graphene. Some nanocrystals did not show any sign of twinning and the observed lattice spacings were consistent with diamond cubic Si. The lattice spacing in the twinned nanocrystals, however, often did not match diamond cubic Si.

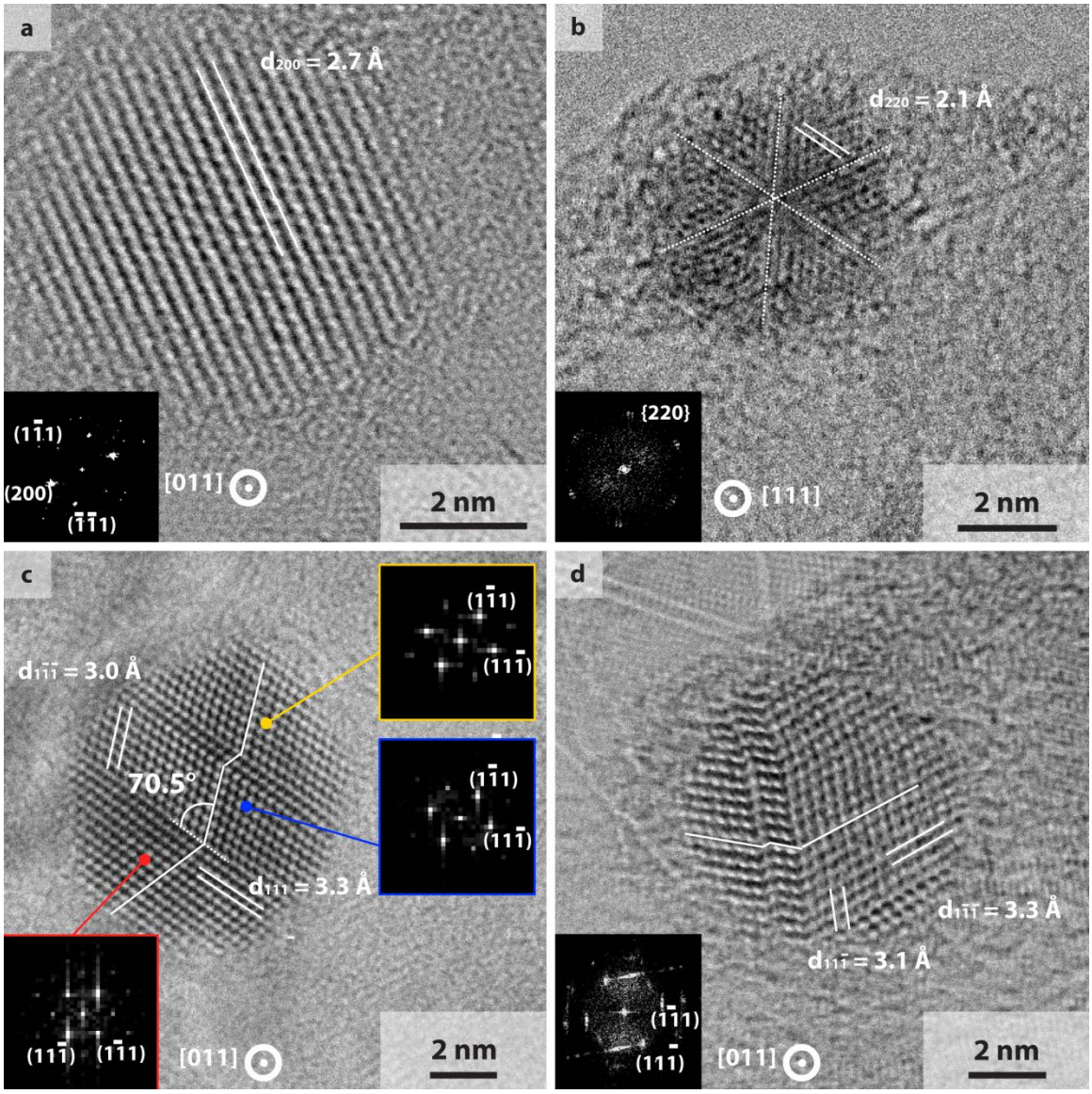

Figure 7.7. Bright field STEM images of defect free (a) and twinned (b – c) silicon nanocrystals. The bulk spacings for Si (200), (220), and (111) lattice planes are 2.71, 1.92, and 3.13 Å, respectively.

Twinning in Si nanocrystals synthesized via heating of silicon rich oxides has been reported by Wang et al.[26] In their report, twinning was observed often, most commonly in the (111) planes, which we have also found (Figure 7 c and d). Figure 7b shows an unpassivatred nanocrystal with radial hexafold twinning. Iijima observed pentafold radial twinning in much larger Si nanocrystals (~80 nm diameter) in 1987,[27], but there have been few reports of radial twinning in Si nanocrystals since. An examination of the lattice spacings of the twinned nanocrystals revealed that there was significant inhomogeneous lattice strain, which was not present in the untwinned nanocrystals. Figure 6a shows a nanocrystal without twinning and the expected (200) lattice spacing of 2.7 Å corresponding to diamond cubic Si. The nanocrystal in Figure 6b with radial twinning has a (220) spacing of 2.1 Å, which is 9% larger than the expected value of 1.9 Å. Lattice planes that should correspond to {111} lattice planes are visible in the nanocrystals in Figures 6b and 6c, but these planes have d-spacings of 3.0 and 3.3 Å, which differ significantly from the expected value of 3.1 Å. The asymmetry in the lattice implies that they have a tetragonal or orthorhombic crystal structure, which could have substantial effects in the optical and electronic properties of the nanocrystals. Zacharias and coworkers found inhomogeneous strain of up to 3% in twinned nanocrystals embedded in in silica.[28] In Iijima's study, strain as high as 10.3% was found in silicon nanocrystals with five-fold twinning.[27] Similar inhomogeneous lattice strain has also been observed in twinned Ge[29] and C (diamond) nanocrystals._ENREF_8_30

7.4.7. Comparison of Different Methods

Figure 8 shows images of Si nanocrystals using the various techniques of HRTEM, and dark- and bright-field STEM presented in this *Letter*. The imaging contrast is enhanced significantly by using graphene as an imaging support. The Cs-corrected dark-field and bright-field STEM images provide complementary information. The contrast in the dark field images acquired using a HAADF detector are highly dependent on the electron density of the material (Z-contrast). The bright-field STEM images look similar to HRTEM images, with imaging contrast arising from Bragg scattering. Accordingly, the contrast in these images is highly dependent on the crystal zone axis. The organic capping ligands are only visible using low accelerating voltage (<120 kV) on graphene. Because graphene is atomically thin, flat, with crystallographically ordered carbon atoms, the molecularly thin hydrocarbon strands are observable due to the thickness contrast.

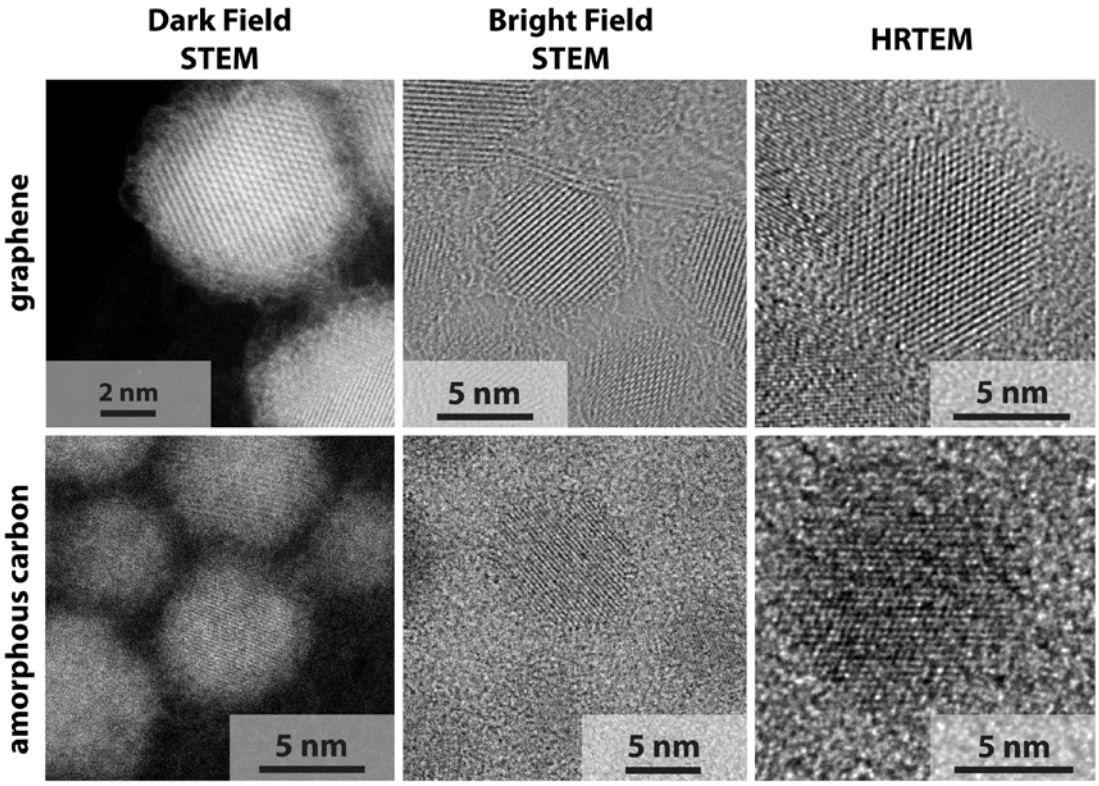

Figure 7.8. Electron microscopy images of organic ligand-stabilized Si nanocrystals using different supports and imaging techniques. (Top row) Si nanocrystals on graphene and (bottom row) amorphous carbon supports. From left to right: Dark field STEM, Bright field STEM, and HRTEM.

7.5. CONCLUSIONS

Graphene supports enable TEM and STEM imaging of organic ligand-coated Si nanocrystals with significantly improved contrast compared to conventional amorphous carbon supports. Using Cs-corrected STEM, the silicon nanocrystals could be imaged very clearly on graphene. Twinning was observed in several unpassivated Si nanocrystals, including hexafold radial twinning. Due to the relative transparency of graphene, the organic molecules passivating the silicon surface could be imaged in both

bright in dark field. The ability to image silicon nanocrystal surfaces, interfaces, and defects is integral to understanding the properties of these materials. For example, since the early 1990's there has been controversy surrounding the origin of Si nanocrystal photoluminescence – whether it is due to quantum confinement, or due to a defect or interfacial trap. In addition, ability to image organic molecules and inorganic/organic interfaces provides the opportunity to directly observe and verify molecular and biomolecular conformation, molecular interactions, and interfacial phenomena at an atomic level. Most methods employed to measure size and shape of these "soft" materials are indirect (i.e. light scattering, chromatography). Direct imaging of these materials typically requires a stain based on heavy atoms to provide contrast or cryogenically freezing the sample. Both of these methods yield images that are oftentimes difficult to interpret. Even finer structure could potentially be resolved by using lower accelerating voltage and cryogenic temperatures. Graphene imaging supports could become widely adapted due to its ease of synthesis and greatly enhanced imaging capability.

7.6. REFERENCES

1. Geim, A. K.; Novoselov, K. S. *Nature Mater.* **2007,** 6, 183-191.

2. Dato, A.; Radmilovic, V.; Lee, Z.; Phillips, J.; Frenklach, M. *Nano Letters* **2008,** 8, (7), 2012-2016.

3. Li, X.; Cai, W.; An, J.; Kim, S.; Nah, J.; Yang, D.; Piner, R.; Velamakanni, A.; Jung, I.; Tutuc, E.; Banerjee, S. K.; Colombo, L.; Ruoff, R. S. *Science* **2009,** 324, (5932), 1312-1314.

4. Zhu, Y.; Murali, S.; Cai, W.; Li, X.; Suk, J. W.; Potts, J. R.; Ruoff, R. S. *Adv Mater* **2010,** 22, (35), 3906-24.

5. Lightcap, I. V.; Kosel, T. H.; Kamat, P. V. *Nano Letters* **2010,** 10, (2), 577-583.

6. Kamat, P. V. *The Journal of Physical Chemistry Letters* **2009,** 1, (2), 520-527.

7. Kamat, P. V. *The Journal of Physical Chemistry Letters* **2011,** 2, (3), 242-251.

8. Yuk, J. M.; Kim, K.; Aleman, B.; Regan, W.; Ryu, J. H.; Park, J.; Ercius, P.; Lee, H. M.; Alivisatos, A. P.; Crommie, M. F.; Lee, J. Y.; Zettl, A. *Nano Lett* **2011**.

9. Kim, K.; Lee, Z.; Regan, W.; Kisielowski, C.; Crommie, M. F.; Zettl, A. *ACS nano* **2011,** 5, (3), 2142-2146.

10. Meyer, J. C.; Geim, A. K.; Katsnelson, M. I.; Novoselov, K. S.; Booth, T. J.; Roth, S. *Nature* **2007,** 446, (7131), 60-63.

11. Meyer, J. C.; Girit, C. O.; Crommie, M. F.; Zettl, A. *Nature* **2008,** 454, (7202), 319-322.

12. Meyer, J. C.; Kisielowski, C.; Erni, R.; Rossell, M. D.; Crommie, M. F.; Zettl, A. *Nano Letters* **2008,** 8, (11), 3582-3586.

13. Gass, M. H.; Bangert, U.; Bleloch, A. L.; Wang, P.; Nair, R. R.; Geim, A. K. *Nat Nano* **2008,** 3, (11), 676-681.

14. Lee, Z.; Jeon, K.-J.; Dato, A.; Erni, R.; Richardson, T. J.; Frenklach, M.; Radmilovic, V. *Nano Letters* **2009,** 9, (9), 3365-3369.

15. McBride, J. R.; Lupini, A. R.; Schreuder, M. A.; Smith, N. J.; Pennycook, S. J.; Rosenthal, S. J. *ACS Applied Materials & Interfaces* **2009,** 1, (12), 2886-2892.

16. Westenfelder, B.; Meyer, J. C.; Biskupek, J.; Algara-Siller, G.; L.G. Lechner; J. Kusterer; U. Kaiser; III, C. E. K.; E. Kohn; Scholz, F. *Journal of Physics D: Applied Physics* **2011,** 44, (5), 055502.

17. Warner, J. H.; Rümmeli, M. H.; Bachmatiuk, A.; Wilson, M.; Büchner, B. *ACS nano* **2009,** 4, (1), 470-476.

18. Wu, Y. A.; Kirkland, A. I.; Schaffel, F.; Porfyrakis, K.; Young, N. P.; Briggs, G. A. D.; Warner, J. H. *Nanotechnology* **2011,** 22, (19), 195603.

19. Hessel, C. M.; Henderson, E. J.; Veinot, J. G. C. *Chemistry of Materials* **2006,** 18, (26), 6139-6146.

20. Hessel, C. M.; Rasch, M. R.; Hueso, J. L.; Goodfellow, B. W.; Akhavan, V. A.; Puvanakrishnan, P.; Tunnel, J. W.; Korgel, B. A. *Small* **2010,** 6, (18), 2026-34.

21. Hummers, W. S.; Offeman, R. E. *Journal of the American Chemical Society* **1958,** 80, (6), 1339-1339.

22. Park, S.; An, J.; Jung, I.; Piner, R. D.; An, S. J.; Li, X.; Velamakanni, A.; Ruoff, R. S. *Nano Letters* **2009,** 9, (4), 1593-1597.

23. Girit, Ç. Ö.; Meyer, J. C.; Erni, R.; Rossell, M. D.; Kisielowski, C.; Yang, L.; Park, C.-H.; Crommie, M. F.; Cohen, M. L.; Louie, S. G.; Zettl, A. *Science* **2009,** 323, (5922), 1705-1708.

24. Ennos, A. E. *British Journal of Applied Physics* **1953,** 4, (4), 101.

25. Holmberg, V. C.; Panthani, M. G.; Korgel, B. A. *Science* **2009,** 326, (5951), 405-7.

26. Wang, Y. Q.; Smirani, R.; Ross, G. G. *Nano Letters* **2004,** 4, (10), 2041-2045.

27. Iijima, S. *Japanese Journal of Applied Physics* **1987,** 26, (3), 365-372.

28. Zacharias, M.; Blasing, J.; Veit, P.; Tsybeskov, L.; Hirschman, K.; Fauchet, P. M. *Applied Physics Letters* **1999,** 74, (18), 2614-2616.

29. Saito, Y. *Journal of Crystal Growth* **1979,** 47, 61-72.

Chapter 8: Conclusions and Future Research Directions

8.1. Conclusions

Nanomaterials have unique size, shape, and surface-dependent properties. Because of their unique electrical, optical and mechanical properties, they have been regarded as novel materials for several new technologies in widely diverse application areas. Because of the nanocrystals' quantized optical properties, the ability to assemble into crystals, and the potential for making new "metamaterials", nanocrystals (particularly quantum dots) are sometimes called "artificial atoms".

The research presented in this dissertation aimed to demonstrate the controlled synthesis of nanomaterials that could be potentially be used for inorganic, solution processed photovoltaic applications. In the case of $CuInSe_2$ nanocrystals, the system was highly optimized, and power conversion efficiencies of 3.1% were achieved.[1] By modifying the reaction scheme for $CuInSe_2$ nanocrystals, quantum confined $CuInS_XSe_{2-X}$ nanocrystals were formed.

Silicon nanocrystals are an intriguing material for optoelectronics and photovoltaics. Optical transitions that are typically forbidden in bulk silicon due to its indirect bandgap can be spectroscopically allowed when nanoscale due to low translational symmetry. Synthesizing nanocrystals from HF-etched annealed hydrogen silsesquioxane[2] provides a good testbed for controllably making Si nanocrystals with good size polydispersibilities, controllable surface functionalization, and solution procesability.

Graphene has garnered a great deal of interest over the past few years. Its "discovery" in 2004[3] has led to a flurry of research investigating its properties, synthesis methods, and applications. This led to the 2010 Nobel Prize in Physics to be awarded to Andre Geim and Kostya Novoselov at Manchester University for "for groundbreaking experiments regarding the two-dimensional material graphene". While graphene ultimately may not be a replacement for Si and CMOS devices, it has potential to fill some niche applications. At the very least, it is an interesting testbed for fundamental physics, as well as an easy-to-use and effective support for transmission electron microscopy.

While the research discussed in this dissertation has a focus on photovoltaic applications for colloidal nanocrystals, the work did diverge into tangential applications. The goal of synthesizing quantum confined I-III-VI nanocrystals was not initially to use them for biomedical applications. However, their strong NIR absorbance and luminescence made them well-suited for this application.

8.1.1. Nanocrystal-based Photovoltaics

Rising energy prices over the past ~10 years has renewed interest in finding sustainable energy sources. Solar, wind, biomass, and geothermal are typically discussed when discussing renewable energy sources that potentially have little environmental impact. Solar is particularly intriguing due to a lack of moving parts, and the huge amount of solar power irradiated upon the earth year. Current methods to making solar cells have made them cost prohibitive. Crystalline silicon dominates the market, but its low absorption coefficient and extremely high purity (necessary due to high thickness

required) makes it too costly. Silicon processing for PVs is a highly mature technology, with most processes borrowed from traditional silicon CMOS processing. Amorphous silicon (a-Si) behaves like a direct bandgap semiconductor, but it is not every efficient or stable.[4] Organics and polymers also suffer from poor stability. Organics, polymers, and a-Si may be better suited for niche applications like consumer electronics due to their poor stability.

The two other main technologies remaining are CdTe and CIGS. Both of these offer great potential efficiencies. The main producer of CdTe modules, First Solar, has been able to produce modules at less than $1/Wp (Wp = peak watt; cost of power under peak illumination conditions). For solar cells to reach grid parity, total installed cost needs to be reduced to less than $1/ Wp. For comparison, crystalline Si modules are ~$3/Wp (before installation).

A truly disruptive technology would reduce this $/Wp by one or two orders of magnitude – that is the actual solar cell would be negligible in cost compared to its installation. The high cost of thin film PVs is associated with high temperature and high vacuum processing, which are energy-, time-, and capital-intensive. Solution processing could allow for low temperature, ambient processing that is amenable to roll to roll (rather than batch) processing. Nanocrystals are one option that could potentially fit these processing requirements. So far, power conversion efficiencies of up to 6.0%[5] have been achieved using room-temperature processed nanocrystals as an absorber material.

Chapters 3 and 4 discussed utilization of $CuInSe_2$ nanocrystals for photovoltaic applications. Compared to other similar efforts, this was one of the few that resulted in stable, moderately high (>3%) with absorber layers processed under ambient environment and low temperature. Devices using CuInSe2 nanocrystals showed little degradation in performance even after repeated testing, after several months of storage.

8.1.2. Quantum dot Based Photovoltaics

The $CuInSe_XS_{2-X}$ quantum dots discussed in Chapter 5 were used for biomedical applications, but it would be interesting to use them in solar cells. Quantum dot based solar cells have typically utilized Pb-chalcogenide nanocrystals (PbSe, PbS) that have very high dielectric constants, resulting in very strong quantum confinement effects (Bohr exciton radius ~40 nm). Using quantum dots for photovoltaics is an intriguing prospect, not only as a practical choice, but as a scientific study. For quantum dots to have properties, some localization of carriers must occur. That is, the electron and hole wavefunctions should not "leak" out into free space or the rest of the film. However, for good charge transport to occur through films, good coupling is desired. It is yet to be determined whether this can be done effectively in films thick enough to absorb all incoming light.

8.1.3. Silicon Nanomaterials

Silicon is a favorite material for study by materials scientists and physicists. The electronic properties and surface chemistry of Si are well understood and well characterized. Its simplicity in structure and stability allows for ease in comparison of theoretical study to experiment. The silicon nanocrystals studied her were synthesized via annealing HSQ, etching away oxide with HF, and passivating the surface as desired.[2] The optical properties were measured as well, with measured photoluminescence out to nearly the band edge of bulk Si.

8.2. FUTURE RESEARCH DIRECTIONS

8.2.1. Nanocrystal-based Photovoltaics

While the work featured in this dissertation uses $CuInSe_2$ as a model system for photovoltaics, it may not be the best choice. $CuInSe_2$ (and CIGS) were used due to their

high performance as a *bulk* polycrystalline film. The transport in highly granular films, however, is completely different than in large-grained crystalline systems.[6] Furthermore, the properties of nanomaterials can be drastically different compared to their bulk counterparts, so materials that work well in bulk devices may not necessarily be the best for nanocrystal-based devices. Much of the recent work in this field has utilized lead chalcogenide nanocrystals, which are poor-suited for bulk photovoltaics due to a very low bandgap.[7-10] Recent years have seen a flurry of research in developing new nanomaterials, so this may help find some alternative materials.

Colloidal nanocrystal-based solar cells have demonstrated high internal quantum efficiencies, but low external quantum efficiencies. This is because the thickness of films utilized in the most efficient nanocrystal-based solar cells needs to double or triple to absorb all incoming light. One approach is to improve the electronic properties, but alternatively an area of research that could utilize this technology is light-trapping. This would benefit not only nanocrystal-based solar cells, but also other technologies like "thin Si", which utilizes submicron Si substrates that can tolerate a much higher concentration of defects. Figure 8.1 illustrates the fraction of the AM1.5 spectrum absorbed by various thicknesses of CIS nanocrystals and crystalline Si.

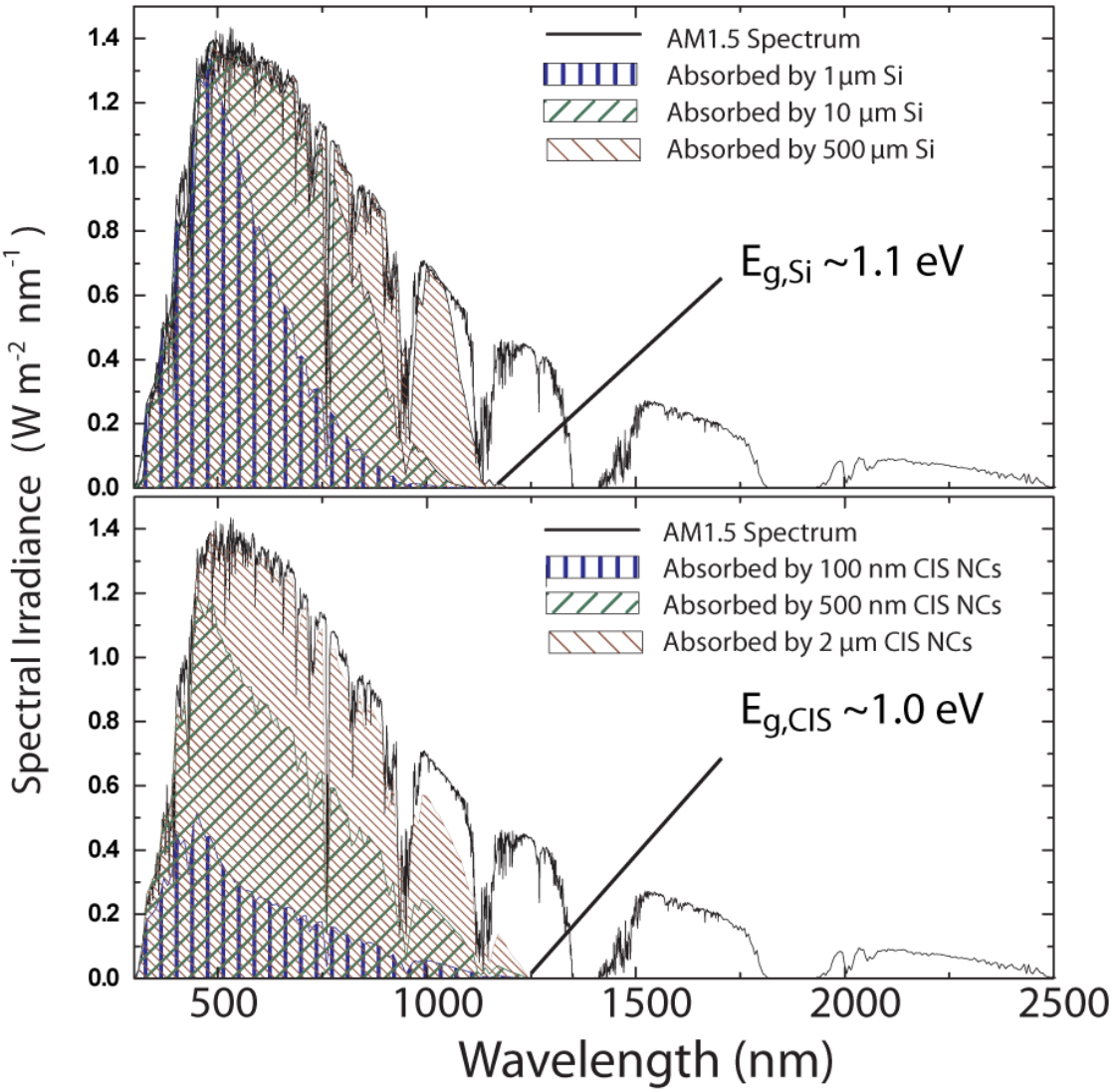

Figure 8.1. Illustration of fraction of solar spectrum absorbed by various thickness of crystalline Si (top) and CIS nanocrystals (bottom).

Control of the electronic properties is crucial to developing high-efficiency nanocrystal-based photovoltaics. Much of the current research effort has focused on increasing carrier mobility, and great strides have been made on this front.[11] However,

studies that study the carrier concentration of nanocrystal films have been limited.[1, 12, 13] Interfaces play a dominant role in the electronic properties of nanocrystal films. Atoms adsorbed to the surface have shown to both enhance mobility[14] and doping. Being able to control both simultaneously would be a breakthrough that would not only impact nanocrystal-based photovoltaics, but also optoelectronics and other electronic devices that could benefit from solution processability.

8.2.1.2. Quantum Dots for Photovoltaics and other Electronic Devices

Quantum dots are nanocrystals that exhibit quantum confinement effects in 3 dimensions. The quantum dots ($CuInSe_XS_{2-X}$; CISS) studied in this dissertation were used for biological imaging, but there is currently active research for using quantum dots for electronics. A fundamental dilemma that arises with using quantum dots arises from the mechanism of quantum confinement – for quantum effects to take place, the charge carriers in the nanocrystal must be localized to some extent within the crystal. However, for applications such as photovoltaics, charge carriers generated within the nanocrystal need to be delocalized to efficiently extract charge. It remains to be seen whether charge extraction can occur efficiently in films thick enough to absorb all incoming light from the sun.

8.2.1.3. Silicon Luminescence

Silicon photoluminescence remains a somewhat controversial topic, largely because of the discrepancy found in literature regarding the properties of luminescent silicon materials. Additionally, the photoluminescence quantum yield reported in this dissertation is around 10%, while others have reported quantum yields as high as 60%.[15]

Further investigation must be done on the role of defects and passivation in Si nanocrystals. Light emitting diodes utilizing Si nanocrystals synthesized by the Kortshagen group have recently demonstrated power efficiencies of over 8%[16] This is the highest reported power efficiency for nanocrystal light emitting diodes to date.

8.2.1.4. Graphene as a TEM support

Chapter 7 shows the use of graphene as a TEM support. The ability to image an inorganic-organic interface has implications not only for nanomaterials, but also biology, surface chemistry, and study of other "soft" condensed matter. The ability to have an atomically-thin substrate that dissipates heat and electricity makes it an ideal support for TEM.

8.3. REFERENCES

1. Akhavan, V. A.; Panthani, M. G.; Goodfellow, B. W.; Reid, D. K.; Korgel, B. A. *Optics express* **2010,** 18 Suppl 3, A411-20.

2. Hessel, C. M.; Henderson, E. J.; Veinot, J. G. C. *Chemistry of Materials* **2006,** 18, (26), 6139-6146.

3. Novoselov, K. S. *Nature* **2005,** 438, 197-200.

4. Staebler, D.; Wronski, C. *Appl. Phys. Lett.* **1977,** 31, (4), 292.

5. Tang, J.; Kemp, K. W.; Hoogland, S.; Jeong, K. S.; Liu, H.; Levina, L.; Furukawa, M.; Wang, X.; Debnath, R.; Cha, D.; Chou, K. W.; Fischer, A.; Amassian, A.; Asbury, J. B.; Sargent, E. H. *Nature materials* **2011,** 10, (10), 765-771.

6. Mott, N. F., Conduction in Non-Crystalline Materials. In Oxford University Press, USA: 1987.

7. Pietryga, J. M.; Schaller, R. D.; Werder, D.; Stewart, M. H.; Klimov, V. I.; Hollingsworth, J. A. *J Am Chem Soc* **2004,** 126, (38), 11752-3.

8. Schaller, R. D.; Klimov, V. I. *Physical review letters* **2004,** 92, (18), 186601.

9. Cho, K.-S.; Talapin, D. V.; Gaschler, W.; Murray, C. B. *Journal of the American Chemical Society* **2005,** 127, (19), 7140-7147.

10. McDonald, S. A.; Konstantatos, G.; Zhang, S.; Cyr, P. W.; Klem, E. J.; Levina, L.; Sargent, E. H. *Nature materials* **2005,** 4, (2), 138-42.

11. Lee, J.-S.; Kovalenko, M. V.; Huang, J.; Chung, D. S.; Talapin, D. V. *Nature Nanotechnology* **2011,** 6, (6), 348-352.

12. Pattantyus-Abraham, A. G.; Kramer, I. J.; Barkhouse, A. R.; Wang, X.; Konstantatos, G.; Debnath, R.; Levina, L.; Raabe, I.; Nazeeruddin, M. K.; Gratzel, M.; Sargent, E. H. *ACS nano* **2010,** 4, (6), 3374-80.

13. Debnath, R.; Tang, J.; Barkhouse, D. A.; Wang, X.; Pattantyus-Abraham, A. G.; Brzozowski, L.; Levina, L.; Sargent, E. H. *J Am Chem Soc* **2010,** 132, (17), 5952-3.

14. Luther, J. M.; Law, M.; Song, Q.; Perkins, C. L.; Beard, M. C.; Nozik, A. J. *ACS nano* **2008,** 2, (2), 271-80.

15. Jurbergs, D.; Rogojina, E.; Mangolini, L.; Kortshagen, U. *Appl. Phys. Lett.* **2006,** 88, (23), 233116.

16. Cheng, K.-Y.; Anthony, R.; Kortshagen, U. R.; Holmes, R. J. *Nano Letters* **2011,** 11, (5), 1952-1956.

Appendix

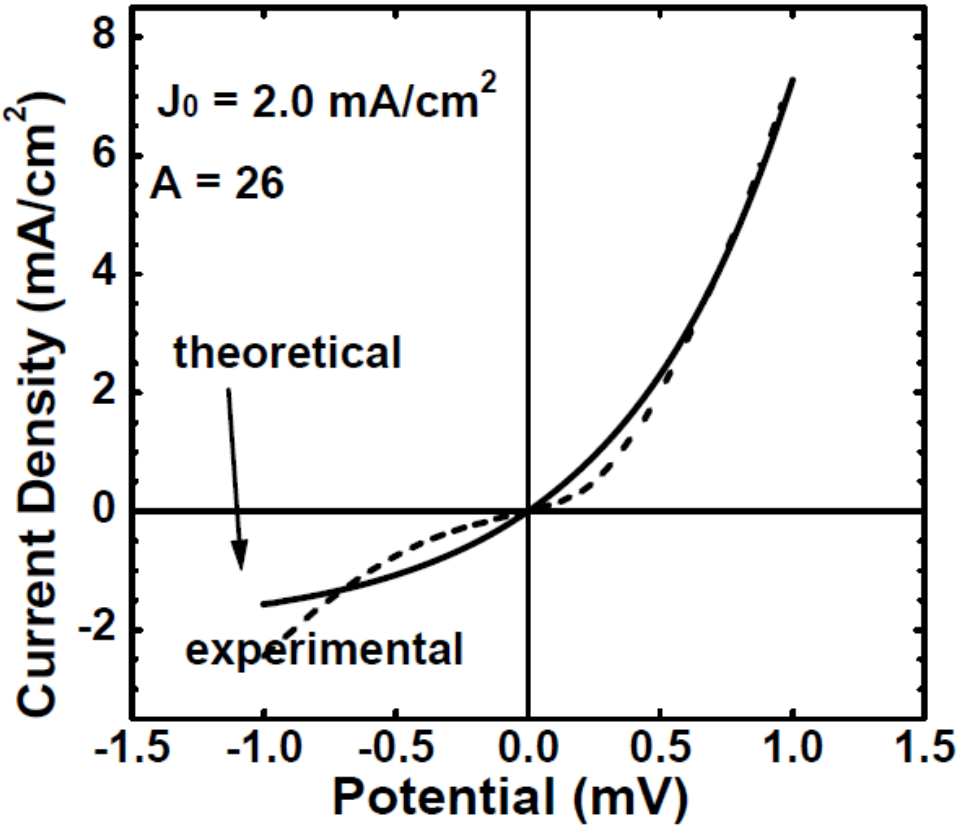

Figure A1. Dark current-voltage (I-V) response of the $CuInSe_2$ nanocrystal PV device from Figure 16 (solid line). The dashed line is a curve fit of the dark I-V response to the I-V behavior expected for an ideal diode: $J(V) = J_0[\exp(qVAkT) - 1]$, where J_0 is the saturation current density, q is the absolute electron charge, k is Boltzmann's constant, A is the ideality factor, and T is temperature.

Glossary

Band gap: in a semiconductor, the difference in energy from the valence band maximum to the conduction band minimum.

Capping Ligand: a chemical species applied to stabilize and passivate nanocrystal surfaces and provide dispersibility in a solvent.

Charge carrier: charge carrying species in solid-state devices, i.e., electrons (negative charge) and holes (positive charge).

Colloidal quantum dot: a semiconductor nanocrystal that exhibits quantum confinement; typically observed as a spectral blueshift of the optical absorbance and/or photoluminescence with decreasing size.

Electronics: technologies that utilize electron flow, generation, and/or recombination.

Indirect band gap semiconductor: a semiconductor that has its conduction band minimum and valence band maximum at different crystal momenta.

Nanocrystal: a crystalline nanoparticle with a diameter between 1 and 20 nm.

Photovoltaic device: a semiconductor device that converts sunlight directly to electricity.

Quantum confinement: change of electronic and optical properties when the material sampled is of sufficiently small size. The bandgap of a semiconductor increases as the size of the nanostructure decreases. This phenomenon results from electrons and holes being confined into dimensions that approach the exciton Bohr radius.

Thin film transistor: a field effect transistor in which the channel material is a thin film semiconductor deposited on a supporting substrate.

Thermoelectric device: a semiconductor device converts heat to electricity, or uses electricity to cool a system.

Light emitting diode: a semiconductor device that converts electricity into light via radiative recombination of electrons and holes.

References

Achermann, M., M. A. Petruska, et al. (2004). "Energy-transfer pumping of semiconductor nanocrystals using an epitaxial quantum well." Nature **429**(6992): 642-646.

Akhavan, V. A., M. G. Panthani, et al. (2010). "Thickness-limited performance of CuInSe nanocrystal photovoltaic devices." Opt Express **18 Suppl 3**: A411-420.

Alivisatos, A. P., W. Gu, et al. (2005). "Quantum dots as cellular probes." Annu Rev Biomed Eng **7**: 55-76.

Allen, P. M. and M. G. Bawendi (2008). "Ternary I-III-VI quantum dots luminescent in the red to near-infrared." J Am Chem Soc **130**(29): 9240-9241.

Allen, P. M., W. Liu, et al. (2010). "InAs(ZnCdS) quantum dots optimized for biological imaging in the near-infrared." J Am Chem Soc **132**(2): 470-471.

Allen, P. M., B. J. Walker, et al. (2010). "Mechanistic insights into the formation of InP quantum dots." Angew Chem Int Ed Engl **49**(4): 760-762.

Altshuler, B. and A. Aronov (1985). Electron-Electron Interactions in Disordered Conductors. North-Holland, Amsterdam.

Andres, R. P., T. Bein, et al. (1996). ""Coulomb Staircase" at Room Temperature in a Self-Assembled Molecular Nanostructure." Science **272**(5266): 1323-1325.

Bar, M., I. Repins, et al. (2009). "Chemical and electronic surface structure of 20%-efficient Cu(In,Ga)Se2 thin film solar cell absorbers." Applied Physics Letters **95**(5): 3.

Baranov, D., A. Fiore, et al. (2010). "Assembly of colloidal semiconductor nanorods in solution by depletion attraction." Nano Lett **10**(2): 743-749.

Bawendi, M. G., W. L. Wilson, et al. (1990). "Electronic structure and photoexcited-carrier dynamics in nanometer-size CdSe clusters." Phys Rev Lett **65**(13): 1623-1626.

Bodnarchuk, M. I., M. V. Kovalenko, et al. (2010). "Energetic and Entropic Contributions to Self-Assembly of Binary Nanocrystal Superlattices: Temperature as the Structure-Directing Factor." Journal of the American Chemical Society **132**(34): 11967-11977.

Bruchez, M., Jr., M. Moronne, et al. (1998). "Semiconductor nanocrystals as fluorescent biological labels." Science **281**(5385): 2013-2016.

Brus, L. (1984). "Electron?electron and electron?hole interactions in small semiconductor crystallites: The size dependence of the lowest excited electronic state." J. Chem. Phys. **80**(9): 4403.

Brus, L. (1986). "Electronic wave functions in semiconductor clusters: experiment and theory." The Journal of Physical Chemistry **90**(12): 2555-2560.

Buzea, C. (2007). "Nanomaterials and nanoparticles: Sources and toxicity." Biointerphases **2**(4): MR17.

Canham, L. T. (1990). "Silicon Quantum Wire Array Fabrication by Electrochemical and Chemical Dissolution of Wafers." Applied Physics Letters **57**(10).

Chelikowsky, J. R. and M. L. Cohen (1974). "Electronic structure of silicon." Physical Review B **10**(12): 5095-5107.

Cheng, K.-Y., R. Anthony, et al. (2011). "High-Efficiency Silicon Nanocrystal Light-Emitting Devices." Nano Letters **11**(5): 1952-1956.

Cho, K.-S., D. V. Talapin, et al. (2005). "Designing PbSe Nanowires and Nanorings through Oriented Attachment of Nanoparticles." Journal of the American Chemical Society **127**(19): 7140-7147.

Clark, M. A., B. H. Hirst, et al. (1998). "M-Cell Surface beta 1 Integrin Expression and Invasin-Mediated Targeting of Yersinia pseudotuberculosis to Mouse Peyer's Patch M Cells." Infect. Immun. **66**(3): 1237-1243.

Cozzoli, P. D., T. Pellegrino, et al. (2006). "Synthesis, properties and perspectives of hybrid nanocrystal structures." Chem Soc Rev **35**(11): 1195-1208.

Cullis, A. G. and L. T. Canham (1991). "Visible light emission due to quantum size effects in highly porous crystalline silicon." Nature **353**(6342): 335-338.

Dato, A., V. Radmilovic, et al. (2008). "Substrate-Free Gas-Phase Synthesis of Graphene Sheets." Nano Letters **8**(7): 2012-2016.

Debnath, R., J. Tang, et al. (2010). "Ambient-processed colloidal quantum dot solar cells via individual pre-encapsulation of nanoparticles." J Am Chem Soc **132**(17): 5952-5953.

Deka, S., A. Quarta, et al. (2009). "CdSe/CdS/ZnS double shell nanorods with high photoluminescence efficiency and their exploitation as biolabeling probes." J Am Chem Soc **131**(8): 2948-2958.

Dong, A., J. Chen, et al. (2011). "Multiscale Periodic Assembly of Striped Nanocrystal Superlattice Films on a Liquid Surface." Nano Letters **11**(2): 841-846.

Dong, A., J. Chen, et al. (2010). "Binary nanocrystal superlattice membranes self-assembled at the liquid-air interface." Nature **466**(7305): 474-477.

Dorn, A., P. M. Allen, et al. (2010). "In situ electrical monitoring of cation exchange in nanowires." Nano Lett **10**(10): 3948-3951.

Doty, R. C., H. Yu, et al. (2001). "Temperature-Dependent Electron Transport through Silver Nanocrystal Superlattices." The Journal of Physical Chemistry B **105**(35): 8291-8296.

Dubertret, B., P. Skourides, et al. (2002). "In vivo imaging of quantum dots encapsulated in phospholipid micelles." Science **298**(5599): 1759-1762.

Engtrakul, C., Y. H. Kim, et al. (2006). "Self-assembly of linear arrays of semiconductor nanoparticles on carbon single-walled nanotubes." J Phys Chem B **110**(50): 25153-25157.

Ennos, A. E. (1953). "The origin of specimen contamination in the electron microscope." British Journal of Applied Physics **4**(4): 101.

Erogbogbo, F., T. Liu, et al. (2011). "Creating Ligand-Free Silicon Germanium Alloy Nanocrystal Inks." ACS Nano.

Farokhzad, O. C. and R. Langer (2006). "Nanomedicine: Developing smarter therapeutic and diagnostic modalities." Advanced Drug Delivery Reviews **58**(14): 1456-1459.

Ford, G. M., Q. Guo, et al. (2011). "Earth Abundant Element Cu2Zn(Sn1−xGex)S4 Nanocrystals for Tunable Band Gap Solar Cells: 6.8% Efficient Device Fabrication." Chemistry of Materials **23**(10): 2626-2629.

Gass, M. H., U. Bangert, et al. (2008). "Free-standing graphene at atomic resolution." Nat Nano **3**(11): 676-681.

Geim, A. K. and K. S. Novoselov (2007). "The rise of graphene." Nature Mater. **6**: 183-191.

Gerion, D., W. J. Parak, et al. (2002). "Sorting fluorescent nanocrystals with DNA." J Am Chem Soc **124**(24): 7070-7074.

Ghezelbash, A. and B. A. Korgel (2005). "Nickel Sulfide and Copper Sulfide Nanocrystal Synthesis and Polymorphism." Langmuir **21**(21): 9451-9456.

Girit, Ç. Ö., J. C. Meyer, et al. (2009). "Graphene at the Edge: Stability and Dynamics." Science **323**(5922): 1705-1708.

Greenham, N. C., X. Peng, et al. (1996). "Charge separation and transport in conjugated-polymer/semiconductor-nanocrystal composites studied by photoluminescence quenching and photoconductivity." Phys Rev B Condens Matter **54**(24): 17628-17637.

Guo, Q., G. M. Ford, et al. (2009). "Sulfide Nanocrystal Inks for Dense Cu(In1−xGax)(S1−ySey)2 Absorber Films and Their Photovoltaic Performance." Nano Letters **9**(8): 3060-3065.

Guo, Q., G. M. Ford, et al. (2010). "Fabrication of 7.2% Efficient CZTSSe Solar Cells Using CZTS Nanocrystals." Journal of the American Chemical Society **132**(49): 17384-17386.

Guo, Q., H. W. Hillhouse, et al. (2009). "Synthesis of Cu2ZnSnS4 Nanocrystal Ink and Its Use for Solar Cells." Journal of the American Chemical Society **131**(33): 11672-11673.

Guo, Q., S. J. Kim, et al. (2008). "Development of CuInSe2 Nanocrystal and Nanoring Inks for Low-Cost Solar Cells." Nano Letters **8**(9): 2982-2987.

Gur, I., N. A. Fromer, et al. (2006). "Controlled assembly of hybrid bulk-heterojunction solar cells by sequential deposition." J Phys Chem B **110**(50): 25543-25546.

Gur, I., N. A. Fromer, et al. (2005). "Air-stable all-inorganic nanocrystal solar cells processed from solution." Science **310**(5747): 462-465.

Heitsch, A. T., D. D. Fanfair, et al. (2008). "Solution−Liquid−Solid (SLS) Growth of Silicon Nanowires." Journal of the American Chemical Society **130**(16): 5436-5437.

Henderson, E. J., C. M. Hessel, et al. (2008). "Synthesis and photoluminescent properties of size-controlled germanium nanocrystals from phenyl trichlorogermane-derived polymers." J Am Chem Soc **130**(11): 3624-3632.

Hessel, C. M., E. J. Henderson, et al. (2006). "Hydrogen Silsesquioxane: A Molecular Precursor for Nanocrystalline Si−SiO2 Composites and Freestanding Hydride-Surface-Terminated Silicon Nanoparticles." Chemistry of Materials **18**(26): 6139-6146.

Hessel, C. M., M. R. Rasch, et al. (2010). "Alkyl passivation and amphiphilic polymer coating of silicon nanocrystals for diagnostic imaging." Small **6**(18): 2026-2034.

Hessel, C. M., P. P. V, et al. (2011). "Copper selenide nanocrystals for photothermal therapy." Nano Lett **11**(6): 2560-2566.

Holmberg, V. C., M. G. Panthani, et al. (2009). "Phase transitions, melting dynamics, and solid-state diffusion in a nano test tube." Science **326**(5951): 405-407.

Holmes, J. D., K. P. Johnston, et al. (2000). "Control of Thickness and Orientation of Solution-Grown Silicon Nanowires." Science **287**(5457): 1471-1473.

Hummers, W. S. and R. E. Offeman (1958). "Preparation of Graphitic Oxide." Journal of the American Chemical Society **80**(6): 1339-1339.

Hussain, N. and A. T. Florence (1998). "Utilizing Bacterial Mechanisms of Epithelial Cell Entry: Invasin-induced Oral Uptake of Latex Nanoparticles." Pharmaceutical Research **15**(1): 153-156.

Huynh, W. U., J. J. Dittmer, et al. (2002). "Hybrid nanorod-polymer solar cells." Science **295**(5564): 2425-2427.

Iijima, S. (1987). "Fine Particles of Silicon. II. Decahedral Multiply-Twinned Particles." Japanese Journal of Applied Physics **26**(3): 365-372.

Jackson, P., D. Hariskos, et al. (2011). "New world record efficiency for Cu(In,Ga)Se2 thin-film solar cells beyond 20%." Progress in Photovoltaics: Research and Applications **19**(7): 894-897.

Jain, P. K., L. Amirav, et al. (2010). "Nanoheterostructure cation exchange: anionic framework conservation." J Am Chem Soc **132**(29): 9997-9999.

Jurbergs, D., E. Rogojina, et al. (2006). "Silicon nanocrystals with ensemble quantum yields exceeding 60%." Appl. Phys. Lett. **88**(23): 233116.

Kamat, P. V. (2009). "Graphene-Based Nanoarchitectures. Anchoring Semiconductor and Metal Nanoparticles on a Two-Dimensional Carbon Support." The Journal of Physical Chemistry Letters **1**(2): 520-527.

Kamat, P. V. (2011). "Graphene-Based Nanoassemblies for Energy Conversion." The Journal of Physical Chemistry Letters **2**(3): 242-251.

Kim, K., Z. Lee, et al. (2011). "Grain Boundary Mapping in Polycrystalline Graphene." ACS Nano **5**(3): 2142-2146.

Kim, S., B. Fisher, et al. (2003). "Type-II quantum dots: CdTe/CdSe(core/shell) and CdSe/ZnTe(core/shell) heterostructures." J Am Chem Soc **125**(38): 11466-11467.

Kim, S., Y. T. Lim, et al. (2004). "Near-infrared fluorescent type II quantum dots for sentinel lymph node mapping." Nat Biotechnol **22**(1): 93-97.

Kim, S. W., J. P. Zimmer, et al. (2005). "Engineering InAs(x)P(1-x)/InP/ZnSe III-V alloyed core/shell quantum dots for the near-infrared." J Am Chem Soc **127**(30): 10526-10532.

Klein, D. L., R. Roth, et al. (1997). "A single-electron transistor made from a cadmium selenide nanocrystal." Nature **389**(6652): 699-701.

Koleilat, G. I., L. Levina, et al. (2008). "Efficient, stable infrared photovoltaics based on solution-cast colloidal quantum dots." ACS Nano **2**(5): 833-840.

Korgel, B. A., S. Fullam, et al. (1998). "Assembly and Self-Organization of Silver Nanocrystal Superlattices: Ordered "Soft Spheres"." The Journal of Physical Chemistry B **102**(43): 8379-8388.

Kroto, H. W., J. R. Heath, et al. (1985). "C60: Buckminsterfullerene." Nature **318**(6042): 162-163.

Kuipers, E. W., C. Laszlo, et al. (1993). "Deposition of nanocrystals on flat supports by spin-coating." Catalysis Letters **17**(1): 71-79.

Kumar, A. P. and K. V. Reddy (1997). "Lateral self-diffusion of selenium in CuInSe2 thin films." Thin Solid Films **304**(1-2): 365-370.

Law, M., M. C. Beard, et al. (2008). "Determining the internal quantum efficiency of PbSe nanocrystal solar cells with the aid of an optical model." Nano Lett **8**(11): 3904-3910.

Law, M., J. M. Luther, et al. (2008). "Structural, optical, and electrical properties of PbSe nanocrystal solids treated thermally or with simple amines." J Am Chem Soc **130**(18): 5974-5985.

Lee, D. C., J. M. Pietryga, et al. (2009). "Colloidal synthesis of infrared-emitting germanium nanocrystals." J Am Chem Soc **131**(10): 3436-3437.

Lee, J.-S., M. V. Kovalenko, et al. (2011). "Band-like transport, high electron mobility and high photoconductivity in all-inorganic nanocrystal arrays." Nature Nanotechnology **6**(6): 348-352.

Lee, J.-S., E. V. Shevchenko, et al. (2008). "Au−PbS Core−Shell Nanocrystals: Plasmonic Absorption Enhancement and Electrical Doping via Intra-particle Charge Transfer." Journal of the American Chemical Society **130**(30): 9673-9675.

Lee, Z., K.-J. Jeon, et al. (2009). "Direct Imaging of Soft−Hard Interfaces Enabled by Graphene." Nano Letters **9**(9): 3365-3369.

Leong, J. M., P. E. Morrissey, et al. (1995). "An aspartate residue of the Yersinia pseudotuberculosis invasin protein that is critical for integrin binding." The EMBO Journal **14**(3): 422-431.

Li, L., T. J. Daou, et al. (2009). "Highly Luminescent CuInS2/ZnS Core/Shell Nanocrystals: Cadmium-Free Quantum Dots for In Vivo Imaging." Chemistry of Materials **21**(12): 2422-2429.

Li, X., W. Cai, et al. (2009). "Large-Area Synthesis of High-Quality and Uniform Graphene Films on Copper Foils." Science **324**(5932): 1312-1314.

Lightcap, I. V., T. H. Kosel, et al. (2010). "Anchoring Semiconductor and Metal Nanoparticles on a Two-Dimensional Catalyst Mat. Storing and Shuttling Electrons with Reduced Graphene Oxide." Nano Letters **10**(2): 577-583.

Lim, Y. T., S. Kim, et al. (2003). "Selection of quantum dot wavelengths for biomedical assays and imaging." Mol Imaging **2**(1): 50-64.

Liu, W., H. S. Choi, et al. (2007). "Compact cysteine-coated CdSe(ZnCdS) quantum dots for in vivo applications." J Am Chem Soc **129**(47): 14530-14531.

Luther, J. M., M. Law, et al. (2008). "Structural, optical, and electrical properties of self-assembled films of PbSe nanocrystals treated with 1,2-ethanedithiol." ACS Nano **2**(2): 271-280.

Luther, J. M., H. Zheng, et al. (2009). "Synthesis of PbS nanorods and other ionic nanocrystals of complex morphology by sequential cation exchange reactions." J Am Chem Soc **131**46): 16851-16857.

McBride, J. R., A. R. Lupini, et al. (2009). "Few-Layer Graphene as a Support Film for Transmission Electron Microscopy Imaging of Nanoparticles." ACS Applied Materials & Interfaces **1**(12): 2886-2892.

McCandless, B. E. and W. N. Shafarman (2003). Chemical surface Depostion of Ultra-thin Semiconductors. U. S. P. Office. USA. **US Patent 6,537,845**.

McDonald, S. A., G. Konstantatos, et al. (2005). "Solution-processed PbS quantum dot infrared photodetectors and photovoltaics." Nat Mater **4**(2): 138-142.

Medintz, I. L., H. T. Uyeda, et al. (2005). "Quantum dot bioconjugates for imaging, labelling and sensing." Nat Mater **4**(6): 435-446.

Mekis, I, et al. (2003). "One-Pot Synthesis of Highly Luminescent CdSe/CdS Core-Shell Nanocrystals via Organometallic and “Greener” Chemical Approaches." Journal of Physical Chemistry B **107**(30): 7454-7462.

Meyer, J. C., A. K. Geim, et al. (2007). "The structure of suspended graphene sheets." Nature **446**(7131): 60-63.

Meyer, J. C., C. O. Girit, et al. (2008). "Imaging and dynamics of light atoms and molecules on graphene." Nature **454**(7202): 319-322.

Meyer, J. C., C. Kisielowski, et al. (2008). "Direct Imaging of Lattice Atoms and Topological Defects in Graphene Membranes." Nano Letters **8**(11): 3582-3586.

Michalet, X., F. F. Pinaud, et al. (2005). "Quantum Dots for Live Cells, in Vivo Imaging, and Diagnostics." Science **307**(5709): 538-544.

Morales, A. M. and C. M. Lieber (1998). "A Laser Ablation Method for the Synthesis of Crystalline Semiconductor Nanowires." Science **279**(5348): 208-211.

Mott, N. F. (1987). Conduction in Non-Crystalline Materials, Oxford University Press, USA.

Mott, N. F. (1990). Metal-Insulator Transitions, CRC Press.

Murray, C. B., C. R. Kagan, et al. (2000). "SYNTHESIS AND CHARACTERIZATION OF MONODISPERSE NANOCRYSTALS AND CLOSE-PACKED NANOCRYSTAL ASSEMBLIES." Annual Review of Materials Science **30**(1): 545-610.

Murray, C. B., D. J. Norris, et al. (1993). "Synthesis and characterization of nearly monodisperse CdE (E = sulfur, selenium, tellurium) semiconductor nanocrystallites." Journal of the American Chemical Society **115**(19): 8706-8715.

Nelson, J. (2003). The Physics of Solar Cells, Imperial College Press.

Novoselov, K. S. (2005). "Two-dimensional gas of massless Dirac fermions in graphene." Nature **438**: 197-200.

Panthani, M. G., V. Akhavan, et al. (2008). "Synthesis of CulnS2, CulnSe2, and Cu(InxGa(1-x))Se2 (CIGS) nanocrystal "inks" for printable photovoltaics." J Am Chem Soc **130**(49): 16770-16777.

Park, S., J. An, et al. (2009). "Colloidal Suspensions of Highly Reduced Graphene Oxide in a Wide Variety of Organic Solvents." Nano Letters **9**(4): 1593-1597.

Pattantyus-Abraham, A. G., I. J. Kramer, et al. (2010). "Depleted-heterojunction colloidal quantum dot solar cells." ACS Nano **4**(6): 3374-3380.

Pietryga, J. M., R. D. Schaller, et al. (2004). "Pushing the band gap envelope: mid-infrared emitting colloidal PbSe quantum dots." J Am Chem Soc **126**(38): 11752-11753.

Puzzo, D. P., E. J. Henderson, et al. (2011). "Visible Colloidal Nanocrystal Silicon Light-Emitting Diode." Nano Letters **11**(4): 1585-1590.

Rizzo, A., C. Nobile, et al. (2009). "Polarized light emitting diode by long-range nanorod self-assembling on a water surface." ACS Nano **3**(6): 1506-1512.

Rogach, A. L., D. S. Koktysh, et al. (2000). "Layer-by-Layer Assembled Films of HgTe Nanocrystals with Strong Infrared Emission." Chemistry of Materials **12**(6): 1526-1528.

Sadtler, B., D. O. Demchenko, et al. (2009). "Selective facet reactivity during cation exchange in cadmium sulfide nanorods." J Am Chem Soc **131**(14): 5285-5293.

Saito, Y. (1979). "Crystal Structure and Habit of Silicon and Germanium Particles Grown in Argon Gas." Journal of Crystal Growth **47**: 61-72.

Schaller, R. D. and V. I. Klimov (2004). "High efficiency carrier multiplication in PbSe nanocrystals: implications for solar energy conversion." Phys Rev Lett **92**(18): 186601.

Schrier, J., D. O. Demchenko, et al. (2007). "Optical properties of ZnO/ZnS and ZnO/ZnTe heterostructures for photovoltaic applications." Nano Lett **7**(8): 2377-2382.

Shevchenko, E. V., D. V. Talapin, et al. (2006). Structural diversity in binary nanoparticle superlattices, Nature Publishing Group. **439:** 55-59.

Shevchenko, E. V., D. V. Talapin, et al. (2006). "Structural diversity in binary nanoparticle superlattices." Nature **439**(7072): 55-59.

Shevchenko, E. V., D. V. Talapin, et al. (2006). "Structural Characterization of Self-Assembled Multifunctional Binary Nanoparticle Superlattices." Journal of the American Chemical Society **128**(11): 3620-3637.

Shevchenko, E. V., D. V. Talapin, et al. (2005). "Polymorphism in AB₁₃ Nanoparticle Superlattices: An Example of Semiconductor-Metal Metamaterials." Journal of the American Chemical Society **127**(24): 8741-8747.

Shklovskii, B. I., B. I. Shklovskiĭ, et al. (1984). Electronic properties of doped semiconductors, Springer-Verlag.

Shockley, W. and H. J. Queisser (1961). "Detailed Balance Limit of Efficiency of p-n Junction Solar Cells." Journal of Applied Physics **32**(3): 510 - 519.

Smith, D. K., B. Goodfellow, et al. (2009). "Self-Assembled Simple Hexagonal AB2 Binary Nanocrystal Superlattices: SEM, GISAXS, and Defects." Journal of the American Chemical Society **131**(9): 3281-3290.

Soltesz, E. G., S. Kim, et al. (2006). "Sentinel lymph node mapping of the gastrointestinal tract by using invisible light." Ann Surg Oncol **13**(3): 386-396.

Staebler, D. and C. Wronski (1977). "Reversible conductivity changes in discharge?produced amorphous Si." Appl. Phys. Lett. **31**(4): 292.

Steckel, J. S., S. Coe-Sullivan, et al. (2003). "1.3 μm to 1.55 μm Tunable Electroluminescence from PbSe Quantum Dots Embedded within an Organic Device." Advanced Materials **15**(21): 1862-1866.

Steckel, J. S., J. P. Zimmer, et al. (2004). "Blue luminescence from (CdS)ZnS core-shell nanocrystals." Angew Chem Int Ed Engl **43**(16): 2154-2158.

Stroh, M., J. P. Zimmer, et al. (2005). "Quantum dots spectrally distinguish multiple species within the tumor milieu in vivo." Nat Med **11**(6): 678-682.

Talapin, V. D, et al. (2003). "Highly Emissive Colloidal CdSe/CdS Heterostructures of Mixed Dimensionality." Nano Letters **3**(12): 1677-1681.

Talapin, V. D, et al. (2004). "CdSe/CdS/ZnS and CdSe/ZnSe/ZnS Core-Shell-Shell Nanocrystals." Journal of Physical Chemistry B **108**(49): 18826-18831.

Talapin, D. V. and C. B. Murray (2005). "PbSe Nanocrystal Solids for n- and p-Channel Thin Film Field-Effect Transistors." Science **310**(5745): 86-89.

Talapin, D. V., E. V. Shevchenko, et al. (2004). "CdSe and CdSe/CdS Nanorod Solids." Journal of the American Chemical Society **126**(40): 12984-12988.

Talapin, D. V., E. V. Shevchenko, et al. (2007). "Dipole−Dipole Interactions in Nanoparticle Superlattices." Nano Letters **7**(5): 1213-1219.

Tang, J., K. W. Kemp, et al. (2011). "Colloidal-quantum-dot photovoltaics using atomic-ligand passivation." Nat Mater **10**(10): 765-771.

Tyrer, P. C., A. Ruth Foxwell, et al. (2007). "Receptor mediated targeting of M-cells." Vaccine **25**(16): 3204-3209.

Urban, J. J., D. V. Talapin, et al. (2007). "Synergism in binary nanocrystal superlattices leads to enhanced p-type conductivity in self-assembled PbTe/Ag2 Te thin films." Nat Mater **6**(2): 115-121.

Wang, Y. Q., R. Smirani, et al. (2004). "Nanotwinning in Silicon Nanocrystals Produced by Ion Implantation." Nano Letters **4**(10): 2041-2045.

Warner, J. H., M. H. Rümmeli, et al. (2009). "Examining Co-Based Nanocrystals on Graphene Using Low-Voltage Aberration-Corrected Transmission Electron Microscopy." ACS Nano **4**(1): 470-476.

Weissleder, R. (2001). "A clearer vision for in vivo imaging." Nat Biotech **19**(4): 316-317.

Westenfelder, B., J. C. Meyer, et al. (2011). "Graphene-based sample supports for in situ high-resolution TEM electrical investigations." Journal of Physics D: Applied Physics **44**(5): 055502.

Wood, V., M. J. Panzer, et al. (2009). "Inkjet-Printed Quantum Dot–Polymer Composites for Full-Color AC-Driven Displays." Advanced Materials **21**(21): 2151-2155.

Wu, Y., C. Wadia, et al. (2008). "Synthesis and photovoltaic application of copper(I) sulfide nanocrystals." Nano Lett **8**(8): 2551-2555.

Wu, Y. A., A. I. Kirkland, et al. (2011). "Utilizing boron nitride sheets as thin supports for high resolution imaging of nanocrystals." Nanotechnology **22**(19): 195603.

Xuanzhi, W. (2004). "High-efficiency polycrystalline CdTe thin-film solar cells." Solar Energy **77**(6): 803-814.

Yu, D., C. Wang, et al. (2003). "n-Type Conducting CdSe Nanocrystal Solids." Science **300**(5623): 1277-1280.

Yu, D., C. Wang, et al. (2004). "Variable Range Hopping Conduction in Semiconductor Nanocrystal Solids." Physical Review Letters **92**(21): 216802.

Yuk, J. M., K. Kim, et al. (2011). "Graphene Veils and Sandwiches." Nano Lett.

Zacharias, M., J. Blasing, et al. (1999). "Thermal Crystallization of Amorphous Si/SiO2 superlattices." Applied Physics Letters **74**(18): 2614-2616.

Zanella, M., G. Bertoni, et al. (2011). "Assembly of shape-controlled nanocrystals by depletion attraction." Chem Commun (Camb) **47**(1): 203-205.

Zhu, Y., S. Murali, et al. (2010). "Graphene and graphene oxide: synthesis, properties, and applications." Adv Mater **22**(35): 3906-3924.

Zylbersztejn, A. and N. F. Mott (1975). "Metal-insulator transition in vanadium dioxide." Physical Review B **11**(11): 4383.

Vita

Matthew George Panthani was born on May 18, 1984 in Boston, Massachusetts and lived in the Cleveland, Ohio area for most of his childhood. After graduating from high school in 2002, he attended Case Western Reserve University. From May to December 2004, he worked as a cooperative education engineer at Forest Laboratories in Commack, NY. In 2006, he graduated with a B.S. in Chemical Engineering and subsequently entered graduate school at the University of Texas at Austin in the Department of Chemical Engineering. He did his doctoral research under the guidance of Professor Brian A. Korgel studying colloidal nanomaterials for use in photovoltaic applications.

Permanent email: matthew.panthani [at] gmail <dot> com

This dissertation was typed by the author.